Investigation and modelling of post processing of AlSi10Mg manufactured by LPBF

Department of Mechanics, Mathematics and Management
MECHANICAL AND MANAGEMENT ENGINEERING
Ph.D. Program
SSD: ING-IND/16–ADVANCED MANUFACTURING PROCESSES

Final Dissertation

Investigation and modelling of post-processing of AlSi10Mg manufactured by LPBF

---

by
Alexandra Morvayova

Supervisors:

Prof. Giuseppe Casalino

Prof. Giuseppe P. Demelio

Coordinator of Ph.D. Program:
Prof. Giuseppe Pompeo Demelio

Course n°36, 01/11/202020-31/1/202

Department of Mechanics, Mathematics and Management
MECHANICAL AND MANAGEMENT ENGINEERING
Ph.D. Program
SSD: ING-IND/16–ADVANCED MANUFACTURING PROCESSES

Final Dissertation

Investigation and modelling of post-processing of AlSi10Mg manufactured by LPBF

by
Alexandra Morvayova

Referees:

Prof. ....

Prof. ....

Supervisors:

Prof. Giuseppe Casalino

Prof. Giuseppe P. Demelio

Coordinator of Ph.D Program:
Prof. Giuseppe Pompeo Demelio

Course n°36, 01/11/2020-31/01/2024

“One day I will find the right words, and they will be simple.”

Jack Kerouac

Acknowledgements

I wish to express my sincere gratitude to Prof. Casalino and Prof. Demelio for their guidance during this project as well as for their tutoring throughout all my PhD. journey. I am deeply grateful for all the inspiring discussions and experienced suggestions but also for providing me enough space to make my own mistakes and learn from them.

I would like to express special thanks to Prof. Contuzzi for his help and valuable suggestions in my research, especially in the context of numerical simulations. I am also very grateful to Prof. Fabbiano for her endless help with the metrological aspect of this thesis.

Last but not least, I wish to thank my family, my fake twin Karolína, and Giuseppe for their endless emotional support and for believing in myself even in moments when I was losing hope.

Abstract

The integration of additive manufacturing, specifically Laser Powder Bed Fusion (LPBF) with Aluminium alloys, represents promising opportunities for industries such as automotive and aerospace, where components with complex designs and optimal strength-to-weight ratios are crucial. However, the industrial reliability of LPBF technology is limited by the complex and not fully understood process-structure-property relationship in the scope of fabrication.

This thesis experimentally explores and demonstrates the interconnected nature of this relationship, exploring the potential for creating numerical models to tailor microstructures in post-process treatment using simple thermal sensors. The irregular response of the LPBF-manufactured component to the thermal load suggests the ongoing microstructural transformation within the specimen induced by the elevated temperature, which, in further context, demonstrates an alteration of the mechanical properties.

Moreover, the thesis meticulously studied the effects of the position of the specimens on the building platform when manufacturing more specimens simultaneously on the geometrical dimensions and tolerances of the manufactured cubes. The findings have great industrial significance, especially for the demanding fields requiring high accuracy of the manufactured components.

Additionally, this work addresses the persistent issue of defects in LPBF-manufactured Aluminium Alloy. A Finite Element Method (FEM) numerical model was proposed, predicting lack-of-fusion defects in AlSi10Mg components ats mesoscale, which was validated through experiments. Optimal LPBF processing conditions for near fully dense components were identified and will serve as a foundation for further modelling of post-processing treatments.

The extensive literature review revealed a lack of standardized guidelines for post-process treatment of LPBF-manufactured AlSi10Mg components. Due to the absence of heat treatments specifically tailored for LPBF-manufactured AlSi10Mg, the industrial practice usually applies heat treatments standardized for cast Aluminium alloys, which are, due to the significant microstructural differences between as-built and as-cast AlSi10Mg, no longer effective. As an innovation, this thesis introduces a novel thermo-mechanical post-process treatment. The here-presented pinless Friction Stir Spot Processing (FSSP) aims to provide microstructural homogenization, porosity reduction, and material softening. The identified optimal processing window yielded low distortions and a significantly higher effective depth

compared to traditional methods like shot peening, while maintaining distortion levels comparable to those originating from the manufacturing process.

To support the study of that complex thermomechanical process, a new numerical model simulating material flow during treatment was proposed. The numerical model, utilizing a Coupled Eulerian-Lagrangian approach, offers an accurate prediction of phenomena such as flash formation and void suppression. The successful validation of the proposed model suggests that the proposed numerical model can be considered an effective tool in the optimization of the FSSP processing of LPBF-manufactured components. The numerical model works well in synergy with the numerical model simulating the LPBF process that was also introduced in this thesis.

The experimental results of the FSSP post-processing method showed that localized microstructural transformation within the TMAZ resulted in mechanical properties that diverge significantly from those of the as-built material. This phenomenon of localized anisotropy, which can manifest differential mechanical behaviour, could be particularly advantageous in numerous industrial applications, such as automotive, aerospace, and healthcare. In the context of different materials, the effect of this post-process treatment might be advantageous for the production of medical implants, where it could effectively reduce the risk of stress shielding by creating areas with brittle and ductile mechanical properties.

The synergistic integration of LPBF, renowned for its exceptional design flexibility, with the capability of FSSP to tailor mechanical properties in a localized manner, presents a transformative potential in the post processing of LPBF aluminium alloys.

Moreover, the efficacy of the presented post-process treatment, its relative simplicity, long tool life and the low environmental impact of the treatment hold the potential to determine the FSSP as the ideal type of post-processing for LPBF-manufactured AlSi10Mg alloy.

Contents

1. Introduction to LPBF and its post-processing

In the last decade, additive manufacturing (AM) has emerged as a transformative technology capable of converting intricate design concepts into fully functional parts. This revolutionary method, encompassing a range of techniques like vat polymerisation, material extrusion, material jetting, sheet lamination, powder bed fusion, direct energy deposition, and binder jetting, has had a profound impact across diverse industries, including medicine, automotive, aerospace, and engineering [1, 2, 3, 4, 5].

AM offers a myriad of advantages, including material savings, enhanced parts reliability, superior precision, reduced tool costs, and unparalleled design freedom. At its core, AM operates on a common paradigm characterized by its layer-wise and cyclic nature [1, 5]. The manufacturing process involves a finite number of cycles, each comprising layer deposition followed by cooling and consolidation. Although various AM technologies differ in applicable materials, energy sources, and specific process-related nuances, they share this fundamental layer-wise and cyclic approach [2, 3, 4].

AM has evolved significantly from its initial focus on polymeric materials. Extensive research in this field has expanded the scope of applicable materials, now encompassing metals, ceramics, organic materials, pastes, and even cells [1, 2]. The growing environmental concerns and the demand for eco-friendly transportation solutions have intensified research efforts in the production of lightweight components for automotive and aerospace industries. It is generally acknowledged that a 10% reduction in the weight of vehicles results in an almost 6% of reduction in fuel consumption. Such fuel savings represent a huge advantage towards diminishing the carbon footprint. This emphasis towards lightweight structures and fully functional parts has led to remarkable advancements in additive manufacturing technologies, particularly in metal processing [5, 6, 7].

The methods of additive manufacturing, inherently capable of processing metallic materials, can now be categorized based on the form of material supply. Presently, these methods include powder-bed systems, powder-fed systems, and wire-fed systems. It is important to note that metal AM technologies can be classified using various criteria, such as the energy source employed [8, 9]. Notably, components produced using different metal AM

methods, but the same materials might exhibit variations in geometric precision, microstructure, and mechanical properties [10, 11].

Among the metal AM technologies, metal powder bed fusion-based processes (M-PBF) stand out, offering superior precision albeit with reduced productivity compared to other metal AM processes. M-PBF processes, further classified into laser powder bed fusion (LPBF) and electron beam melting (EBM), employ laser heat and electron beams, respectively, to selectively melt the deposited metal powder bed [12, 13]. Despite its lower productivity, LPBF has gained significant traction due to its remarkable manufacturing precision, higher efficiency, and cost-effectiveness [10, 14, 15].

In summary, additive manufacturing has evolved beyond its initial constraints, now incorporating a wide array of materials and advanced processing methods. The emphasis on environmentally friendly practices and the demand for lightweight components have driven significant progress in metal AM technologies, making LPBF a particularly promising and cost-effective choice for precision manufacturing [6, 7, 10, 13, 14].

1.1. LPBF of metals

The recent advancements in laser technologies, marked by the development of more economical, compact, and versatile laser devices, coupled with their successful integration from research laboratories into industrial applications, represent a pivotal precursor to the growing popularity of Laser Powder Bed Fusion (LPBF) technology [15, 16].

LPBF, a cutting-edge manufacturing technique, operates through a cyclic process involving the deposition of thin layers of powder, selective melting in predefined coordinates, rapid cooling and consolidation of the melts, followed by the deposition of new powder layers, as illustrated in Figure 1 [17, 18]. The entire manufacturing process is seamlessly orchestrated by computer support, wherein the Computer-Aided Design (CAD) model undergoes segmentation into individual layers. Subsequently, each layer's transverse section, in conjunction with pre-programmed build parameters like hatch spacing and scanning strategy, serves as the foundation for generating the G-code that dictates the trajectory of the scanning head [15, 16, 17].

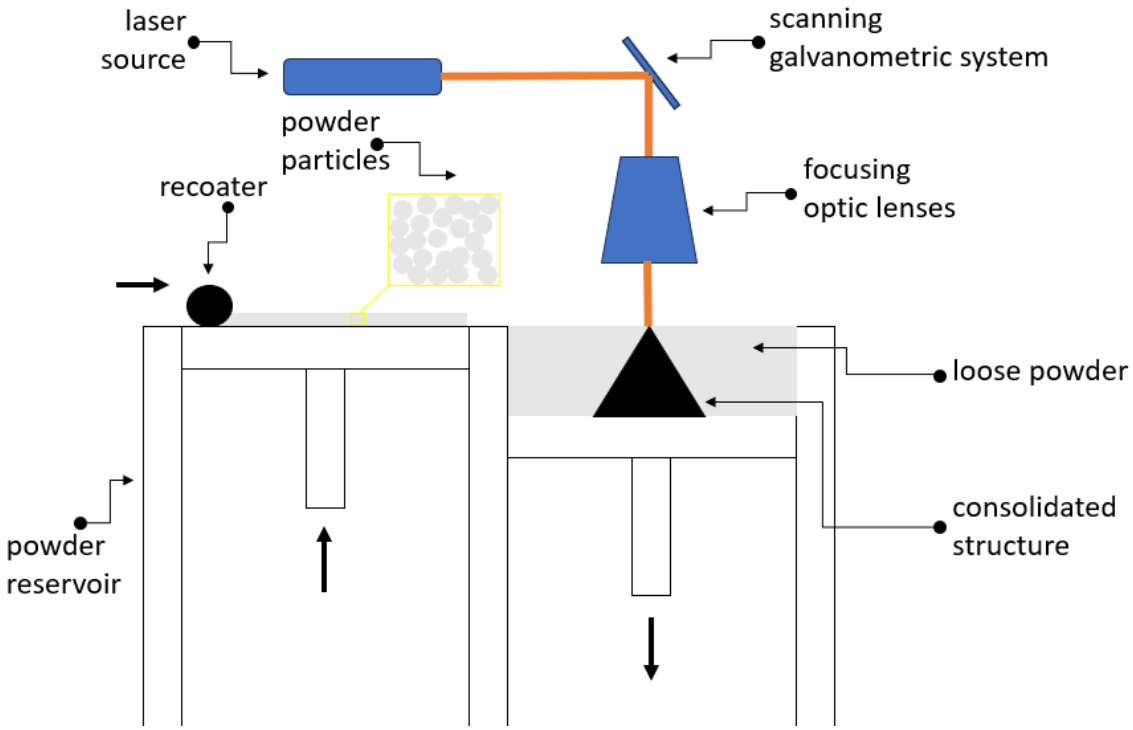

Figure 1 Schematic representation of LPBF manufacturing process

The metal Laser Powder Bed Fusion (LPBF) technique can be characterized as a multifaceted and highly dynamic process. The ultimate characteristics and microstructure of the produced components are shaped by various parameters of the manufacturing process, as it is represented in Table 1. The intricate nature inherent in this manufacturing process underscores its highly complex character, which, as of yet, remains partially unveiled in terms of the interrelationship between process, structure, and property [19, 20].

Table 1 Parameters influencing the final outcomes of LPBF manufacturing process

Process parameters				
Position related	**Powder related**	**Laser related**	**Scan related**	**Ambiance related**
• Position on the building plate	• Layer thickness	• Spot size diameter	• Scanning speed	• Platform preheating
• Orientation during the build	• Particles' size and shape distribution	• Laser power	• Hatch spacing	• Powder feeder preheating
	• Chemical composition	• Pulse characteristics	• Scan pattern	• Type of inert gas
	• Powder bed density			

The utilization of thin powder layers, typically around 30 microns in thickness, in conjunction with the relatively minuscule diameter of the laser beam, approximately of 100 microns, invariably yields heightened precision and considerable design flexibility in the production of components. The LPBF technique's unique capacity to craft intricate designs within a single process step, devoid of material waste, stands in stark contrast to conventional manufacturing methods that often necessitate a sequence of processes, leading to the excessive consumption of materials and energy. This distinction positions LPBF as a more environmentally sustainable manufacturing solution, fostering a greener and resource-efficient approach [20, 21, 22].

Furthermore, the potential for recycling the unmelted residual powder in LPBF enhances material efficiency. The paradigm shift from a multi-step manufacturing process for market-ready components to a singular production step within LPBF harbours the prospect of significantly reducing the design-to-manufacture timeline [22, 23].

It is imperative to underscore that the distinctive dynamics inherent in the LPBF process, characterized by elevated temperatures, the cyclic re-melting and re-heating of consolidated layers, and rapid heating rates, exert a profound influence on the microstructure and mechanical properties of the manufactured parts. Consequently, these properties may exhibit substantial deviations from those achieved through conventional manufacturing techniques, even when utilizing the same materials [15, 16, 18. 19].

While the metallic LPBF technology has achieved substantial commercialization, its current applicability is confined to a limited array of materials. Notably, titanium, nickel superalloys, refractory alloys, and tool and high-speed steels are among the extensively investigated and processed material grades within the scope of this manufacturing technology [24, 25].

In contemporary industrial settings, LPBF technology finds diverse applications, notably in the production of biomedical implants featuring customized geometries and specialized automotive and aerospace components characterized by reduced weight. The weight reduction of bespoke components can be realized through a variety of approaches, including optimized material selection—where aluminium alloys emerge as the lightweight yet high-strength

solution—topology optimization, and the integration of lattice structures, either individually or in combination. The persistent demand from industries for components that are simultaneously lightweight and high-strength serves as a driving force for the extensive global research in the LPBF manufacturing of aluminium alloys [26, 27, 28].

1.2. The specifics of LPBF manufacturing with Aluminium alloys

Several distinguishing characteristics of aluminium and its alloys render them advantageous for various industrial applications. These include a low density of 2700 kg/m³, high strength, commendable corrosion resistance, excellent weldability, and sufficient hardenability. While pure aluminium exhibits relatively low strength, the incorporation of various alloying elements is a common practice. Notably, silicon (Si), magnesium (Mg), and copper (Cu) serve to enhance strength, iron (Fe) and cobalt (Co) improve machinability, and nickel (Ni) enhances aluminium's performance under thermal loads [29, 30, 31].

Current research in LPBF processing of aluminium predominantly focuses on traditional aluminium alloys rather than exploring novel materials. The inherent properties of aluminium alloys, such as high thermal conductivity, high reflectivity, poor powder flowability, and low laser absorptivity, present challenges in LPBF processing. The combination of high thermal conductivity and reflectivity makes most aluminium alloys challenging to process due to the necessity of employing high laser powers to prevent incomplete melting and undesirable lack-of-fusions [32, 33].

Despite the need for high laser powers, the exceptional thermal conductivity of aluminium rapidly dissipates the energy from the laser beam. This phenomenon significantly contributes to the already rapid heating rates during the manufacturing process. The resulting extraordinarily high thermal gradients may lead to increased thermal stresses, further exacerbating the risk of solidification cracking. Notably, the high laser reflectivity of aluminium is commonly attributed to the abundance of free electrons [34, 35, 36].

Compounding these challenges is the poor flowability of aluminium powders, which hinders the proper deposition of successive layers and contributes to defects in consolidated parts. Both the low flowability of aluminium powders and the low viscosity of aluminium melts pose serious concerns during manufacturing, creating an environment conducive to porosity

formation. Addressing these intricacies in the LPBF processing of aluminium alloys is crucial for advancing the efficiency and quality of additive manufacturing in the realm of aluminium applications [32,33, 34, 35, 36].

Furthermore, the increased susceptibility of aluminium to oxidation significantly contributes to the formation of porosity. This issue can be mitigated to some extent through meticulous control of the processing environment within the build chamber and the application of inert gases. Thus, in order to avert the occurrence of defects in aluminium components produced by LPBF, thoughtful consideration should be given to either incorporating alloying elements or optimizing the process parameters [37].

For a comprehensive understanding of cast aluminium alloys, as endorsed by the Aluminium Association, their key characteristics are depicted in Figure 2.

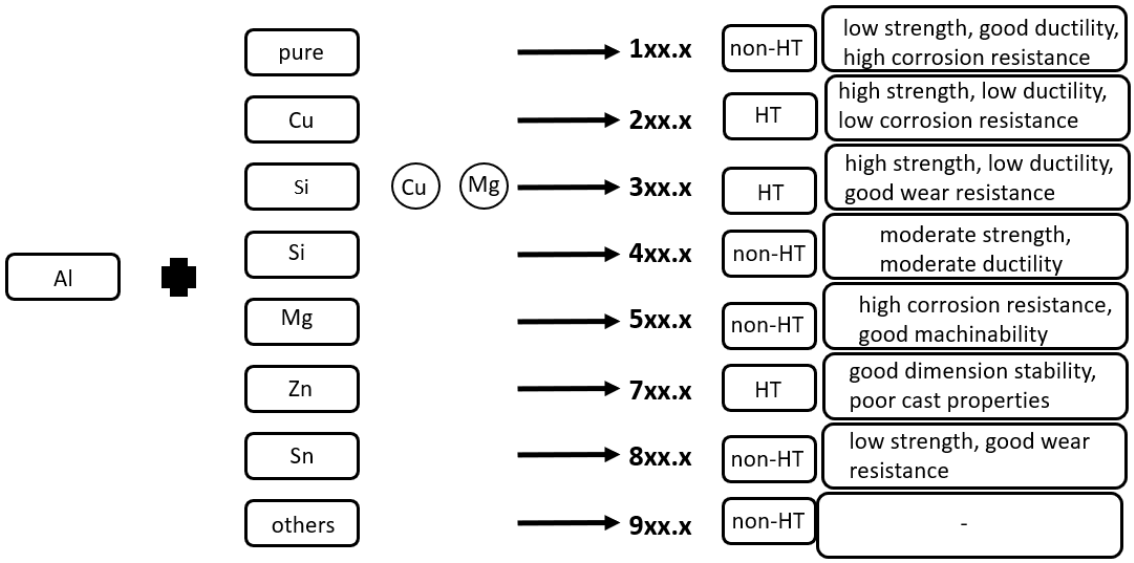

Figure 2 Cast aluminium alloys

In general, cast alloys, particularly AlSi10Mg and AlSi12, are notable for their high fraction of Al-Si eutectic, contributing to favourable castability and minimal shrinkage. These attributes make them suitable materials for LPBF processing. As previously discussed, the incorporation of Si enhances the mechanical properties of pure aluminium and improves melt fluidity. Similarly, the presence of Mg, as observed in the AlSi10Mg alloy, stands out as the most effective strengthening element. Mg promotes the formation of Mg2Si precipitates and exhibits high solubility [38, 39].

It is noteworthy that the compatibility between aluminium and Si/Mg as alloying elements is facilitated by their similar atomic structures, given their adjacency in the periodic table. However, their distinct differences arise from disparate crystal structures; aluminium adopts an FCC type, Si possesses a cubic crystal structure, and Mg exhibits a hexagonal structure [40, 41].

Both AlSi10Mg and AlSi12 alloys are characterized by average tensile strength and relatively low ductility. The LPBF manufacturing process, leading to a fine-grained and highly heterogeneous microstructure, can manipulate the overall properties of the manufactured components. These alloys find extensive use across diverse industrial sectors, underscoring their popularity and widespread application [37, 38, 39].

The characteristics of Aluminium powder particles, including size and shape, as the feedstock in the LPBF process, significantly influence process dynamics, resolution, and the overall properties of the manufactured parts [35, 36].

Despite the aforementioned advantages of LPBF processing with Aluminium alloys, particularly its capacity for intricate designs and the potential to revolutionize component manufacturing, its suitability and feasibility from a business perspective remain ambiguous. A comprehensive evaluation of product complexity, desired customization levels, and production volume is imperative. Notably, the current high cost of LPBF technology, coupled with its relatively low productivity and high energy demands, may disqualify it from consideration for manufacturing aluminium alloy components that could otherwise be conventionally produced [40, 41, 42].

1.2.1. Aluminium powders for LPBF manufacturing process

In accordance with the inherent characteristics of the LPBF manufacturing process, the foundational state of the Aluminium alloy utilized for constructing the specimens is in the form of powder. Predominantly, commercially available Aluminium powders specifically tailored for the LPBF process exhibit a particle size ranging from 25 to 70 μm [43, 44].

As of the present date, the vast majority of Aluminium powders is synthesized through the gas atomization process. This method entails the initial melting of Aluminium alloys, followed by subjecting the molten material to high-velocity gas jets. Subsequently, the molten material undergoes fragmentation into numerous droplets, which solidify during their trajectory. It is

pertinent to highlight that the gas atomization process yields metallic particles characterized by a diverse array of shapes and sizes. Consequently, these solidified particles undergo sieving or air classification based on their size range, tailored for diverse applications, including the specific size range conducive to LPBF processing [45, 46].

Given the nature of the gas atomization process, it follows that Aluminium powders for LPBF processing lack uniformity, comprising particles of varying sizes and shapes within the predetermined size range. Importantly, the morphology and particle size distribution of these powders hold considerable significance in the LPBF process, exerting a notable influence on the flowability and packing density of the deposited powder layers. Through empirical investigation, it has been established that spherical particles, in contrast to irregularly shaped counterparts, exhibit superior flowability and higher packing density. This, in turn, results in diminished porosity and fewer defects in the manufactured components [47].

Numerous researchers [48, 49] have investigated the prospect of augmenting the manufacturing resolution of LPBF by reducing the thickness of powder layers. Given that the diameter of the laser beam, a pivotal factor influencing resolution in fabricated components, is constrained within a high range that cannot be readily manipulated, the reduction of layer thickness emerges as a potential avenue for enhancing manufacturing resolution. This reduction, achievable through the utilization of finer powders, holds promise for addressing resolution challenges in LPBF [50].

Additionally, employing powders with smaller particle diameters not only facilitates lower layer thickness but also improves consolidation kinetics and augments the specific surface area relative to the volume of deposited layers. This, in turn, enhances laser absorptivity, further contributing to improved manufacturing resolution [48, 50].

Conversely, the utilization of finer aluminium powders in the LPBF process introduces concerns related to the heightened risk of inflammation and oxidation. It is imperative to underscore that the reduction in the diameter of powder particles significantly diminishes the minimum ignition energy required. Noteworthy is the fact that aluminium powders are classified in the Special Health Hazard Substance List, underscoring the necessity for cautious handling and manipulation [51].

In summary, while the reduction of powder layer thickness and the use of finer powders present potential avenues for elevating LPBF manufacturing resolution, the associated risks, particularly with finer aluminium powders, necessitate careful consideration and adherence to safety protocols [43, 47, 50].

1.2.2. Powder recycling

In the realm of scientific inquiry, a considerable portion of research attention is presently directed towards evaluating the impact of incorporating recycled powders on the quality of engineered components. It is noteworthy that a minor fraction of the deposited powder layers undergoes the process of melting and fusion, while the majority remains essentially intact. The reuse of the unfused powder emerges as a pivotal factor significantly enhancing the material efficiency of the LPBF manufacturing process [52, 53].

Conversely, the characteristics of the virgin powder may undergo substantial transformations during the manufacturing process. Multiple investigations [54, 55, 56] have validated the occurrence of progressed porosity, diminished mechanical performance, and an increased presence of defects in specimens produced from recycled powder, in contrast to those manufactured from virgin powder of the same material. This phenomenon can be attributed to the augmented dimensions of recycled powder particles, marked by the presence of numerous satellites originating from the splatters of molten metal, and an elevated oxygen content in recycled powders. Notably, literature [57] commonly reports nearly double the oxygen content in AlSi10Mg recycled powders, primarily ascribed to oxide formation. This poses a significant concern in the LPBF manufacturing process, as the oxides tend to envelop the liquid melt pools, thereby diminishing the wetting behaviour of adjacent unmelted powder particles [58].

The implications of these dynamics at the liquid-gas-solid interface frequently manifest in the formation of porosity. Consequently, the altered properties and heightened risk of defect development must be meticulously considered when employing recycled AlSi10Mg powder in the LPBF process for component manufacturing [52, 56, 58].

1.3. Physical phenomena and defect formation in LPBF manufacturing with Aluminium alloys

In the course of LPBF manufacturing, the material typically undergoes an intricate phase transformation, transitioning from a powdered form as its initial state, to a liquid state when

the powder is melted, further progressing to a gaseous state as the material evaporates. Ultimately, the material returns to a solid state upon cooling of the molten substance. The intricate interplay of kinetics and thermodynamics mechanisms during the LPBF process is accompanied by highly complex physical phenomena that manifest across diverse spatial and temporal scales. The rapid dynamics of LPBF contribute to the formation of various defects on all state interfaces [59, 60].

1.3.1. Powder bed and laser interactions

In the realm of LPBF, a pivotal occurrence is the intricate interplay between the laser and powder bed. The interaction initiates with the laser beam's absorption, a process significantly shaped by multiple reflections off the spherical-like surfaces of the powder particles and pores. As the laser beam converges, it permeates and scatters to a greater depth within the deposited layer [61, 62].

Upon irradiation of the powder bed, the incident photons' energy undergoes a transformation into thermal energy. Subsequently, this thermal load is applied to the powder bed within the track and is then dissipated across neighbouring powder particles. The intricate dynamics of heat transfer within the powder bed encompass radiation, convection, and heat conduction processes [61, 62, 63].

In the LPBF processing of metals, continuous fiber lasers are commonly employed. The prevalent wavelength for laser processing of metals is typically set at 1.1 μm, with the power density distribution of the laser beam adhering to a Gaussian-like pattern. Beyond the inherent powder characteristics influencing overall absorption and local energy distribution at the powder-laser boundary—such as surface roughness, presence of metal oxides, and temperature—the laser setup, incorporating parameters like laser power and wavelength, significantly shapes the interaction between the deposited powder bed and the laser beam (Figure 3). Additionally, the angle of incidence emerges as a noteworthy parameter influencing the dynamics of the laser-powder interactions [64, 65].

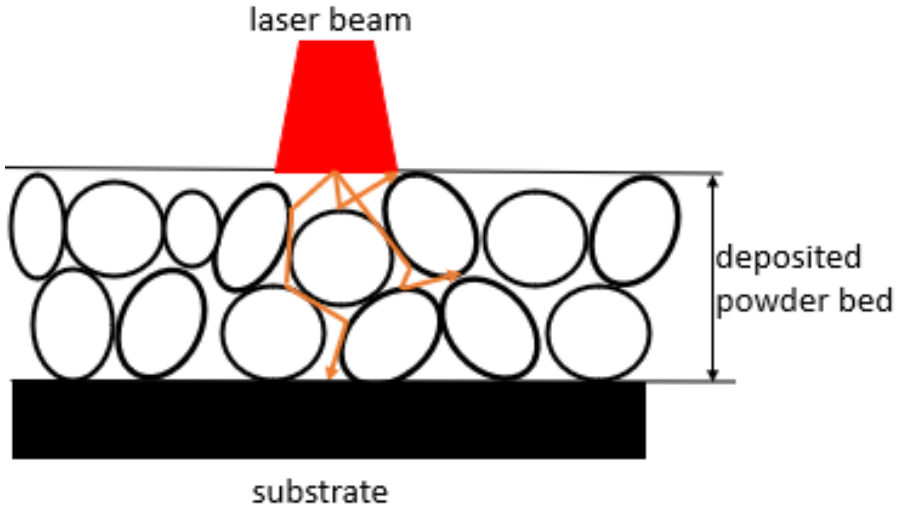

Figure 3 Laser-powder bed interaction

1.3.2. Liquid phase physical interactions

Upon exposure to the laser beam, the powder particles undergo a transformative process wherein the incident photons' energy is converted into thermal energy. This results in the rapid elevation of the powder particles' temperature, surpassing the melting point of the deposited metal. Subsequently, the irradiated powder particles undergo a phase transition, initially manifesting as liquid droplets that coalesce to form molten pools [66].

The intricate nature of the melt pools is dictated by elevated thermal gradients induced by the application of high laser power, coupled with the brisk dynamics arising from the utilization of high scanning speeds. Within the melt pools, various physical phenomena come into play, including gravity, surface tension, capillary forces, and buoyancy (Figure 4). The dynamics of the melt pools, inclusive of their geometry, kinetics, and thermodynamics, are orchestrated by both primary and secondary forces [67]. Primary forces involve the wetting behaviour of the powder particles, surface tension, and capillary forces, while secondary forces encompass gravity forces and surface tension. The interplay of these primary and secondary forces significantly influences the stability and geometry of the resulting melt tracks [68, 69].

Heat transfer within the melt pool is predominantly governed by Marangoni convection, a phenomenon driven by the formation of particle-accumulated structures and temperature-dependent surface tension. Broadly, Marangoni convection facilitates the transfer of molten metal with higher temperatures from the central region of the laser spot towards the peripheries [70].

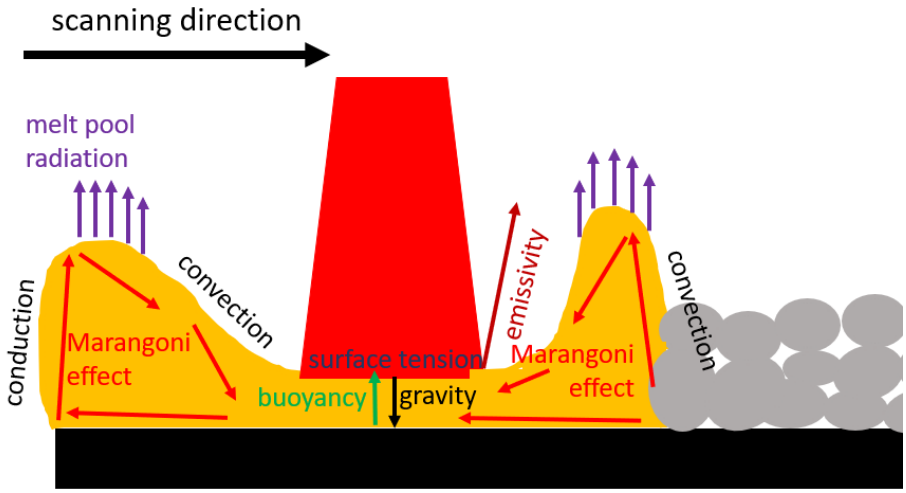

Figure 4 Melt pool dynamics

1.3.3. Metal evaporation and liquid-gaseous interface

Depending on the applied laser power and the ultimate temperature reached by the metal, the manufacturing process may give rise to varying degrees of metal evaporation. This phenomenon, with its potential for moderate to substantial metal loss, significantly impacts the stability of the LPBF process, emerging as a critical consideration in quality control [71].

Metal vaporization is intricately linked to the occurrence of several undesirable effects, including keyhole porosity, the balling effect, spattering, and powder denudation. Keyhole porosity arises from the recoil pressure exerted on the molten metal, leading to the formation of a cavity. Conversely, the release of vapor from the melt pool results in the loss of elements through burning and the potential alteration of chemical composition in comparison to the original powder composition. The subsequent solidification of metal vapours on scanning equipment poses a substantial risk to the errorless functioning of the manufacturing system [71, 72, 73].

Metal vapours exert a profound influence on the dynamics of shielding gas and the melt pool. Anomalies in the flow of molten metal manifest as numerous half-cylindrical or spherical micro melt tracks, characterized by insufficient contact with the substrate or previously deposited layers. This occurrence often arises when the liquid phase fails to adequately wet unmelted powder particles at the liquid-solid boundary or along grain boundaries, typically due

to the presence of impurities. Termed the balling effect, this phenomenon is primarily attributed to the Plateau–Rayleigh capillary instability of the melt pool [74, 75].

In contrast, larger melt pools exhibit increased viscosity, enhancing the flowability of molten metal and mitigating the risk of the balling effect. However, enhanced viscosity may introduce a different set of defects. The highly flowable molten metal, propelled by increased recoil pressure, facilitates the ejection of droplets of aluminium melts to higher regions. These ejected droplets undergo cooling, typically experiencing in-flight oxidation, before descending and adhering to solidifying melt tracks, thereby contributing to the formation of defects in the final product (Figure 5) [76, 77].

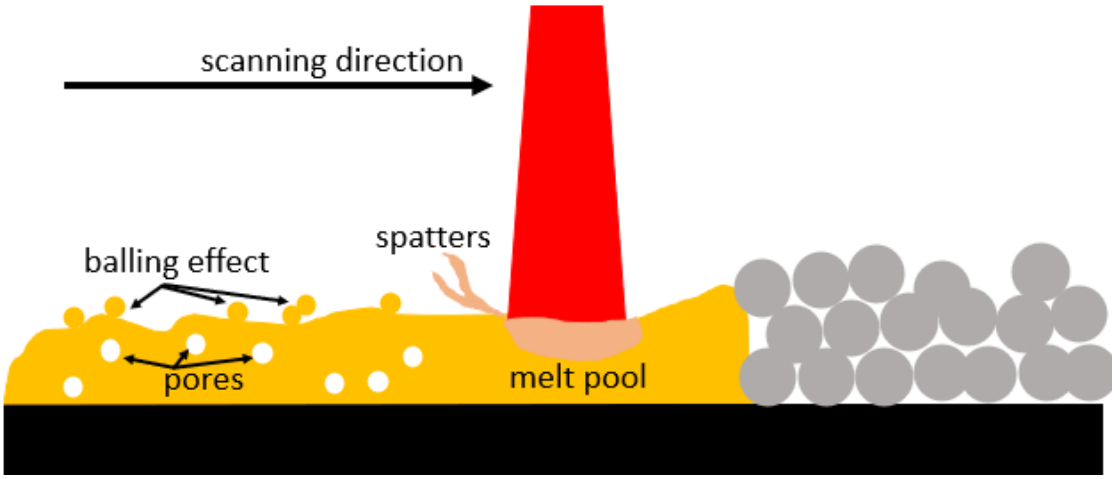

Figure 5 Defect formation in melt pools

In a similar vein, the evaporation of powder from the central regions of the melt pool is posited as the primary factor contributing to the denudation of powder in the proximity of the melt pool tracks. This phenomenon can be explained by the Bernoulli principle, wherein the augmentation of fluid flow velocity concurrently leads to a reduction in the pressure or potential energy of the fluid in motion. The substantial evaporation of metal and the resulting decrease in pressure within the vapor jet give rise to a formidable gas flow, sufficiently potent to strip away powder particles (Figure 6). The denudation of powder induced by flow-driven mechanisms notably impacts the dimensions of the melt pool [78, 79, 80].

Conversely, the interaction with the liquid and capillary forces during direct contact possesses the capability to integrate a limited number of adjacent powder particles into the melt pool. However, in comparison to the powder denudation driven by fluid flow, this mechanism exerts only a marginal influence on the ultimate characteristics of the resulting melt pool [78].

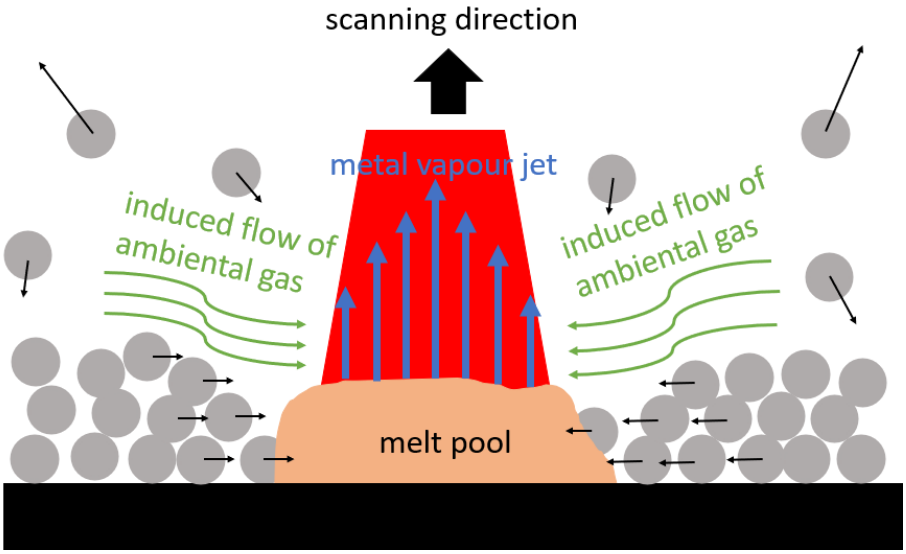

Figure 6 Powder denudation mechanism

It is crucial to recognize that the gas flow plays a dual role in the LPBF process. Not only does it facilitate the incorporation of denuded particles into the melt pool, but it also contributes to their vertical ejection, counter to the scanning direction. The ejected powder particles may either be redistributed back into the powder bed or adhere to the surface of semi-solid melt pools. This attachment of ejected powder particles to the solidifying melt track results in increased surface roughness—a characteristic frequently observed in LPBF-manufactured specimens. This phenomenon is intricately linked to the spatter formation described earlier [78, 81].

While the mechanisms governing powder denudation in LPBF manufacturing have garnered limited attention from the research community, recent studies indicate that careful control of the ambient gas pressure within the building chamber can manipulate powder denudation. Experimental findings underscore that lower pressure conditions yield sharper and more well-defined denudation zones. The significance of curbing excessive powder denudation lies in its dual impact: ensuring a more uniform powder distribution in subsequent layers and mitigating the risk of void linear structures in consolidated specimens featuring highly denudated zones. These insights highlight the importance of precise gas pressure regulation as a key parameter in optimizing the LPBF process for enhanced material quality and structural integrity [82, 83].

1.3.4. Solidification mechanisms

Notably, the phase transformation from liquid to solid critically determines the metallurgical microstructure of the final manufactured component. This solidification process is intricately regulated by cooling rates and spatial temperature gradients. The resultant grain morphology and texture are notably influenced by the solidification front, with distinct mechanisms at play during the LPBF manufacturing process [84, 85, 86].

Within this process, primary solidification unfolds in the fusion zone—directly impacted by the laser beam—where rapid cooling rates induce non-equilibrium conditions and undercooling at the solid-liquid interface. Simultaneously, secondary solidification occurs in heat-affected zones, defined by previously deposited layers, or in regions beyond the laser beam's influence [84, 86].

The solidification dynamics within the fused zone are characterized by swift cooling, leading to non-equilibrium conditions, and undercooling at the solid-liquid interface. Presently, it is widely acknowledged that the directional solidification microstructure in metals depends on the temperature gradient at the solid/liquid interface and the growth rate at the solidification front. The ratio of these parameters defines grain morphology, while their product governs grain size [87].

Within the solidification process, equiaxed α-Al grains nucleate in the constitutionally undercooled liquid near the liquid-solid boundary in the melt pool. Intriguingly, segregation occurs at the solidification front, resulting in initially formed solids having lower Si content than the remaining liquid alloy. As crystallization outpaces Si diffusion in the solid, the unsolidified alloy becomes enriched with Si. The region near melt pool boundaries termed the coarse zone, exhibits a coarser microstructure, primarily comprising primary α-Al grains with an equiaxed configuration. Consequently, the microstructure at melt pool boundaries is notably coarser than that within the melt pools [88, 89].

The solidification process initiates at the peripheries of the melt pools and progressively advances towards their centres. Within the melt pools, the microstructure is distinguished by the presence of the primary Aluminium phase and a nano-sized Al-Si network. The Aluminium, forming cellular-dendrites, intertwines with a fibrous Si network, exhibiting growth towards the central region of the laser tracks. Under specific conditions, grain growth

parallel to the thermal gradient may lead to the retention of interdendritic liquid at the interfaces. This, combined with the relatively high shrinkage of Aluminium, contributes to the formation of cracks [90, 91, 92].

Importantly, as one moves from the boundaries to the centres of the melt tracks, the microstructure undergoes a gradual refinement, constituting what is commonly referred to as the "fine zone." The observed variation in grain size is attributed to the non-constant solidification cooling rate, primarily dictated by the solidification velocity. Previous investigations have established that the solidification velocity during the LPBF process of Aluminum alloys is chiefly influenced by the morphology of the solid/liquid interface, resulting in a predominantly cellular structure constrained by the motion of the laser beam. In general, the solidification velocity is contingent on position, with higher velocities nearer to the top of the melt pool [93, 94, 95].

The ultrafine microstructure, induced by rapid cooling rates, imparts superior mechanical properties to LPBF-manufactured AlSi10Mg samples compared to their conventionally manufactured counterparts. The scheme of microstructure evolution within the melt pools is depicted in Figure 7 [96].

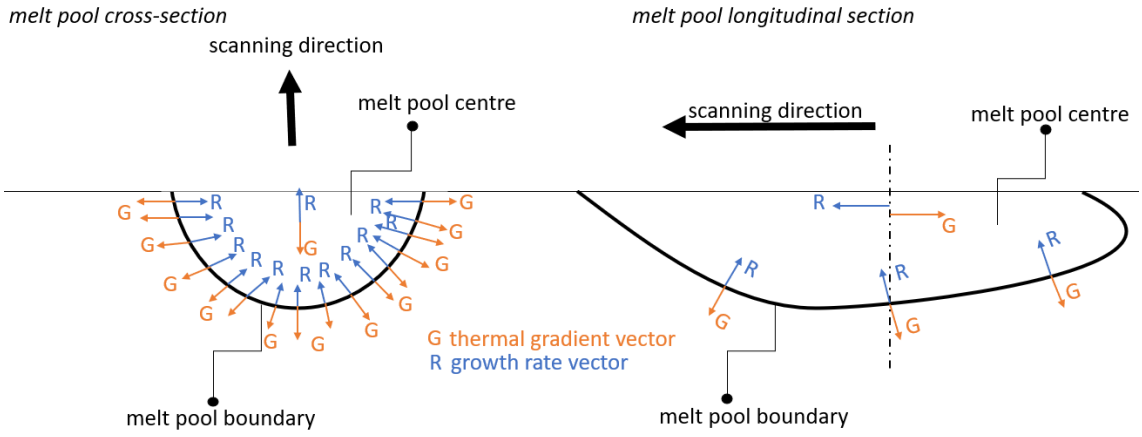

Figure 7 Microstructure evolution in LPBF process

In contrast to the rapid heating and cooling rates experienced within fusion zones, the material in heat-affected zones undergoes repeated heating and cooling cycles characterized by prolonged durations and considerably lower cooling rates. The maximal temperature within heat-affected zones decreases incrementally with each heating cycle and seldom surpasses the melting temperature. Consequently, the material within these zones predominantly undergoes

solid phase transformations. These unique conditions contribute to the partial disruption of the fibrous Si network, while the sluggish cooling rates foster grain coarsening [86, 92].

On a global spatial scale, the combination of high cooling rates and distinct thermal gradients within the cooling structure significantly induces the formation of residual stresses. In the context of LPBF manufacturing, the initiation of residual stresses occurs at the micro level for each deposited layer, culminating in the development of final macroscopic residual stresses. It is imperative to note that residual stresses are undesirable, as they compromise the mechanical properties of manufactured components, exacerbate distortions, and serve as precursors to the emergence of various defects, including cracks and delaminations [97, 98, 99].

Within the built direction, the typical residual stress distribution manifests as tensile stresses in the lower sections of the manufactured specimens, succeeded by compressive stresses in the middle regions and additional tensile stresses in the upper regions. These variations can be attributed to the robust bonding of the lower layers to the building platform and the exposure of the material to additional heating cycles, effectively serving as an in-situ thermal treatment [100].

1.4. Process-structure-property relationship regarding LPBF manufacturing of Aluminium alloys

Due to the intricacies inherent in the LPBF manufacturing process, predicting the overall properties of aluminium components produced through this method proves to be a relatively challenging. The complexity arises from the multitude of processing parameters at play, each exerting influence on the unique manufacturing conditions characteristic of LPBF. These processing parameters act as crucial boundary conditions, delineating the framework within which a myriad of physical phenomena unfold during the manufacturing process. Illustrated in the Figure 8 is a schematic representation of the intricate interplay between process parameters, resulting material structure, and the conclusive properties—a complex threshold that defines the LPBF framework [101, 102].

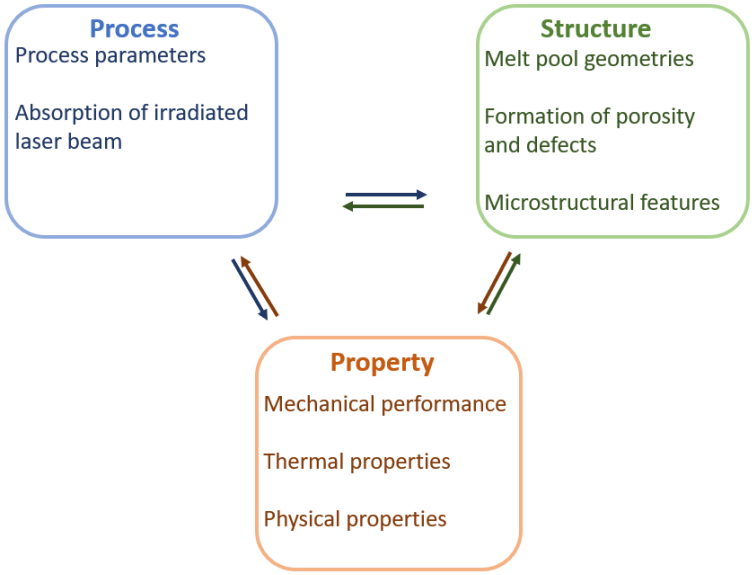

Figure 8 Scheme of process-structure-property interrelationship in LPBF

The structural characteristics of manufactured components are intricately tied to the specific manufacturing conditions imposed upon them. For instance, inadequate energy input from the laser beam can lead to incomplete melting and a lack of fusion in the material. Simultaneously, the energy input of the laser beam plays a pivotal role in shaping the thermal history of fused components. This, in turn, sets the stage for unique solidification conditions, yielding a microstructure characterized by heterogeneity, ultrafine features, and often, metastability [103].

Numerous analytical equations have been proposed to delineate the correlation between grain size and various mechanical properties in metals produced through manufacturing processes. Despite these efforts, comprehending the entirety of the process-structure-property relationship in LPBF remains a formidable challenge. The LPBF process is inherently complex, involving a myriad of physical phenomena and influential factors. Given this complexity, a substantial portion of the threshold connecting process parameters, material structure, and resulting properties remains inadequately understood [104].

In the realm of LPBF, despite extensive research endeavours, achieving a high level of controllability and reliability in the process remains unachieved. This inherent challenge stands as a significant impediment to the widespread industrial adoption of LPBF technology [105].

1.4.1. Volumetric energy density as a control mechanism of LPBF process

Volumetric energy density (VED) represents one of the most commonly used metrics to control the LPBF manufacturing process (1).

$$VED = \frac{P}{vht} \quad (1)$$

Where P denotes the laser power (W), v stands for the scanning speed (mm/s), h is the hatch spacing (mm) and t is the layer thickness (mm) [106, 107].

The provided formula reveals that various combinations of process parameters can yield the same VED. Although hatch spacing and layer thickness are typically fixed, the laser power and scanning speed exhibit an inverse proportionality that is widely employed to manipulate the LPBF process [108].

It is widely recognized that maintaining a low VED can lead to insufficient melting, resulting in larger and prolonged lack-of-fusion porosity. Conversely, an excessively high VED induces excessive evaporation of the molten metal. Given the LPBF's rapid cooling rates, molten metal swiftly solidifies, entrapping gas bubbles beneath the solidified material. This dynamic process manifests as a spherical porosity type with smaller diameters in the manufactured components' structure [108, 109].

It is crucial to note that the presented formula does not account for powder material properties and laser beam diameter. The neglecting of these parameters is particularly significant for Aluminium alloys, characterized by low laser absorptivity. In the case of Aluminium powder beds irradiated by a laser beam, the material does not absorb the total delivered effective energy. Consequently, higher VED values, especially achieved through increased laser power, are commonly employed in LPBF processing of Aluminium alloys. Therefore, the formula has been modified to incorporate the material aspects of powder in the LPBF process (2) [108, 109, 110, 111].

$$MVED = \frac{\beta}{h\sqrt{(4a\emptyset)}} \frac{P}{\sqrt{v}} \quad (2)$$

Where β stands for thermal diffusivity of the material, a is the laser absorptivity and Ø is the diameter of the laser beam. It should be however stated that even if formula (2) considers more

aspects of the manufacturing process, there are still numerous parameters that are neglected, such as scanning strategy, orientation of the manufacturing pieces and their position on the building platform. Various researchers have determined that volumetric energy density, as a thermodynamic quantity, does not possess the capability to sufficiently capture the physical phenomena taking place during the process [110, 111].

1.4.2. Effect of processing parameters on the melt pool dimensions

It was previously determined that the melt pool dimensions represent a more efficient feature in LPBF process control than VED or MVED since it considers more physical phenomena, including Marangoni convection, balling effect, etc. The melt pool geometry highly depends on the processing conditions and properties of the adopted materials (3).

$$\left(\frac{L}{w}\right)^2 = \frac{aePv}{32\pi k\beta (T-T_0)} \quad (3)$$

Where $\frac{L}{w}$ is the aspect ratio of the melt pool, e is the Euler's number, T is the melting temperature and T_0 is the temperature of the surrounding environment. Subsequently, the aspect ratio of the melt pool expands with increasing power and velocity. It was discovered that the melt pool clumps when its aspect ratio exceeds the critical value of the surface tension [112, 113].

This finding implies the potential coherence of the melt pool, shedding light on critical factors like the balling effect, pore formation, and delaminations. Consequently, identifiable melt pool instabilities may manifest as defects, leading to diminished mechanical properties in the fabricated components. Consequently, there exists a pressing need to scrutinize the processing parameters that impact melt pool formation and discern their optimal processing window. The careful management and forecasting of melt pool characteristics emerge as pivotal aspects in enhancing the reliability of the Laser Powder Bed Fusion (LPBF) manufacturing method [112, 113, 114, 115].

1.4.3. Tailoring of the microstructure in LPBF manufactured Aluminium parts

In accordance with the findings outlined in section 1.3.4, the microstructure of the fabricated components is intricately governed by both the temperature gradient and the growth

rate. The interplay between these two key parameters and their consequential impact on the microstructure is visually represented in Figure 9[84, 87, 88].

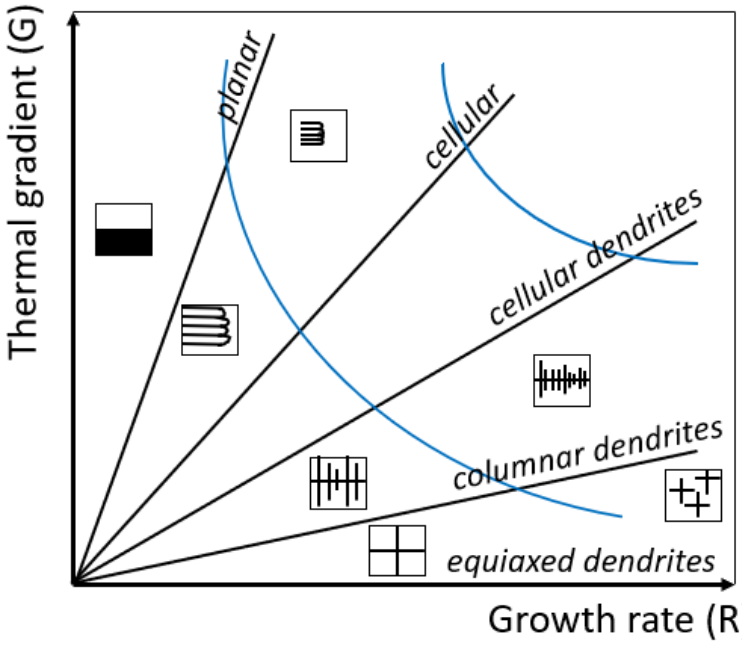

Figure 9 Interplay between G and R parameters and their impact on microstructure evolution

The interaction between the material and the laser beam, coupled with subsequent directional heat transfer, gives rise to thermal gradients within the heated structures. While it is widely acknowledged that high laser power primarily dictates the magnitude of these thermal gradients, the corresponding cooling and solidification rates are predominantly influenced by high scanning speeds. Nonetheless, current literature indicates that the thermal gradients in the LPBF process are intricately shaped by a multitude of parameters and processing conditions inherent to part manufacturing. These include laser characteristics, the temperature and material attributes of the building platform, and the positioning of the component in relation to the inlet or outlet of the inert gas, among other factors [116, 117].

Crucially, the spatial arrangement and configuration of components on the building platform wield a substantial impact on thermal gradients, particularly in scenarios involving the concurrent fabrication of multiple specimens. The accumulation of heat by neighbouring specimens can lead to pronounced thermal effects. Recognizing these nuances is essential for optimizing the LPBF process and ensuring consistent part quality [118].

Furthermore, it is widely established that the microstructural characteristics of specimens exert a profound influence on the mechanical properties of the manufactured parts. Materials

exhibiting a fine-grained microstructure generally manifest superior mechanical properties compared to their coarse-grained counterparts. This phenomenon is commonly attributed to the higher density of grain boundaries in fine-grained structures, which impedes crack propagation. Consequently, a finer microstructure is associated with enhanced structural integrity and improved mechanical performance in the final product [119, 120].

Several authors have introduced an intriguing approach to tailor microstructures by inducing precipitates. Notably, the presence of these precipitates significantly influences the mechanical properties of the as-built components. Achieving the desired volume of precipitates can be realized through the application of powders with optimized chemical compositions or by employing optimized laser processing parameters. In the case of AlSi10Mg alloys processed by LPBF, it is observed that the average concentration of Si in the α-Al phase surpasses the equilibrium state, attributed to the rapid cooling rates inherent in LPBF. The manipulation of laser processing parameters, therefore, becomes a pivotal factor influencing variations in cooling rates, subsequently impacting the volume, size, and chemical nature of the precipitates [121, 122].

Several researchers have introduced the unique capability of components with process-induced lack-of-fusion defects to function as designed lattices. This becomes especially compelling in scenarios where the manufacturing system's defined resolution poses challenges in creating small dimensions of lattices. A consensus among various researchers suggests that these process-induced defects could potentially serve as desired features, provided their position, size, volume, and range can be thoroughly controlled [123, 124].

The collective findings of numerous research teams underscore the importance of developing theoretical frameworks that presents the interrelations between process and condition parameters and the resulting microstructure. This development represents a crucial stride toward achieving precise control over microstructural features [117, 118, 120, 124].

1.4.4. Influence of the process parameters on the residual stresses and distortions in LPBF manufactured Aluminium parts

High residual stresses are frequently observed in Aluminium parts manufactured through LPBF. Due to their pronounced spatial variability, conventional analytical equations universally establishing the relationship between processing parameters and resultant residual

stresses lack applicability. This spatial variability also complicates the experimental assessment and subsequent evaluation of results. Consequently, researchers and industrial practitioners often resort to indirect determination of residual stresses through correlations with distortions, as distortions are predominantly attributed to residual stresses [97, 99, 125].

In both research and industrial applications, the significance of residual stresses is underscored by their impact on distortions. Controlling distortion is recognized as a crucial parameter in LPBF manufacturing, particularly as excessive distortion can render the manufactured specimens unsuitable for applications demanding high dimensional accuracy [98, 99].

Despite the multiparametric and intricate nature of residual stress formation, several studies have explored the interrelationships between imposed processing parameters and the resultant values of residual stresses. Notably, it has been observed that residual stresses exhibit simultaneous increases with escalating laser power and scanning speed. This phenomenon is generally linked to the heightened thermal gradients induced by high laser power and the rapid cooling rates associated with elevated scanning speeds [125].

Conversely, certain studies propose that excessive scanning speed may result in increased porosity within the fused specimen, potentially leading to the relaxation of formed residual stresses. While the literature extensively reports on the impact of laser power and scanning speed, the effects of layer thickness and scanning strategy on residual stresses have received comparatively less attention. Further exploration of these aspects is warranted to comprehensively understand and optimize the LPBF process for enhanced control over residual stresses and distortion in manufactured components [126, 127, 128, 129].

It has been however investigated that higher layer thickness partially works as an insulating medium, resulting in decreased heat transfer velocity to the bottom of the deposited layer, which is then demonstrated as the area with low residual stresses [130].

The current literature reports contradictory effects of the hatch spacing on the residual stresses in fused specimens. While some authors report that low hatch spacing increases the residual stresses in manufactured components due to increased thermal gradients, different studies have shown that lower hatch spacing increases the dimensions of heat affected zones,

where material reheating takes place. Such reheating has effects similar to in-situ heat treatment, with residual stress reduction as the main outcome [131, 132, 133, 134].

Various researchers have determined the scanning strategy as an important parameter in residual stress control. It was reported that areas with highest residual stresses are located along the scanning direction. In order to limit the accumulation of the residual stresses in manufactured parts, leading to excessive distortions, the alteration of the scanning direction between the successive layers is commonly applied [126, 129, 132, 133].

Depending on the geometry of the building parts, the island scanning strategy is usually recommended for the residual stress reduction. The lower length of the scan vectors, typical for the island scanning strategy reduces the thermal gradients between the neighbouring melt tracks and therefore reduces the residual stress cumulation [97, 99, 124, 130].

Despite the observed interrelations between the processing parameters and the residual stresses, the control of the residual stress cumulation, and consecutive distortion formation in LPBF-manufactured AlSi10Mg components still remains a challenge. Several parameters and aspects of the LPBF manufacturing process influencing the formation of residual stresses is not well investigated and reported. Better understanding of these mechanisms would lead to increased reliability of this manufacturing method, opening up new opportunities for industrial employments, including critical applications such as aerospace and medicine [97, 99, 126, 129].

Ideally, a thorough knowledge of process-structure-property threshold would enable the tailoring of the microstructure and consecutive properties of the LPBF manufactured components from Aluminium alloys.

1.5. Post-process treatment of LPBF manufactured Aluminium alloys

Despite the well-documented research attempts to improve the quality, and at the same time to minimize the defects in LPBF manufactured components from the Aluminium alloys, various undesired features, such as high surface roughness, porosity, excessive residual stresses, etc., can be commonly observed. With the objective to increase the quality of the manufactured parts, or to enhance their mechanical properties, various methods of post-process treatment are applied [135, 136].

1.5.1. Surface treatment

While there have been numerous attempts to increase the surface quality of the AlSi10Mg components manufactured by LPBF by optimizing the process parameters, the surface quality and integrity must be more often improved by various types of post-process treatment [137].

The methods of post-process treatment, commonly applied to LPBF-manufactured AlSi10Mg components to increase the surface quality include laser, mechanical, and chemical surface post-treatments, such as laser polishing, grinding, blasting and shot peening. Grinding and mechanical polishing are considered the most efficient methods of improving the quality and integrity of the surface characteristics in specimens manufactured by LPBF [137, 138].

It has been reported that the application of laser-based surface treatment methods (laser polishing, laser shock peening) results not only in a substantial decrease of the porosity but might also decrease the porosity in sub-surface areas. Interestingly, the laser re-melting (a method consisting of the repeated scanning of every solidified layer without previous powder deposition) has exhibited the ability to decrease the surface roughness by 50%, and in the same time decrease the porosity by 40%, when compared to the specimen built with same process parameters without laser re-melting. It should be however noted that the laser re-melting negatively affects the mechanical properties of the built parts as it substantially decreases the strength of the treated components [139, 140].

In contrast, the sandblasting and vibratory finishing reportedly increased the fatigue strength of the LPBF-manufactured AlSi10Mg components, compared to the as-built state. It was determined that sandblasting is less productive in increasing fatigue strength, on the other hand, its ability to decrease the surface roughness is much more efficient, compared to vibratory finishing [141, 142].

Similarly, the effects of chemical post-process surface treatment consist of both decreasing the surface roughness and increasing the fatigue strength. Both effects are however much less prominent, compared to the mechanical methods of surface treatment [143].

1.5.2. Shot peening

Shot peening can be considered one of the most common and simple cold working techniques and its effect on the Aluminium alloys manufactured by LPBF technique has been

well documented. Although the shot peening is not thoroughly efficient in decreasing the surface roughness of the manufactured pieces, the effects of this post-process treatment also consist of enhancing the compressive residual stresses and thus decreasing the tensile stresses, reducing the porosity, and increasing the high cycle fatigue behaviour of aluminium component manufactured by LPBF [144, 145, 146].

During shot peening, the highly accelerated beads, directed towards the treated surfaces cause plastic deformation localized on and under the surface of the treated components (Figure 10). The strain hardening phenomena leads to enhancement of the residual compressive stresses and high dislocations density in these regions. It has been reported that application of shot peening has the potential to improve the fatigue and tensile strength and enhance the hardness of the treated surfaces. While the effects of shot peening are considerably positive, the effective depth is rather small [144, 146].

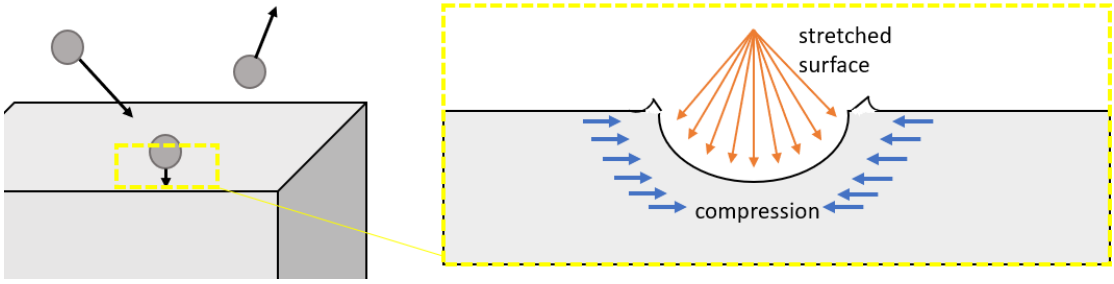

Figure 10 Schematic representation of the effects of shot peening

1.5.3. Hot isostatic pressing

The post-process treatment, commonly applied to LPBF manufactured components to decrease the process-induced porosity, with a considerably larger effective depth, compared to shot peening, is hot isostatic pressing (HIP). The working mechanism of this post-process treatment method applies heating of the specimen to a high temperature (depending on the material characteristics) and subjecting the specimen to a high pressure, usually just under the yield point. Both processes, heating and pressing, are applied simultaneously in an inert atmosphere [147, 148, 149, 150].

The effects of this treatment consist of the dissolving of the entrapped gas to the solidified metal and subsequent collapse of the pores. The plastic deformations inside treated components are densified and the microstructure gets homogenized. The pores are generally considered a crack nucleation site; therefore, the idea of HIP-induced pore closure is to increase the fatigue

strength of treated components. Noteworthy, the HIP treatment does not significantly transform the geometrical dimension and tolerances of the LPBF manufactured specimens [147, 150].

In the realm of Aluminium alloys, the HIP treatment is commonly administered at a temperature of 500 °C and a pressure of 100 MPa. Research has indicated that temperatures below 300 °C are insufficient for achieving optimal pore elimination. Despite evident pore closure, the strength of components subjected to HIP treatment has been observed to be subpar compared to their as-built counterparts. This discrepancy has been attributed to the globularization and coarsening of the microstructure in treated specimens, coupled with the failure of the previously present Si network within the eutectic of the as-built specimens [151, 152].

Noteworthy is the recurrent observation of pore re-opening in AlSi10Mg specimens following HIP treatment. The substantial fraction of re-opened porosity is attributed to the inadequate diffusion of entrapped gas from within the pores. Despite a reduction in pore diameter due to increased temperature and pressure, the remaining gas within the pores expands, potentially reinstating the pore diameter [148, 152].

It is crucial to highlight the contradictory effects of HIP on LPBF-manufactured aluminium, as reported in the literature. While some studies confirm improvements in fatigue strength, others describe a significant increase in ductility alongside an excessive decrease in strength, contrary to the anticipated enhancement in fatigue life [149, 150].

The notable reduction in strength observed in HIP-treated specimens stands out as a key disadvantage of this post-processing method. Existing literature suggests that this strength diminution can be partially mitigated through additional cycles of heat treatment [149, 150].

Exploring various combinations of HIP and subsequent heat treatments on the porosity and mechanical properties of AlSi10Mg components fabricated by LPBF has been a subject of investigation. However, discrepancies in published results regarding the effectiveness of such post-processing treatments persist. While certain studies propose that thermal treatment applied to HIP-treated specimens leads to significant pore re-opening and an increase in mechanical strength comparable to as-built specimens, others present more favourable outcomes. It is imperative to acknowledge the need for more extensive research in this domain to arrive at conclusive findings [153, 154, 155].

1.5.4. Thermal treatment

Heat treatments, in general, serve as efficient methods for modifying the mechanical properties of treated specimens to meet specific functions and applications. The alteration of mechanical properties primarily relies on inducing microstructural modifications [156, 157, 158, 159].

In the context of conventionally manufactured aluminium alloys, particularly AlSi10Mg, a set of guidelines has been established for heat treatment. The recommended methods for this alloy include the T6 treatment. The T6 method, serving as the primary thermal treatment for AlSi10Mg alloy, involves solution heat treatment followed by immediate water quenching, succeeded by a direct ageing cycle [160].

It is crucial to acknowledge that the T6 heat treatment is intricately designed to transform the microstructure and mechanical properties of conventionally manufactured aluminium alloys. However, the unique characteristics of aluminium alloys produced via LPBF method may introduce variations in the effectiveness of the T6 treatment. The significantly finer microstructure observed in LPBF-manufactured aluminium alloys can lead to reactions distinct from those commonly observed in conventionally manufactured aluminium parts when subjected to thermal treatments [156, 158].

It is worth noting that the thermal response of LPBF-manufactured aluminium components is not extensively studied under thermal loads. Consequently, understanding the behaviour of these components during thermal treatments, or generally under the thermal load remains an area requiring further investigation [155].

Current literature reports significant grain coarsening in LPBF-manufactured AlSi10Mg components imposed to T6 treatment. It is noteworthy that the metastable cellular microstructure in AlSi10Mg components manufactured by LPBF leads to phase transformation by decomposition after the material is subjected to heat treatment. Numerous authors have also reported the growth and concluding decrease of the number of Si precipitates within Ostwald's ripening phenomenon [161, 162, 163].

Notably, Ostwald's ripening phenomenon can be characterized by the dissolving of the small-sized Si particles, that subsequently deposit on the larger particles, which adversely lead

to coarsening of the Si precipitates. This process is led by the inclination of the particles to reach a more thermodynamically stable state since the surface-to-area ratio is minimised [163].

In a similar vein, the annealing process induces notable changes in the material's microstructure. Specifically, the finely delineated low-angle grain boundary sub-structures are eliminated through annihilation. This transformative effect can be ascribed to the recuperation of dislocation arrays inherent in the material's as-built state. The originally intricate network of Si surrounding the α-Al cells undergoes decomposition, forming Si spheroids. This results in a composite-like microstructure characterized by an Al matrix reinforced with Si particles [164, 165].

These microstructural modifications are further evidenced by pronounced material softening, heightened ductility, and diminished strength. Notably, the T6 treatment imparts alterations to the mechanical properties, particularly a decrease in strength, which may prove detrimental in diverse industrial applications, particularly those necessitating load-bearing capabilities [164, 165].

Conversely, the T5 heat treatment has been reported to enhance the mechanical strength of components manufactured through LPBF. However, contingent upon the applied temperature and treatment duration, the effects of T5 may include a substantial reduction in ductility [166].

Noteworthy, the AlSi10Mg specimens manufactured by LPBF are still commonly subjected to traditional methods of heat treatment, neglecting their microstructural and mechanical characteristics, possibly leading to lower efficiency of the heat treatment, or its overall detrimental effects. This practice can be explained by the current lack of knowledge regarding the heat treatment of LPBF-manufactured components [157, 158, 161].

Despite the extensive research on this topic, it is necessary to further study the possibilities to optimise the heat treatment directly for AlSi10Mg alloys, considering the microstructural characteristics in both prior and post treatment states. The optimization of heat treatment parameters is crucial for achieving the desired mechanical properties of AlSi10Mg alloys, and it is an active area of research in the field of additive manufacturing and materials science [154, 163, 164, 165].

Further research might lead to a better understanding of the post-process treatment of AlSi10Mg components manufactured by LPBF. Ideally, optimized parameters of conventional treatment processes, or development of the new post-process treatments, directly tailored to LPBF manufactured components might lead to further improvement of their quality and increased area of application of this manufacturing method [157, 158, 159].

1.5.5. Thermo-mechanical treatment

Friction stir processing represents the most recent metalworking technique that might be successfully applied to LPBF-manufactured AlSi10Mg components with the objective of homogenizing their microstructure, suppressing the porosity, and providing localized specific property enhancement. This metal working technique utilizes the same process principles as friction stir welding, where the fusion of two components is secured by flow of heated and softened material supported by the contact with rapidly rotating tool [160, 161, 162].

The friction stir processing (FSP), however, instead of joining the specimens, locally modifies the microstructure of monolithic specimens induced by plastic material flow. During the FSP treatment, the processed material is heated to the temperature of around 80% of the melting point, plastically deformed and driven to flow by the contact friction between the non-consumable tool and base material. An example of the processing setup is demonstrated in Figure 11. The common effects of FSP treatment, when applied to LPBF-manufactured specimens, include grain refinement and microstructure homogenisation, porosity suppression, ductility improvement, fatigue life enhancement, and local modification of residual stresses [160, 162].

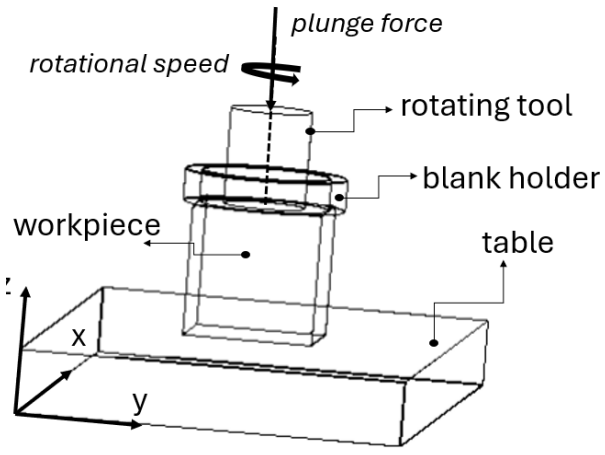

Figure 11 Processing set-up of FSP treatment

Several research groups have confirmed the homogenizing and densifying effects of FSSP on specimens manufactured using MLPBF. Scherillo et al. [163] described the breakage in layer-wise morphology and homogenization of both micro- and macrostructures in friction stir-welded AlSi10Mg plates fabricated by SLM. Huang et al. [164] confirmed the transformation of the microstructure in Ti6Al4V specimens processed by the tool with rotational speeds over 400 rpm. The initial porosity of processed specimens was significantly suppressed, and the ductility was greatly improved. Maamoun et al. [165] compared the ability of hot isostatic pressing (HIP) and FSSP to densify the structure of AlSi10Mg, finding that the densification of the microstructure of specimens processed with FSP was significantly more efficient. Lv et al. [166] described the transformation of residual stresses in selectively laser melted specimens after FSSP treatment. The FSP caused an increase in residual stresses with a typical M-shaped distribution. Perard et al. [167] applied FSP to martensitic steel specimens with copper cold spray coating, and FSP demonstrated the ability to densify the microstructure and homogenize the coating layer.

On the other hand, the final effects of the FSP treatment, together with the effective depth of processing, vastly depend on the applied process parameters (plunge depth, processing speed, rotating speed, plunge force) and working set-up (presence and geometry of pin, the standard-, or spot processing set-up, refill-type of processing, etc.). While current literature already includes few sources directly describing the effects of FSP treatment in specimens manufactured by LPBF technique from AlSi10Mg alloy [168, 169, 170], this area still requires further investigation.

Considering the working mechanism of this processing technology, in which a rapidly rotating tool is pressed against the surface of the specimen, it is not surprising that this thermo-mechanical treatment might result in defects distortions of different ranges and types (Figure 12). Several parameters, including plunge force, pin usage, pin geometry, etc., influence the range and type of distortions in processed specimens. Numerous researchers suggested that increasing the plunge depth and using a pin can negatively impact the geometric accuracy and surface integrity of the processed specimen [161, 165].

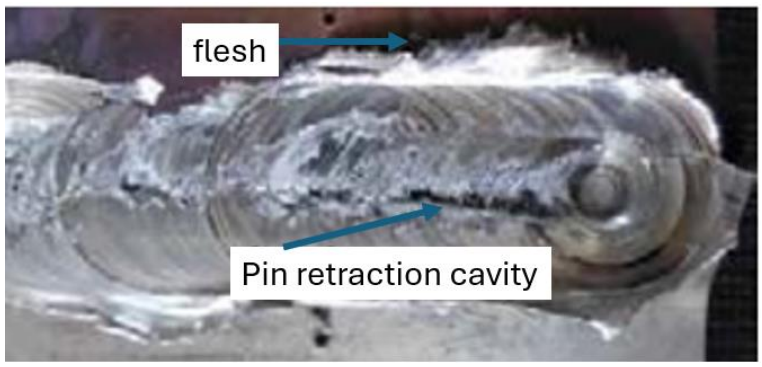

Figure 12 Defect and deformations in FSP-treated specimen

Notably, the distortions of processed components arising from material flux in FSP treatment may pose a challenge in applications that require precise dimensional accuracy. Therefore, it is imperative to conduct meticulous research uncovering the material flow during FSP treatment in specimens manufactured via LPBF. Striking a balance between an appropriate effective depth and acceptable deformation is essential for evaluating the effectiveness of the FSP treatment. Understanding the material flow and resulting deformations induced by FSSP processing with different parameters represents a key precursor to further industrialisation of the FSSP treatment as an efficient post-processing technology for LPBF manufactured components. In contrast, the current lack of research regarding this topic might be considered an obstacle to the widespread application of FSP treatment to LPBF-manufactured components. [162, 164, 169].

Since the LPBF-manufactured components often require good geometrical accuracy, the FSP process optimization, including testing of novel processing set-up, should be considered. More research attention should be given in finding a balance between the effective depth of processing and induced deformation.

1.6. Numerical modelling and Finite Element Analysis (FEA) of LPBF manufacturing with Aluminium alloys

Numerical modelling represents an important tool in enhancing the reliability of the LPBF manufacturing process. Predicting the outcomes of manufacturing considering various process parameters, aspects of the environment inside the building chamber, etc. holds the potential to minimize the defects and residual stresses, increase the precision and minimize the risk of failure of the building component. The numerical modelling might thus represent a significant

economical and environmental benefit, as it prevents the potential material and energy waste [167, 168, 169, 170].

In the realm of LPBF, a multitude of intricate and dynamic physical phenomena unfold, underscoring the inherent complexity of the process. Given the constraints imposed by the computational capabilities of common computers, the imperative arises to consciously integrate simplifications into numerical models. Consequently, these models are tailored to different scales—micro, meso, and macro—reflecting the need to strike a balance between computational efficiency and accuracy [168, 169].

It is essential to emphasize that the level of detail incorporated into these numerical models is intrinsically tied to the computational cost. Consequently, the precision of a model corresponds directly to its computational demands. As a pragmatic consequence, the most refined numerical models find application in the analysis of short, single-track manufacturing scenarios, where intricacies are portrayed with careful attention. Conversely, macroscale models, characterized by a higher degree of abstraction, are adept at simulating the manufacturing of full-sized components. This tiered approach ensures that computational resources are allocated optimally, matching the intricacy of the model to the specific requirements of the manufacturing scenario at hand [167, 169, 170].

1.6.1. Microscopic approach

The microscopic modelling approach employed for simulating the LPBF manufacturing process achieves an unparalleled level of detail among all computational methodologies. Notably, numerical models operating at the microscopic scale exhibit the utmost complexity, resulting in the highest computational cost when compared to models at other scales [171, 172].

The microscopic models frequently deal with materials on the particle level. Although there is ongoing research regarding the simulations of powder particle distribution within the powder bed, this topic still remains quite a challenge. It should be highlighted that accurate particle distribution is an important precursor for the high accuracy of the simulated porosity, powder denudation processes, melt pool dynamics, etc. In order to reach satisfactory results, the raindrop method, or the recoater simulations are commonly applied [171, 172, 173].

Within the raindrop method, falling powder particles aim to reach a local minimum in potential energy. When coming into contact with another particles, the falling particles start to

rotate as necessary while ultimately, they are either settling in place at the local minimum or falling until reaching the global minimum. In contrast, the recoater simulations are mainly based on Discrete Element Methods (DEM). The DEM considers the motion of the individual particles and their effects on one another, including e.g., the Van der Waals forces, gravity, and friction between them [174, 175].

Moreover, microscale models detailly describe the interaction of the powder bed with the laser beam. The laser beams, considered primary heat sources, are described by various techniques, although the Goldak expression is one of the most commonly used ones [171, 172, 173, 176].

The Goldak heat source considers the energy distribution as ellipsoid, including the heat flux in front part (qf) and rear part (qr), as it is depicted in Figure 11. The total energy distribution is thus the sum of the heat fluxes in the front and rear parts (4, 5, 6) [176].

$$Q(x,y,z) = q_f(x,y,z) + q_r(x,y,z) \quad (4)$$

$$q_f = \frac{6\sqrt{3} f_f IUe}{x_f bd\sqrt{\pi}} * \exp\left(-\frac{3(x-vt)^2}{x_f^2} - \frac{3y^2}{b^2} - \frac{3z^2}{d^2}\right) \quad (5)$$

$$q_r = \frac{6\sqrt{3} f_r IUe}{x_r bd\sqrt{\pi}} * exp\left(-\frac{3(x-vt)^2}{x_r^2} - \frac{3y^2}{b^2} - \frac{3z^2}{d^2}\right) \quad (6)$$

Where f_f and f_r represent the power fraction of front and rear part, respectively. Notably, the sum of both is equal to 2. The x_f and x_r are the front and rear ellipsoid semi-axe, respectively, while b and d stand for width and depth of the heat source [176].

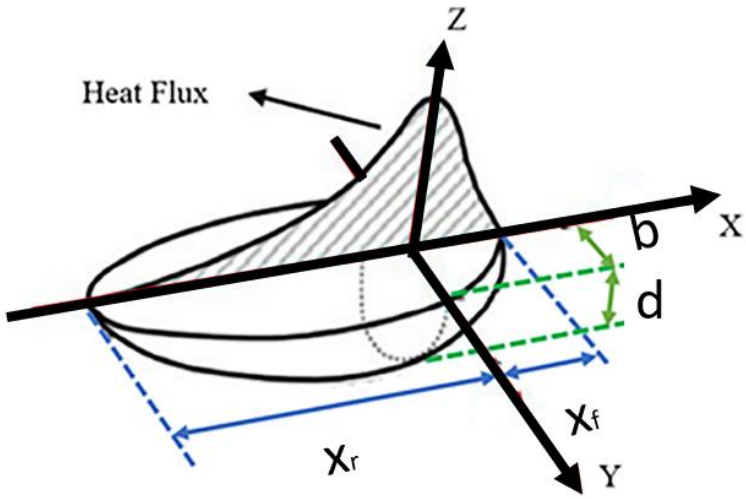

Figure 13 Goldak heat source

As the response to the laser irradiation, the microscale numerical models describe the phase change of the material, as well as natural and forced heat conduction and heat irradiation. Notably, the emissivity of a powder bed surface can be only assumed by considering the packing density of the powder bed, and the emissivity of the material in its solid phase. On the other hand, the heat loss due to ablation is mainly determined in respect to the mass of the ablated material [177, 178].

The phase change interface is governed by the latent heat, expressing the enthalpy and specific heat capacity of the material in solid state, solid-liquid hybrid state and liquid state, where the liquid state usually also recognize between melts and vapours. Consequently, the evolution of the melts-vapours interface is mainly defined using evaporation rate. In continuum heat flux coupled models, the mushy zone is mainly considered a homogeneous porous medium, while the liquid phase is considered a Newtonian fluid with incompressible flow [179, 180].

Depending on the complexity of each numerical model, the fluid flow is portrayed to be subjected to several forces, such as buoyancy, the Darcy's term or the surface forces. Majority of microscale numerical models describe the buoyancy forces by the Boussinesq approximation and Darcy term by the Kozeny equation. Finally, the large fraction of the microscale numerical models portray the surface forces as the sum of the surface tension term, capillary forces and Marangoni effect, and recoil pressure terms [181, 182].

The stress field calculation is usually coupled with the heat conduction model and is it based on the thermoplastic theory, including yield criterion, flow criterion and hardening criterion [171, 173, 174].

The microscale numerical models are governed by mass, momentum, and energy conservation equations [173, 174, 175, 176, 177, 178].

The special feature of the microscale models is represented by the prediction of the microstructure. While it is well known that the microstructure is mainly influenced by the thermal gradient and solidification rate, there are currently 3 distinctive numerical methods commonly applied in microscale models to simulate the microstructural evolution: deterministic method, randomness method and direct simulation method [183, 184, 185, 186, 187].

The deterministic method applies supercooling, solute supersaturation and thermophysical properties of materials as the main parameters determining the microstructural evolution. This numerical method also divides the solid and liquid phases according to the temperature field distribution, mainly applying molecular dynamics (MD). In contrast, the randomness method adopts the principles of the probability theory, and nucleation and crystal growth are considered random events. The randomness method usually applies the Monte Carlo (MC) or cellular automata (CA) methodology. Furthermore, the direct method simulates the heat transfer, mass transfer and phase transition through unified mathematical and physical equations and solves the solid-liquid interface in the process of numerical calculation. The commonly used direct simulation methods include level set method (LS) and phase field method (PF) [183, 184, 187].

Notably, the current state of computational technology poses a significant size restriction to numerical simulations using a microscopic approach. Therefore, it is still difficult to determine e.g., porosity in larger scales. The level of adversity of computation is further increased by statistical variation and missing of sufficient material data in the literature. The accurate prediction of surface roughness, mechanical and physical properties, fatigue life, melt-pool dynamics, and porosity remain a distant goal [171, 172, 173].

1.6.2. Mesoscopic approach

The mesoscopic approach in LPBF simulations typically treats the powder bed as a continuous porous medium, disregarding the individual characteristics of powder particles.

Consequently, numerical models at the mesoscale often neglect the powder denudation dynamics, the influence of powder granulometry distribution, and interactions between powder particles and the laser beam. Although mesoscopic simulations primarily focus on the formation and dynamics of melt pools, they employ simplifications that neglect certain physical phenomena [188, 189].

Similar to the microscopic approach, the interaction between the laser and the powder bed in mesoscopic simulations is described using transient heat transfer. The heat source is commonly modelled with Gaussian or Goldak-like distributions. In contrast, mesoscale approaches tend to overlook heat loss due to material ablation. While phase change is typically modelled similarly to the microscopic approach, some authors either entirely neglect or highly simplify the dynamics of the gas phase. Consequently, a significant proportion of mesoscopic models fails to accurately portray recoil pressure and buoyancy forces within melt pools [188, 189, 190].

Despite sharing fundamental features with microscopic models, mesoscopic approaches involve simplifications or the neglect of specific physical effects. The computational advantage of mesoscale simulations, characterized by considerably lower costs compared to microscopic approaches, enables the simulation of larger, multi-track, and multilayer components [188, 189, 190].

In mesoscopic numerical models, the deposition of new layers is often described using either the death-and-birth or inactive method. In the death-and-birth method, non-deposited layers are present throughout the simulation but are "killed" by assigning material properties that do not influence the computation. Upon material deposition, these layers are activated, "born" with real material properties. In contrast, the inactive method includes only deposited elements in the model, with non-deposited elements added incrementally during the layer deposition process [191, 192].

The characteristic feature of mesoscale numerical models in LPBF manufacturing is the pursuit of equilibrium between a high level of detail and a desirable computational cost. Despite the considerable research and numerous mesoscale models, there remains a need for novel numerical models that provide fast and reliable predictions of defect formation and distortion distribution in LPBF-manufactured components, especially those with larger

dimensions. Ongoing efforts should focus on addressing this gap in order to advance the accuracy and efficiency of LPBF simulations [188, 189, 190].

1.6.3. Macroscopic approach

The macroscale approach is a widely employed method for simulating the LPBF manufacturing process, particularly in predicting distortions and residual stresses across full-sized components. In these simulations, the complexity of physical phenomena within the manufacturing process is significantly reduced, yet the models consistently demonstrate rapid and reliable predictive performance [193, 194, 195, 196].

Depending on the size of the component under simulation, individual layers are typically grouped into higher meta-layers, comprising generally 3 to 10 single layers, which are deposited simultaneously. Similarly, the heating of these deposited layers is infrequently represented through interaction with a Gaussian or Goldak heat source. More commonly, the meta-layers are concurrently heated by applying heat flux based on energy equilibrium. Some researchers opt to depict the laser-powder bed interaction by setting the initial temperature of the heated meta-layer equal to the peak temperature during manufacturing, followed by allowing the meta-layer to cool through radiation and heat conduction [194, 195].

The derived thermal history is subsequently utilized to ascertain thermal strains and stresses. The prevalent method for stress and strain prediction in additively manufactured components within macroscale numerical models is the inherent strain method. This approach considers residual strains in the material as the source for the formation of residual stresses, in accordance with Hooke's law. It is noteworthy that in a significant fraction of finite element models, residual strains are represented by plastic strains [197, 198].

Macroscopic numerical models often incorporate coupling between thermal and mechanical solvers, with thermal expansion serving as the coupling feature between these computational domains. Such coupled thermomechanical models on the macroscale consistently offer swift and dependable predictions of residual stresses and distortions in LPBF-manufactured components without necessitating calibration. Alternatively, exclusively mechanical models grounded in the inherent strain method are available, albeit requiring prior experimental calibration. This calibration typically involves the experimental manufacturing of three or more callipers, followed by measuring distortions at predetermined points [199].

Despite the aforementioned advantages and capabilities of numerical models employing the macroscale approach, certain limitations have been identified. Notably, macroscale models are incapable of providing information regarding microstructure, surface characteristics, melt pools, or evaporation dynamics in LPBF-manufactured components [200].

1.6.4. Numerical modelling of post-process treatment of Aluminium components manufactured by LPBF

In the realm of post-processing treatments for Aluminium specimens produced by LPBF, it is notable that while a variety of treatments are commonly employed, only a small fraction of research has been dedicated to the development of numerical models investigating the specific impacts of these treatments on material characteristics. The small number of available numerical models may be linked to the recognized knowledge gap pertaining to post-processing treatments, as described in section 1.5. [201, 202, 203].

Despite the conspicuous lack of numerical models in this domain, a handful of researchers have proffered diverse findings concerning numerical models for both thermal and mechanical treatments. Warnken et al. assert that the modelling of heat treatment necessitates the anticipation of the thermal history within the furnace. Given that a majority of furnaces operate in a vacuum, the predominant mode of heat transfer from the heating elements to the treated components is radiation. Particularly for highly reflective Aluminium and its alloys, the reflective nature must be considered when modelling this radiation. A nuanced understanding of the thermal history of treated components holds the potential to enhance the optimization of power in heating elements for controlling thermal gradients or determining optimal part positioning in the furnace to avert shading and cold spots. Utilizing the predicted thermal history can further facilitate the computation of microstructure evolution and contribute to the formulation of the most suitable thermal cycle [204].

Conversely, numerical modelling of mechanical treatments poses substantial challenges, primarily attributable to the rapid dynamics of the process and extensive plastic deformations leading to mesh distortion and ensuing convergence issues. Consequently, various authors advocate for the adoption of alternative computational methods to address these complexities [204].

Similarly, in the intricate problem thermos-mechanical processing of LPBF-manufactured parts, several aspects with high computational demands have been identified. These include the anisotropic microstructure and contact properties between the part and the processing tool, among others. Additionally, the rapid and significant plastic deformation experienced by processed components adversely affects the convergence behaviour and overall processability of conventional Finite Element Method (FEM) numerical methods with static mesh [205, 206].

Consequently, it is necessary to consider alternative numerical strategies incorporating adaptive mesh to strike a balance between the precision and time effectiveness of numerical simulations for friction stir spot processing [207, 208].

The Augmented Lagrangian method (ALM) has been widely employed to address the minimization problem and effectively model the contact and friction between two distinct bodies, namely the workpiece and the tool. By utilizing successive unconstrained minimization, the authors addressed the constrained minimization problem, assigning physical significance to the Lagrange multipliers as contact forces. This enabled the examination of friction conditions while ensuring accurate solutions. Additionally, the introduction of a penalty parameter, influencing the numerical conditioning directly, played a pivotal role in enhancing convergence behaviour [209, 210].

To further enhance convergence behaviour, the implementation of adaptive mesh or adaptive updates for penalty parameters might provide a significant advantage. Numerous researchers have obtained satisfactory outcomes by utilizing ALM to compute friction between elastic bodies or combinations of elastic and rigid bodies. However, when incorporating elastoplastic materials, the convergence issues still persisted, demanding continual monitoring [211, 212].

To enhance the accuracy, efficiency, and feasibility of numerical modelling in friction stir welding/processing, an arbitrary Lagrangian-Eulerian numerical (ALE) method was introduced. Guerdoux and Fourment (2005) utilized a splitting method within ALE, first calculating material velocity and pressure fields, followed by mesh velocity, and solving the advection terms. They investigated different methods of nodal variable transport in their study [213, 214]. Schmidt and Hattel (2005) developed a numerical model using the ALE formulation to establish the quasi-stationary thermomechanical state of the workpiece. They

reported reduced computational costs and no convergence issues, but void formation within the workpiece could not be simulated [215].

More recently, several authors employed the coupled Eulerian-Lagrangian (CEL) numerical method to further reduce computational costs and address significant mesh distortion problems. The CEL method utilizes the Lagrange-plus-remap algorithm, which operates in two steps. First, material deformation is captured through mesh distortion with Lagrangian increment. Second, the mesh is restored by calculating material flow between nodes and subsequent remapping. Numerous research groups have demonstrated good agreement between experimental results and CEL-calculated results, including the ability to track burr and void formation, as well as large and rapid deformations [216, 217, 218, 219].

Currently, the research community is engaged in an ongoing discussion regarding the benefits and disadvantages of ALE and CEL numerical methods. While several distinctions in the predictive capacities of both numerical approaches are recognized, it remains unclear which method is more efficient [220].

The availability of fast and reliable numerical models of post-process treatment, specifically tailored for Aluminium components manufactured by LPBF holds the potential to improve the general knowledge of effects of post process treatment and co-create the process window with optimal effects on desired characteristics of treated components. At the same time, the numerical models might prevent the material- and energy waste that would be otherwise created by application of unoptimized post-process treatment [201, 202, 203, 204].

1.7. Motivation

The current level of awareness and state-of-the-art of LPBF manufacturing with Aluminium alloys described in the previous section of this dissertation suggest the existence of the knowledge gap. We have identified several phenomena and aspects of LPBF manufacturing with Aluminium alloys that are still not well discovered and described, such as the distinctive process-structure-property threshold, the effect of processing parameters on the distribution of residual stresses and distortions, and the behaviour of LPBF-manufactured components under the thermal load.

Consistent with the latter parameter, we have identified the significant lack of awareness of the research community regarding the thermal treatment, and post process treatment of

Aluminium components manufactured by LPBF in general. To our knowledge, the HIP represents the only treatment that is focused directly on additively manufactured components and the current literature does not provide the unambiguous overview on its effectivity when applied to Aluminium alloys manufactured by LPBF. Therefore, the development of the novel techniques of post-process treatment, considering the distinctive characteristic of LPBF specimens, and providing the sufficient effective depth might be considered highly beneficial.

Despite the existence of various numerical models, there is still a pressing need for fast and reliable solutions, able to predict formation of residual stresses and distortions, defects, melt pool dynamics. The numerical models simulating the post-process treatment of LPBF-manufactured specimens represent a special category of numerical tools, that is not well betoken in current literature.

The further research and rigorous studies regarding these topics hold the potential to improve the reliability of the LPBF manufacturing method. Such knowledge enhancement might have significant industrial consequences, leading to progressed applicability of LPBF, and increased area of application.

1.8. Objectives and outline

The main objective of this dissertation is to enhance the level of knowledge regarding the LPBF manufacturing process with the Aluminium alloys by addressing the points identified in section 1.7. The objectives of the thesis correlate with its outline. Therefore, the dissertation is sectioned as follows.

- Second chapter is focused on the characterisation of the AlSi10Mg specimens manufactured by LPBF. This section contains the mechanical, optical, and thermal characterisation of the AlSi10Mg components using various methods, including destructive, and non-destructive tensile testing, microhardness characterisation, physical simulation of the behaviour of the sample under the thermal load. The porosity of the specimen discovered by optical analysis will be further confirmed by the relative density testing using Archimedes method.

- Third chapter is focused on the development of the mesoscale numerical model of LPBF manufacturing process with AlSi10Mg alloy, focused on the prediction of lack-

of-fusion type of porosity. The numerical model was validated by the comparison of simulated and experimental dimensions of melt pools in specimens manufactured with 9 different combinations of process parameters.

- Fourth chapter is oriented in experimental and numerical investigation of the effects of the position of the AlSi10Mg cubical specimens on the building platform on their geometrical dimensions, tolerances, and surface characteristics.

- Fifth chapter introduces the novel post-process treatments for LPBF-manufactured AlSi10Mg alloy components, the pinless friction stir spot processing (P-FSSP). The chapter studies the effects of the treatment on the level of porosity and microstructural characteristics of the treated component. At the same time, the chapter determines the effects of P-FSSP processing parameters on the deformation of the treated parts, flash formation, and the effective depth of processing. The statistical methods are used to determine the optimal processing window resulting in the sufficient effective depth and minimal deformation of the processed parts. The experimental campaign was reproduced in numerical simulations employing the commercial software Simufact Forming using Arbitrary Lagrangian-Eulerian (ALE) numerical approach.

- Sixth chapter is focused on the development of the original numerical model of P-FSSP treatment of AlSi10Mg specimens manufactured by LPBF. The designed numerical model employs and discusses the coupled Euler-Lagrangian mathematical formulation in prediction of material flow and defect formation/suppression in the treated specimen. The developed numerical model was validated by the comparison of simulated results with the experimental ones, introduced in the chapter 5.

- Seventh chapter provides the summary of the work done, draws the conclusions and suggests the future works.

2. Characterisation of the AlSi10Mg alloy manufactured by LPBF

This chapter provides a comprehensive overview of the intricate characteristics and behaviour exhibited by AlSi10Mg alloy specimens produced through the Laser Powder Bed Fusion process. While the LPBF technique has become a common method for processing the AlSi10Mg alloy, the literature lacks a thorough description of certain aspects and characteristics associated with this alloy when subjected to LPBF. The AlSi10Mg alloy, recognized for its concurrent strength and lightweight properties, holds significant industrial promise. Nonetheless, certain physical attributes of this alloy pose challenges in its LPBF processing. This presents a potential obstacle to its widespread industrial application, considering that LPBF markedly alleviates the geometric constraints inherent in conventional manufacturing methods.

This chapter presents the initial findings derived from optical analysis, microhardness testing, standard destructive and non-destructive analyses of tensile behaviour, examination of relative density, and evaluation of specimen response to thermal loading. The ensuing analysis highlights the distinctive features of the AlSi10Mg alloy processed by LPBF, with a focus on its characteristic microstructure, identification of defects, mechanical properties, and the intricate relationships between them.

2.1. Experimental procedures

2.1.1. Manufacturing of the specimen

Five cylindrical specimens made of AlSi10Mg were manufactured utilizing an EOSINT M270 production system, which features a fiber laser boasting a maximum power of 200 W and a laser spot diameter of 90 µm. Each specimen measured 120 mm in total length and 10 mm in diameter, as visually depicted in Figure 14.

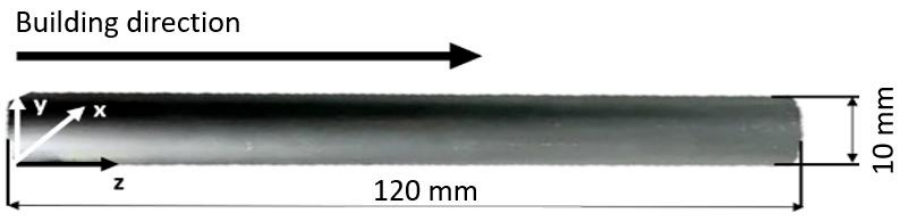

Figure 14 LPBF-manufactured AlSi10Mg specimen

Throughout the construction phase, the building chamber was meticulously supplied with a vacuum argon medium, effectively diminishing the oxygen content to below 0.1%. Simultaneously, the building plate underwent pre-heating to a temperature of 200 °C, a measure implemented to mitigate residual stresses. The determination of process parameters was guided by the supplier's recommendations for the specific material in question, outlined in Table 2.

Table 2 LPBF-process parameters

	Laser power [W]	**Scanning speed** [mm/s]	**Layer thickness** [µm]	**Hatch distance** [µm]
Skin	120	900	30	0.1
Core	195	800	30	0.17
Contour	180	900	-	-

Conclusively with the applied manufacturing method, the AlSi10Mg alloy, as the feedstock material was preliminary in the powder state. The powder, supplied by EOS, had a size distribution in a range from 25 to 70 µm, and a chemical composition as depicted in Table 3.

Table 3 Chemical composition of AlSi10Mg powder

Element [%]										
Al	Si	Fe	Cu	Mn	Mg	Ni	Zn	Pb	Sn	Ti
balanced	9-11	0.55	0.05	0.45	0.25-0.45	0.05	0.10	0.05	0.05	0.15

During the building process, the specimens were oriented lengthwise, and their distribution on the building plate was as demonstrated in Figure 15.

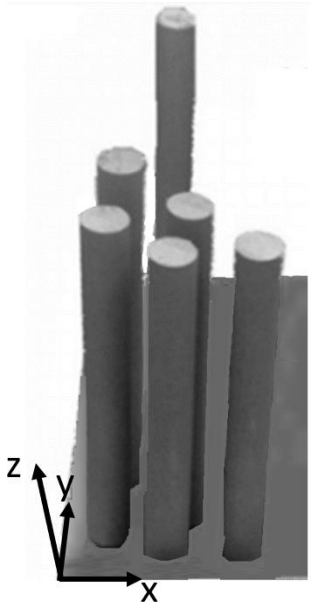

Figure 145 Distribution of the specimens on the building plate

2.1.2. Material testing

2.1.2.1. Characterisation of the relative density

Considering the porosity being the common defect in specimens manufactured by the LPBF method, the specimen in its as-built state underwent testing to determine its relative density. The Archimedes method, as depicted in Figure 16, was employed for this purpose.

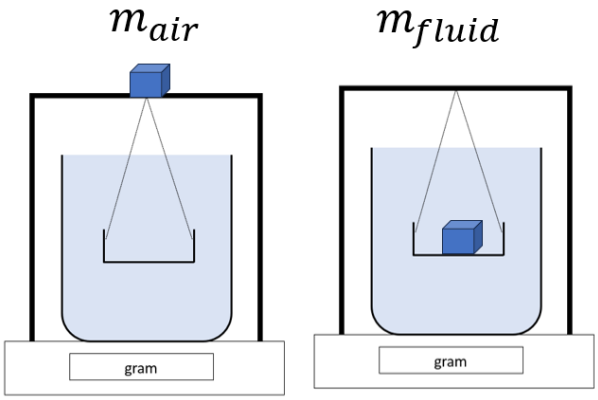

Figure 16 Archimedes method

The testing consisted of two distinct phases. Initially, the weight of the specimen was measured in an atmospheric setting, followed by a subsequent measurement in a submerged state within a water medium. The relative density of the specimen ($\rho_{specimen}$) was calculated as in (7).

$$\rho_{specimen} = \rho_{fluid} \frac{m_{air}}{(m_{air} - m_{fluid})} (7)$$

Where ρ_{fluid} is the density of applied water medium, m_{air} is the weight of the analysed specimen in air and the m_{fluid} is the weight of specimen in the fluid. Finally, the level of porosity was calculated as in (8).

$$Porosity = 100 - (\frac{\rho_{specimen}}{\rho_{AlSi10Mg}} .100) [\%] (8)$$

2.1.2.2. Metallography

The microstructure of the manufactured sample was examined in transverse and cross sections in as-deposited and etched conditions by means of optical microscopy. The sample underwent conventional microscopic preparation with an etching solution of Keller's reagent (1% HF+1,5% HCl + 2,5% HNO3 + 95% H2O).

2.1.2.3. Testing of the tensile properties

Initially, the tensile properties of the AlSi10Mg specimens were assessed non-destructively, using the methods of the acoustic characterisation. Within the experimental characterisation, contact tests in pulse-echo mode were conducted. Notably, it was not necessary to exploit the property of acoustic refraction, as we used a transducer to generate longitudinal waves and one for transverse waves. The experimental set-up was as depicted in Figure 17.

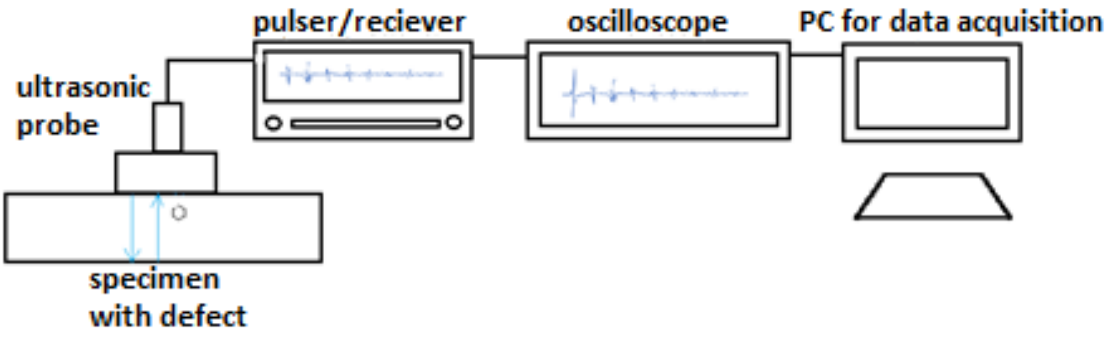

Figure 17 Ultrasonic contact pulse-echo set-up

During the experimental campaign, the time of flight (TOF) characterizing the time in which the ultrasonic wave travels from a source (transducer) into the tested medium and back, for both longitudinal and transverse waves was measured. Subsequently, considering the

measured TOFs and known thickness of the sample, which represents the spatial path of the wave in the material, the ultrasonic velocities of the longitudinal and transverse waves, respectively, were obtained (9).

$$v = \frac{2s}{TOF} \quad (9)$$

where 2s represents the wave path (the double of the thickness of the material) and TOF is the time of flight.

Finally, assuming the theoretical model of isotropic material, known the material's density and using the measured velocities, the Young's modulus (E), the shear modulus (G), the bulk modulus (B) and Poisson ratio (ν) were calculated as follows (10, 11, 12, 13) [205, 206].

$$E = \frac{\rho v_t^2 (3v_l^2 - 4v_t^2)}{v_l^2 - v_t^2} \quad (10)$$

$$G = \rho v_t^2 \quad (11)$$

$$B = \rho(v_l^2 - \frac{4}{3}v_t^2) \quad (12)$$

$$\nu = \frac{1-2(\frac{v_t}{v_l})^2}{2-2(\frac{v_t}{v_l})^2} \quad (13)$$

where v_l is the velocity of the longitudinal wave, v_t is the velocity of the transversal wave and ρ is the density of the tested material.

Notably, the tensile properties of the LPBF-manufactured AlSi10Mg specimens were measured in 4 different points in 2 different directions, as it is depicted in Figure 18.

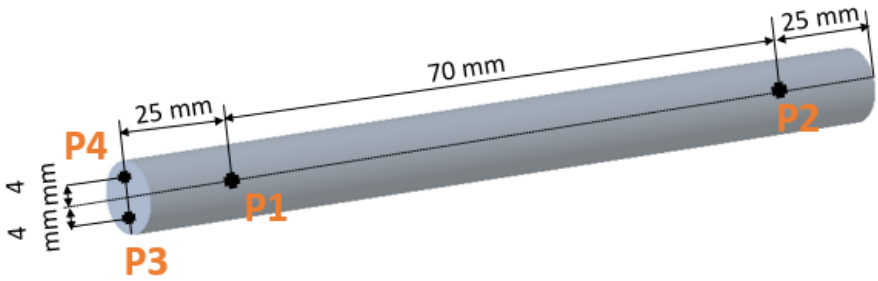

Figure 18 Distribution of measuring points for ultrasonic testing

With the aim to mitigate the reflection of singular microscopic pores, suppress the amount of the noise, and thus overall improve the readability of the ultrasonic signal, the pulse frequency of contact transducers was chosen to be 2,5 MHz. The imposed value of pulse

frequency was in agreement with the general guidelines for acoustic characterisation of the LPBF-manufactured materials, where a lower frequency is advised.

Additionally, the tensile properties of the specimen in the axial direction were assessed by conventional destructive tensile test following ASTM E8 standard, using INSTRON 5869 universal testing machine (Instron, USA), as it is demonstrated in Figure 19.

Figure 19 Tensile testing

2.1.2.4. Microhardness testing

In order to verify the anisotropic nature of the LPBF-manufactured AlSi10Mg specimens, the microhardness test across the several regions of the perpendicular section of the specimens were conducted. Microhardness tests were done with a load of 0.3kgF for a duration of 15 seconds.

2.1.2.4. Behaviour of the specimen under thermal load

The specific thermal response to the elevated temperature of AlSi10Mg specimens manufactured by LPBF technique was examined in physical simulations. Three different types

of thermal loads were applied using the Gleeble 3800 physical simulator, as outlined in Table 4. The thermal loads included a heating phase (from 20 °C to 500 °C), a holding phase (maintaining a constant temperature of 500 °C), and a cooling phase (from 500 °C to 20 °C). It is important to note that subsequent analysis revealed that the physical simulator was unable to achieve the desired cooling rate, thus the thermal behaviour during the cooling phase could not be evaluated. The physical simulation system employed two thermocouples: one for heating the specimen using Joule heating principles, and another to measure the instantaneous temperature of the specimen (Figure 20).

Table 4 Imposed thermal loads

Thermal load	**Heating rate** [°C/s]	**Keeping phase time** [s]	**Cooling phase** [°C/s]
TH1	10	60	10
TH2	7.5	80	7.5
TH3	6	240	6

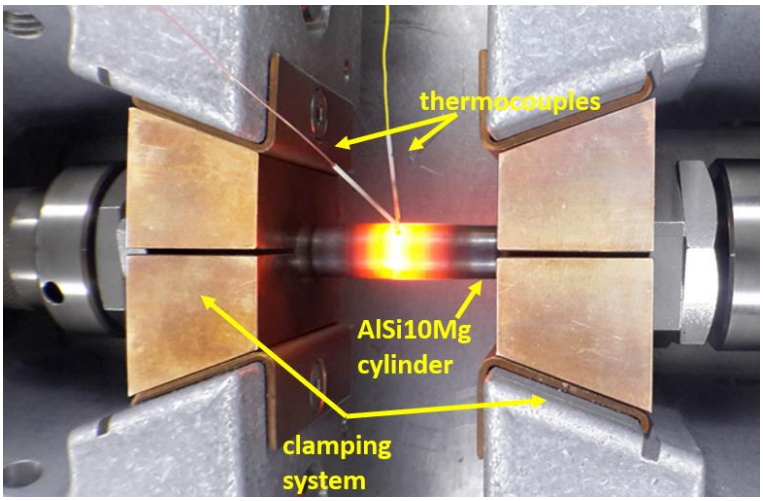

Figure 20 Working set-up of physical simulation

The measured (T_m) and imposed (T_i) temperatures were subsequently analysed, their difference (T_{diff}) for each time step was calculated (14), and the T_{diff} over the imposed temperature was plotted.

$$T_{diff} = T_m - T_i \quad (14)$$

2.2. Results and discussions

2.2.1. Porosity, defects, and heterogeneous microstructure

Table 5 shows the measured weight of the specimen in both air and water medium assessed within the Archimedes method, as well as the calculated density of the sample, and the density of the AlSi10Mg material, stated by the powder supplier. It is noteworthy that the level of porosity was subsequently calculated to be 2.66%.

Table 5 Characteristics of the LPBF-manufactured AlSi10Mg specimens investigated by the Archimedes method

m_{air} [g]	m_{fluid} [g]	$\rho_{AlSi10Mg}$ [kg/m^3]	$\rho_{specimen}$ [kg/m^3]
39.89	24.47	2670	2598

Moreover, optical analysis unequivocally confirms the presence of porosity, as depicted in Figure 21. Notably, the AlSi10Mg samples produced through LPBF exhibit a distinct prevalence of both lack-of-fusion defects and metallurgical porosity. The lack-of-fusion defects manifest predominantly as elongated structures with an approximate cross-sectional length of 140 µm or as spherical formations with a larger diameter of approximately 26 µm, discernible in the transverse section of the specimen. Conversely, metallurgical porosity is characterized by spherical formations with a diameter of approximately 8 µm, evident in both transversal and cross-sectional views of the specimen. This distinctive combination of lack-of-fusion defects and metallurgical porosity underscores a notable trait in the LPBF-manufactured AlSi10Mg samples.

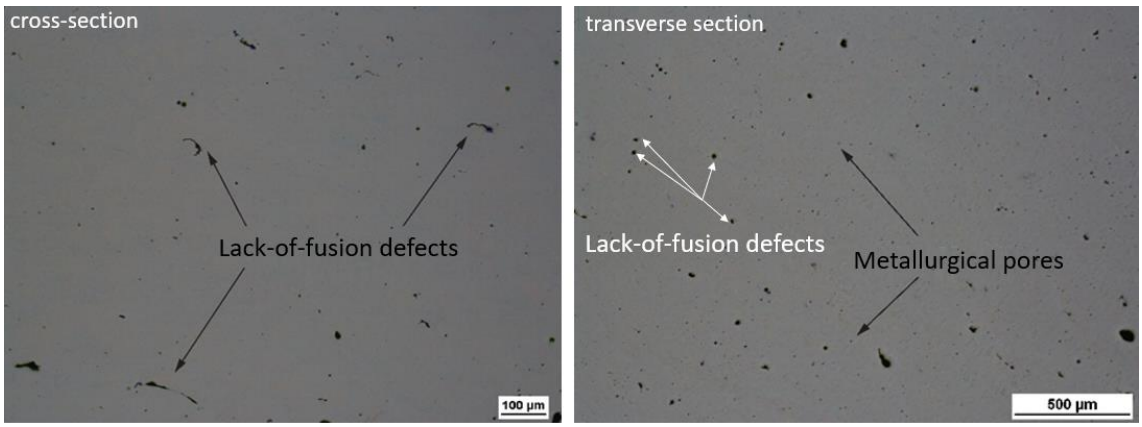

Figure 21 Porosity and lack-of-fusion defects observed on cross- and transverse section of the LPBF-manufactured AlSi10Mg specimen

The prevailing literature indicates that the computed porosity levels primarily arise from metallurgical pores, with the voids resulting from a lack of fusion predominantly filled by

unfused powder, while metallurgical pores tend to remain empty. Consequently, the applicability of the Archimedes method in ascertaining porosity levels in specimens produced through LPBF is inherently constrained, as it notably underestimates the volume of lack-of-fusions, as documented in references [32, 103, 108].

It is crucial to emphasize that although a discernible degree of porosity and lack-of-fusions is commonly observed in LPBF-manufactured specimens, the potential effects on the mechanical properties of the fabricated components should not be overlooked. A comprehensive understanding of the existing porosity levels is imperative to ensure the requisite structural integrity for the subsequent application of the manufactured components [103, 109, 110].

Moreover, the optical microscopy analysis unequivocally substantiates the pronounced heterogeneity inherent in the AlSi10Mg components fabricated through LPBF technique, as visually depicted in Figure 22. The transverse section of the specimen prominently exhibits distinctive half-cylindrical structures, attributed to the solidified melt tracks. Despite the discernible metallurgical cohesion observed among these melt tracks, a noteworthy presence of microvoid structures is identified. This optical inspection additionally verifies the well-documented phenomenon of epitaxial grain growth reported in the literature [37, 89, 95, 116, 117].

Similarly, the cross-sectional examination of the specimens reveals prolonged structures, unequivocally linked to the solidified melt tracks. A nuanced classification of four distinct regions, each characterized by disparate microstructures, emerges upon closer inspection of the cross-section. These regions encompass areas featuring fine cellular structures, zones exhibiting coarser cellular formations interspersed with slender dendritic boundaries, and heat-affected zones encircling the melt pools. It is noteworthy that the grain size of the cellular structures within the melt pools varies based on their proximity to the melt pool surface. The influence of a heightened cooling rate on the microstructure elucidates the exceptionally fine nature of the cellular-dendritic Al-Si eutectic structure.

Furthermore, the coarse dendritic microstructure observed at the boundaries of the melt pools signifies overlapping regions where the material experienced double melting. In stark contrast, the fine microstructure prevalent in the heat-affected zones is situated between the coarse dendritic boundaries of the melt pools and the fine cellular structures from the preceding

layers. This comprehensive examination provides valuable insights into the intricate microstructural variations induced by the LPBF process, shedding light on the interplay of cooling rates and solidification dynamics in the AlSi10Mg alloy.

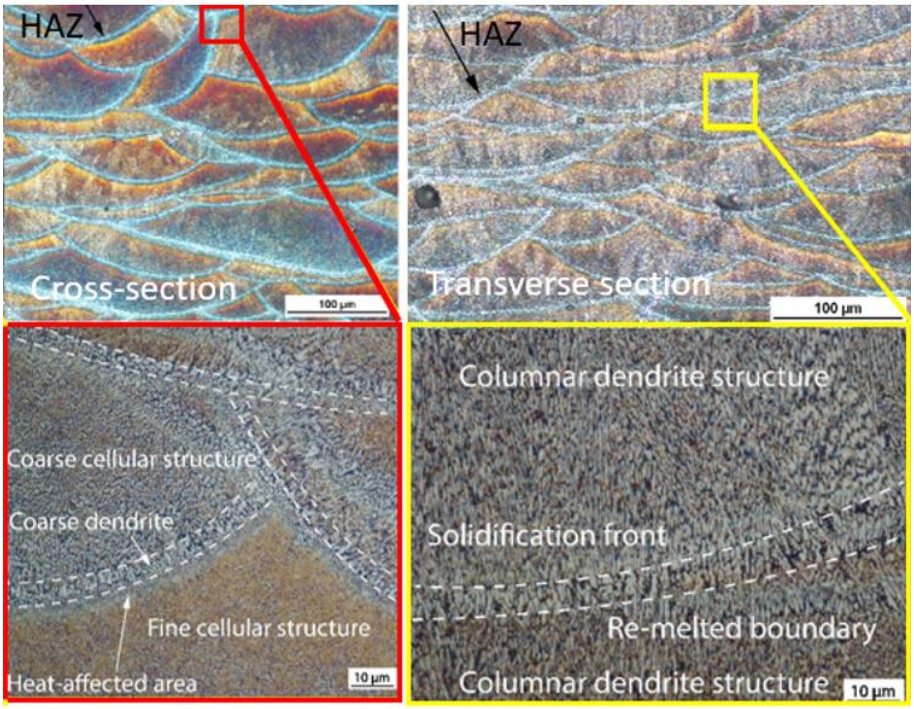

Figure 22 Heterogeneous microstructure on cross- and transverse section of LPBF-manufactutred AlSi10Mg sample

Such heterogeneity as observed both on cross- and transverse section, consisting of both different grain sizes in different regions, but also variable microstructural characteristics across the examined samples suggests the anisotropic mechanical properties.

2.2.2. Mechanical properties and anisotropy

Table 6 lists the calculated velocities of transversal and longitudinal waves travelling through the samples and back to the predetermined measuring points, as well as the calculated mechanical moduli.

Table 6 Velocities of transversal and longitudinal waves tested in different measuring points

	v_l [m/s]	v_t [m/s]	E [MPa]	G [MPa]	B [MPa]	ν
P1	6120.99	3258.66	73843.09	28352.37	62232.45	0.30
P2	6373.31	3241.24	74364.37	28050.05	71052.88	0.33
P3	5383.28	3214.14	67469.18	27582.96	40598.53	0.22
P4	5418.33	3234.37	68331.52	27931.27	41144.97	0.22

Notably, it was observed that varying the position of transducers on the sample surface and the testing direction, the velocity of the longitudinal waves varied significantly. The observed variations in longitudinal wave velocity were pronounced, contrasting with the relatively stable behavior of transverse waves, as illustrated in Figure 23.

Additionally, an examination of the ultrasonic wave signals revealed noteworthy changes in the amplitude of longitudinal waves when altering the position of the ultrasonic transducer, while such amplitude variations were notably less pronounced in transverse wave signals.

It is supposed that the signal amplitude variations, and consequently also velocity variations of longitudinal waves are attributed to the porosity and heterogeneity of the sample. This phenomenon appears to be less prominent in transverse waves, suggesting a lower sensitivity to detecting porosity in the specimens manufactured through LPBF technique. This distinction in sensitivity can be attributed to the orthogonal nature of motion and propagation in transverse waves, compared to the alignment of motion and propagation in longitudinal waves [207, 208].

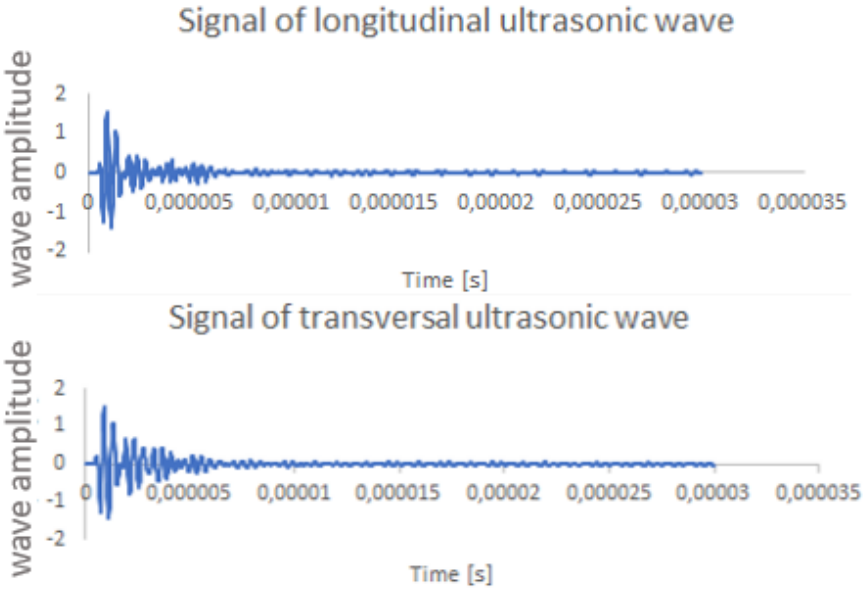

Figure 23 Signal of longitudinal and transversal ultrasonic wave travelling through the specimen

The confirmed relationship of the velocities of the longitudinal waves with the testing direction, and consequently large differences in mechanical moduli calculated for both the testing directions suggest that the mechanical properties of the specimens are significantly anisotropic. It was found that the elastic modulus of the specimen tested in the direction coincident with the building direction was lower than the elastic modulus tested in the direction

perpendicular to the building direction. This phenomenon is commonly reported in the literature [209, 210, 211].

The observed anisotropy in the material is linked to its heterogeneous microstructure. The LPBF manufacturing process, known for inducing epitaxial grain growth, results in a microstructure characterized by grains aligning nearly perpendicularly to the building direction. This unique microstructural alignment significantly influences the mechanical properties of the specimen, particularly enhancing the elastic modulus when tested in a direction perpendicular to the building direction, as documented in reference [212].

Additionally, the elastic modulus of the LPBF-manufactured AlSi10Mg specimen tested in the direction coincident with the building direction was compared to the experimental results originating from the standard destructive tensile test. The stress-strain curve is shown in Figure 24.

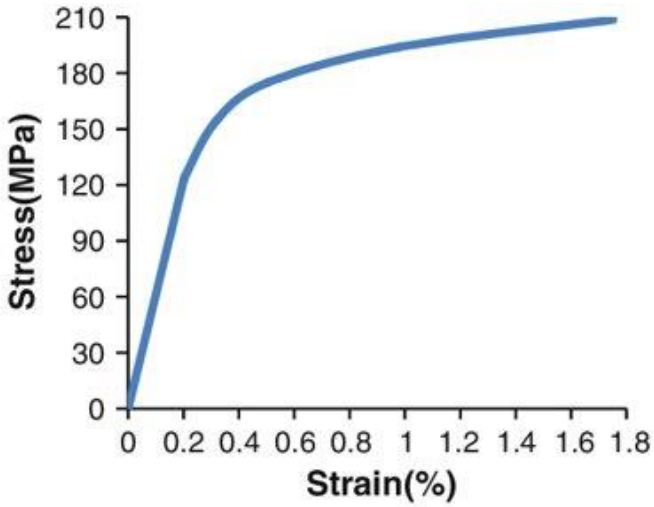

Figure 24 Stress-strain curve of LPBF-manufactured AlSi10Mg specimen

The specimen's ultimate tensile strength was determined to be 207.3 MPa, accompanied by an elongation at break of 1.78%, and an elastic modulus of 67.3 GPa. Importantly, the elastic modulus obtained through the standard tensile test exhibited commendable consistency with values derived from non-destructive ultrasonic testing in the corresponding direction. This convergence underscores the efficacy of ultrasonic non-destructive testing as a valuable tool for discerning the anisotropic mechanical properties inherent in LPBF-manufactured AlSi10Mg specimens.

Conversely, the ultrasonic evaluation of additively manufactured specimens continues to pose challenges due to inherent issues such as resolution limitations, structural noise, and microscopic flaws. The right selection of wave frequency emerges as a key point in achieving both the requisite level of detail and optimal signal readability. This underscores the intricate nature involved in navigating the complexities of ultrasonic assessment for additively manufactured materials.

The anisotropic nature of the specimens was confirmed through microhardness assessments. Noticeable variations in microhardness were observed between the layer core (Figure 25a) and fusion line (Figure 25b). The reduction in microhardness is attributed to the disruption of the fine intercellular network caused by the coarsening of silicon near the boundaries of the melt pool [213, 214]. Additionally, diminished microhardness was identified in overlapping areas exhibiting coarse cellular structures (Figure 25c). Despite the acknowledged impact of defects and porosity on the mechanical properties of LPBF-manufactured components, contemporary literature suggests that grain orientation plays a more significant role in influencing microhardness than porosity does [215].

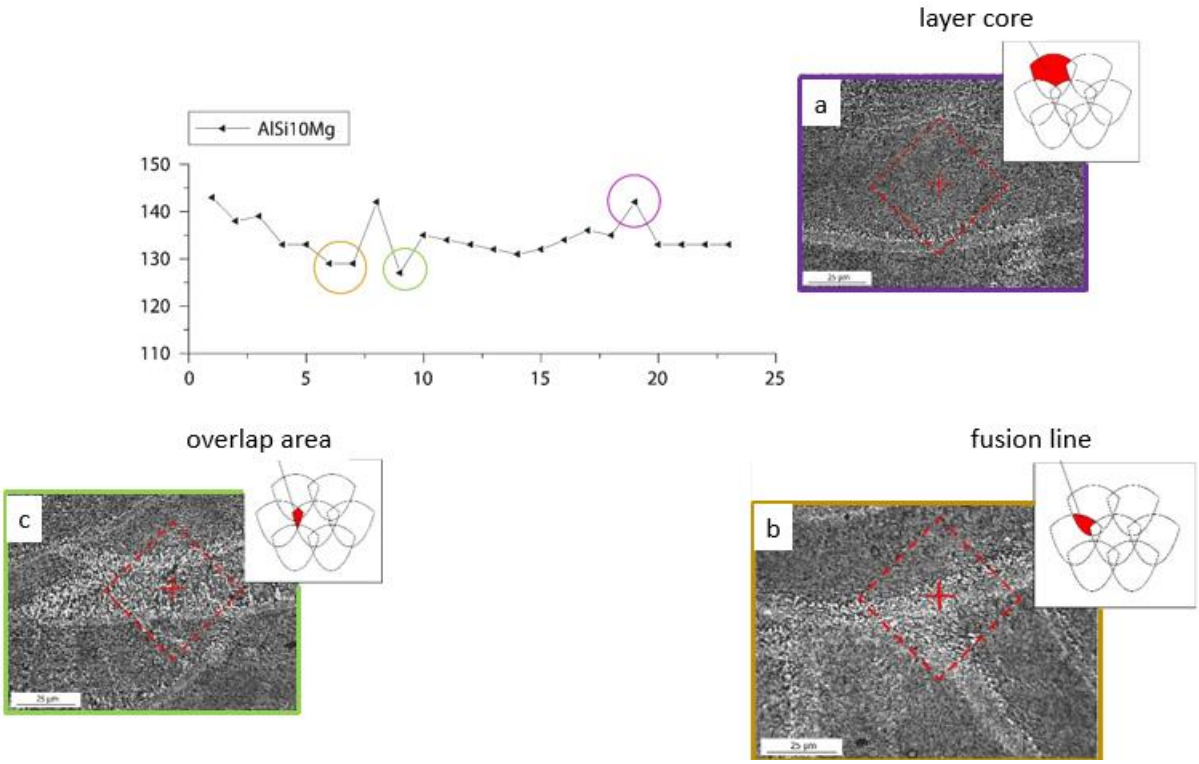

Figure 25 Microhardness tetsting in a.) layer core, b.) fusion line, c.) overlap area

2.2.3. Behaviour of the specimen under thermal load

The examination of the Tdiff signal, depicted against the applied temperature (refer to Figure 26), has unveiled a series of anomalies. It is noteworthy that the incidence of these irregularities in the signal exhibited a discernible correlation with the imposed heating rate.

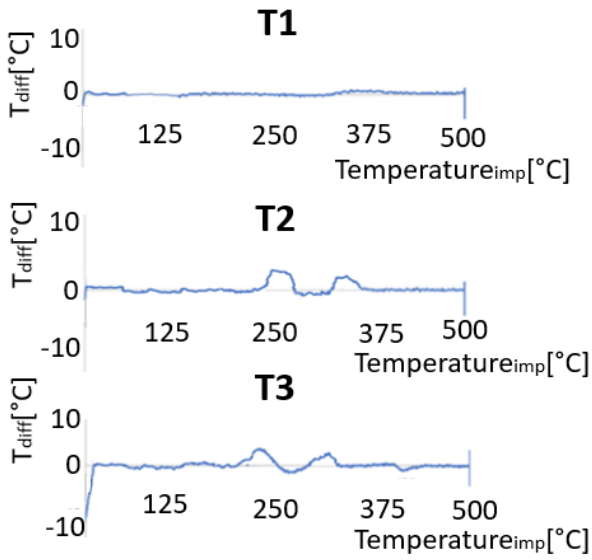

Figure 26 Tdiff signal, plotted over the imposed temperature of T1, T2, and T3 thermal load

The temperature of the specimen under the thermal load T1 mimicked the imposed temperature most accurately, resulting in the least number of irregularities. The irregularities between the temperature of the AlSi10Mg cylinder and the imposed temperature of the T1 load were located mainly until 120 °C, consisting of numerous very short peaks. Another irregularity in the analysed temperature was observed between 320°C and 400°C. The observed peak has a positive direction and prolonged, short, and doltish shape.

Two main irregularities between the real temperature of the AlSi10Mg cylinders and the temperature imposed in the T2 thermal load were observed. The first positive peak was identified between 210 °C and 280 °C, and the second positive peak was identified between 300 and 350 °C. Both peaks demonstrated similar shape characteristics, however, the first identified peak was slightly higher and thicker. It should be noted that the temperature of the cylinder between both identified peaks (280-300 °C) relatively closely followed the imposed temperature and thus no significant irregularities in this temperature range were identified.

Similar irregularities were identified between the temperature of the AlSi10Mg specimen and the imposed temperature of thermal load T3. The first positive peak was identified in a

slightly lower temperature then previously, starting at around 190 °C. It is noteworthy that, unlike in the thermal load T2, the first and second peak are seemingly connected with a shallow negative peak, occurring between 270 and 290 °C. The second positive peak was subsequently identified between 290 and 340 °C. An additional negative peak was identified between 410 and 440 °C.

The initial peak, detected in cylinders subjected to T2 and T3 thermal loads, has been ascribed to microstructural modifications induced by thermal loading, as detailed by Van Cauwenbergh et al. [216]. These alterations are predominantly characterized by the precipitation of silicon (Si) particles from the supersaturated aluminium (Al) cells. The existence of such a microstructure in as-built specimens was corroborated in section 2.2.1. The absence of the first peak during the analysis of the initial thermal load suggests that the applied heating rate did not supply adequate activation energy for this transformation to fully manifest.

Similarly, the second peak, observed across all three thermal loads, is also associated with temperature-induced microstructural changes. Within this temperature range, these changes encompass both diffusional activity and the spheroidization of Si particles [87, 88].

The third peak, evident during the T3 thermal load, can be attributed to the coalescence of primary Si particles. It is noteworthy that this microstructural transformation necessitates a higher activation energy, and consequently, it manifests only at elevated temperatures with a sufficiently low heating rate [88].

The precise positions and configurations of the identified peaks are contingent upon the applied heating rate, which corresponds to the overall thermal energy imparted to the specimen under the respective thermal load. Notably, thermal loads characterized by lower heating rates furnish sufficient thermal energy to activate the microstructural change at an earlier stage, consequently resulting in the occurrence of the peak at a marginally lower temperature [217].

Building upon the established structure–property correlations described in Section 2.2.2, the alterations in microstructure and grain size induced by the thermal load inherently lead to variations in the mechanical properties of the treated component. Consequently, a meticulously optimized thermal load has the potential to induce desired modifications in both the microstructure and mechanical properties of the examined specimen.

Given the identified correlation between irregularities in the material's thermal response to the imposed thermal load and the microstructural changes induced by said load, there arises an opportunity to leverage physical simulations for measuring the thermal response. This, in turn, may facilitate the development of digital twins applicable to tailoring the microstructure of the LPBF-manufactured AlSi10Mg. Through digital twinning, it becomes conceivable to establish an optimal processing window for achieving the desired microstructural configuration through thermal treatment. This innovative approach holds promise as a valuable tool for enhancing the reliability of the LPBF manufacturing method. Nevertheless, it is imperative to acknowledge that further investigations are warranted to comprehensively validate and refine these findings.

3. Mesoscale numerical modelling of LPBF manufacturing process with the AlSi10Mg alloy

In contemporary times, numerical modelling withstands a pivotal role in the commercialization of additive manufacturing technologies. Its primary contributions include enhancing reliability, minimizing material and financial wastage, and elevating the overall product quality. Numerical modelling and simulation provide invaluable comprehension of the synergistic impacts of strain, strain rate, and temperature—a critical aspect for discerning the crashworthiness of additive manufacturing components. Despite the ongoing and intensive research efforts in this domain, there is still a pressing need, particularly within the industrial realm for the development of robust and potent numerical models.

Furthermore, the development of sufficiently accurate and efficient numerical models in the context of LPBF fabrication serves as a crucial prerequisite for enhancing the efficacy of numerical modelling in the post-processing treatment of LPBF-manufactured components—a topic of burgeoning significance in the industrial landscape. This chapter therefore aims to introduce a novel numerical model designed to predict melt pool dynamics and lack-of-fusion occurrences in AlSi10Mg specimens during LPBF manufacturing on the mesoscale.

The original numerical model encapsulates the phase transition from powder to liquid, along with subsequent solidification, providing a comprehensive depiction of the intricate dynamics within the mushy zones. It accounts for factors such as the interaction of the powder bed with the Gaussian volumetric moving heat source, non-isothermal flow of melted metal, thermal expansion, and the Marangoni effect. The validation of the original numerical model is assessed through a comparative analysis of melt pool dimensions simulated under various sets of process parameters with corresponding experimental results. These experiments were conducted under the same process conditions, either within our experimental campaign or as reported in the literature. The chapter underscores the significance of the proposed numerical model in advancing the understanding and control of LPBF processes, contributing to the broader discourse on additive manufacturing in industrial applications.

3.1. Experimental set-up

3.1.1. Manufacturing of the samples

The present investigation adhered to a full factorial design within the framework of the chosen design of experiment (DOE). The implemented experimental plan meticulously

examined the formation of melt pools and the potential occurrence of lack-of-fusion defects in a set of 9 specimens. Each specimen was produced with a distinct combination of laser power and scanning speed, recognized as pivotal process parameters in the Laser Powder Bed Fusion (LPBF) manufacturing process. It is noteworthy that all other process parameters were held constant across the manufacturing of all specimens, as detailed in Table 7.

Table 7 The values of the constant process parameters

Constant process parameters		
Layer thickness [µm]	**Hatch spacing [µm]**	**Laser beam diameter [µm]**
30	80	100

The implemented Design of Experiments (DOE) comprised two distinct factors, each containing three different levels. It is important to note that this experimental configuration yielded a total of nine experimental units, as detailed in Table 8. However, it is necessary to highlight that, during the course of the experimental campaign, only four specimens were both manufactured and tested. The experimental results for the remaining specimens were extrapolated from the available literature. The specific combinations of processing parameters employed in the manufacturing of specimens within our experimental campaign are emphasized in bold in Table 8. Additionally, Table 8 provides a comprehensive listing of the values of energy density (ED), calculated for each unique combination of processing parameters, as delineated in Equation (15).

$$ED = \frac{P}{vhd} \quad (15)$$

where P denotes the laser power, v is the scanning speed, h is the hatch spacing and d is the layer thickness.

Table 8 LPBF process parameters designed according to the full factorial plan

Sample	**Laser power** [W]	**Scanning speed** [mm/s]	**Energy density** [J/mm^3]
S1	**100**	**400**	**104.17**
S2	100	600	69.44
S3	**100**	**1000**	**41.67**
S4	200	400	208.33
S5	200	600	138.89

S6	200	1000	83.33
S7	**275**	**400**	**286.46**
S8	275	600	190.97
S9	**275**	**1000**	**114.58**

During the conducted experimental campaign, four specimens of AlSi10Mg alloy measuring 0.5x1x0.21 mm were fabricated utilizing the EOSINTM270 manufacturing system, a product of EOS (Germany). The supplied powder, whose chemical composition is detailed in Table 3, was sourced from EOS. The fabrication process adhered to a zigzag scanning strategy, as illustrated in Figure 27, for all specimens.

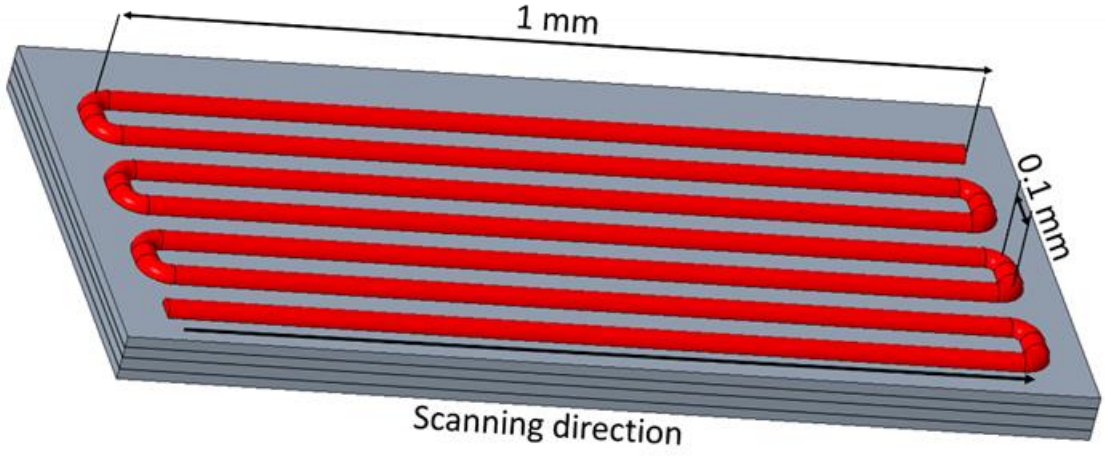

Figure 27 Scanning direction and laser beam path applied to manufacture the specimens within the own experimental campaign

3.1.2. Determination of the melt pool dimensions and presence of lack-of-fusions

The melt pools were identified as the zones that underwent fusion and resolidification. Their dimensions were determined by measuring the maximum length in the XY plane for length and the highest z-dimension for depth. The same methodology was employed for the determination of Length of Fusion (LOF) dimensions.

Measurements within our experimental campaign were conducted using optical microscopy images and pixel counts. To facilitate these measurements, specimens were carefully cut and subjected to etching using Keller's reagent solution. The microstructure of the specimens was examined in both transverse and cross-sectional views.

The micrograph method, as outlined by Propoppatum et al. [218], was employed to determine the mean LOF and melt pool dimensions, along with the final volume of LOFs. The volume of LOFs was computed according to Eq. 16:

$$V_{lack-of-fusions}\ [\%] = \frac{\sum V_{LOF\ defects}}{V_{total}}.100 \quad (16)$$

3.2. Numerical model

A comprehensive coupled mechanical-thermo-fluid dynamical model was developed to simulate the manufacturing process of nine specimens, each characterized by distinct process parameters (refer to Table 8 for details). The numerical model intricately captured the coexistence of various phenomena, encompassing the interaction between the powder and the laser heat source, the dynamics of phase change interfaces, non-isothermal flow, thermal expansion, and the influential Marangoni effect [219].

In the simulation, non-melted layers of AlSi10Mg alloy powder were represented as homogeneous porous media, with a specified packing density of 0.7 [220]. The deposition of new layers was delineated through the utilization of a birth-and-death technique, allowing for a sufficiently accurate representation of the additive manufacturing process.

The powder material properties are shown in Figure 28.

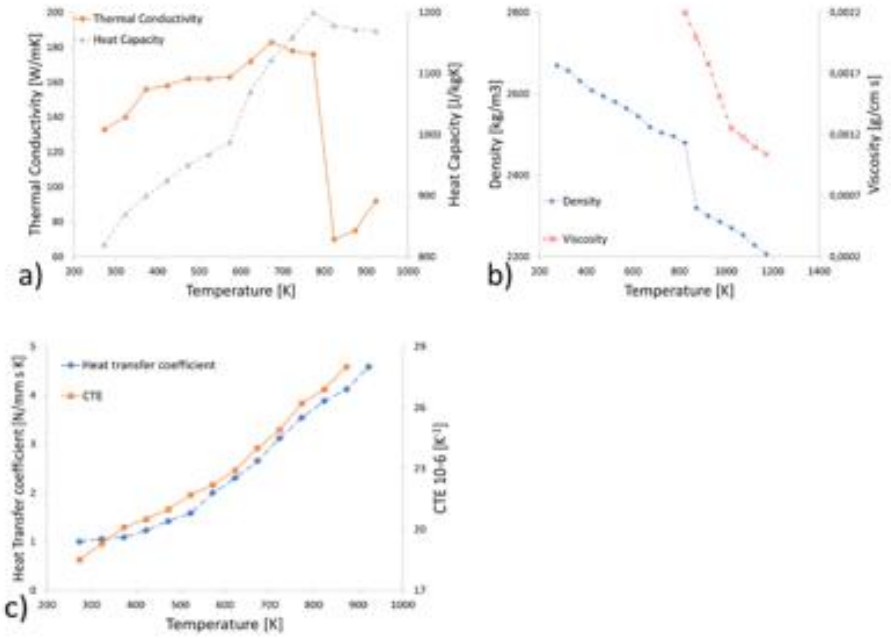

Figure 28 Material properties: Thermal conductivity [84] and heat capacity [96] (a); Density and vis-cosity [94] (b); Heat transfer coefficient [91] and CTE [91] (c)

Complex nature of presented model was described by CFD model based on mass, momentum, and energy conservation equations (17, 18, 19) [221].

$$\nabla . \vec{v} = 0 \qquad (17)$$

$$\frac{\partial \vec{v}}{\partial t} + (\nabla . \vec{v})\vec{v} = -\frac{1}{\rho}\nabla P + \mu \nabla^2 \vec{v} + \vec{g} + F_b \qquad (18)$$

$$\frac{\partial h}{\partial t} + (\nabla . \vec{v})h = -\frac{1}{\rho}(\nabla . k \nabla T) + Q \qquad (19)$$

Where v is the molten material velocity, P is the pressure, ρ is the density, μ is viscosity, g is gravity, F_b is the body force, h is enthalpy, t is time, k is thermal conductivity, T is temperature and Q is the input energy from the heat source.

Heat source was defined as Gaussian heat source model (20, 21) [222]:

$$Q(x,y) = I exp\left[-\left(\frac{2(r(t))^2}{r_q}\right)\right] \qquad (20)$$

$$I = \frac{2AP}{\pi h r_q} \qquad (21)$$

Where Q is the heat source, I is the intensity, r describes the position and r_q is the laser beam radius. A denotes the absorptivity, P denotes the laser power, h is the height of the heat source.

The phase change from solid to liquid state was stimulated through latent heat of fusion. Enthalpy was defined as follows: (22) [223, 224]

$$h = \int C_p dT + l_f \quad (22)$$

where Cp is thermal capacity, l_f is latent heat of fusion.

Density, heat capacity and thermal conductivity in the mushy zone were calculated as follows (23, 24, 25):

$$\rho = \rho_s \theta_s + \rho_l \theta_l \quad (23)$$

$$C_p = \frac{1}{\rho}\left(C_{ps}\rho_s\theta_s + C_{pl}\rho_s\theta_s\right) + l_f \frac{\partial a_m}{\partial T} \quad (24)$$

$$k = k_s \theta_s + k_l \theta_l \quad (25)$$

Where θ_s and θ_l are the phase fraction of solid and liquid phase and a_m is the mass fraction of mushy state.

Further, the a_m is defined by the equation (26) [224]:

$$a_m = \frac{1}{2}\frac{\rho_l\theta_l - \rho_s\theta_s}{\rho_s\theta_s + \rho_l\theta_l} \quad (26)$$

The body mass force was applied to dampen the velocity in the mushy zone. The Kozeny-Carman equation was integrated [222].

Marangoni effect was depicted as the coupling feature of heat transfer and laminar flow.

The material was described as elasto-plastic, with the hardening function described by Johnson-Cook model. The temperature-induced material softening was considered.

The thermal expansion was described as coupling feature of solid mechanics model with the heat transfer.

In the post-build state, the lack-of-fusions were identified as areas where the temperature did not exceed the melting point. Consequently, the level of lack-of-fusion defects was calculated (16). The melting pools were identified according to the heat distribution in consolidated layers.

3.3. Validation of the simulated results and statistical analysis

The validation of our proposed numerical model underwent validation involving a comparison between experimental and simulated results, accompanied by the subsequent calculation of the relative error inherent in the simulated outcomes. Furthermore, the data was subjected to the statistical analysis to determine the effects of energy density, laser power, and scanning speed on the tested dimensions of the melt pools and lack-of-fusions. Employing analysis of variance (ANOVA), statistical significance of these input parameters in relation to the output parameters was determined. This investigative process was complemented by the application of a full-factorial Design of Experiments (DOE), from which regression equations were derived. The execution of these statistical analyses was conducted using the Minitab software platform.

3.4. Results and discussion

3.4.1. Melt pool dimensions and lack-of-fusion volume

Table 9 shows the simulated and experimental values of mean melt pool lengths and LOFs volumes. The simulated and experimental data were in good agreement and the proposed numerical model can be therefore considered validated.

Table 9 Simulated and experimental values of melt pool length and LOFs volume

Sample	**Melt pool length** [μm]			**Volume of lack-of-fusion defects** [%]		
	Simulated	**Experimental**	**Relative error** [%]	**Simulated**	**Experimental**	**Relative error** [%]
S1	159	151	5.30	2.96	3.12	5.13
S2	136	128 [15]	6.25	3.18	3.68 [20]	8.15
S3	128	136 [16]	5.88	4.58	4.36 [20]	5.05
S4	254	278 [14]	8.63	1.54	1.47 [18]	4.76
S5	148	143 15]	3.50	2.14	1.98 [20]	8.08
S6	144	152 [16]	5.26	2.78	2.64 [17]	5.30

S7	281	296	5.06	0.39	0.41	4.87
S8	234	246 [14]	4.88	0.71	0.67 [19]	5.97
S9	152	144	5.56	1.25	1.225	2.04

Figure 29 additionally demonstrates the comparison of simulated and experimental melt pool lengths, depicted in their relationship with the energy density.

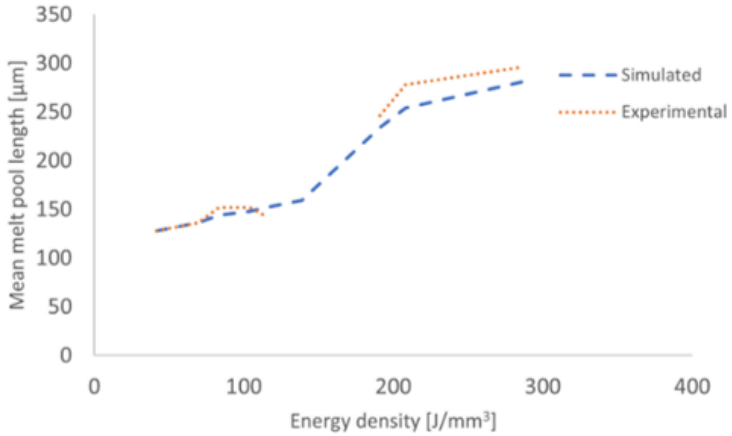

Figure 29 Comparison of simulated and experimentally assessed values of mean melt pool lengths, depicted in their relationship to the energy density

The statistical significance of the quasi-linear relationship between the energy density and mean melt pool length was confirmed by ANOVA (R^2 of 91.29%, P-value of 0.00). Notably, short melt pools were observed in those specimens manufactured with lower energy density (S2, S3). When the energy density was over 200 J/mm^3, the melt pools were considerably longer (Figure 30). Increase of melt pool length caused by increased energy density was confirmed by literature [224,225,226].

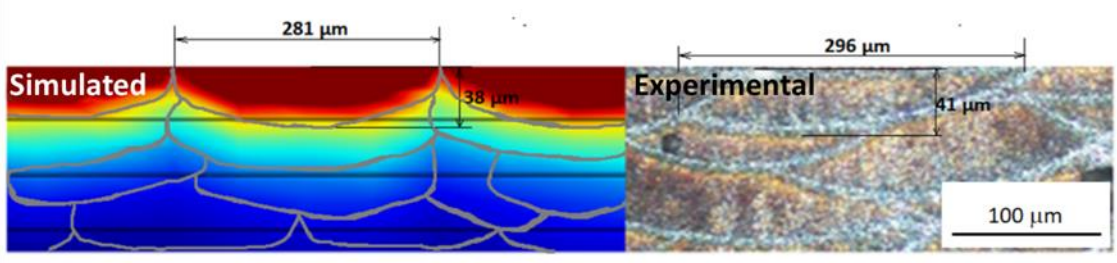

Figure 30 Simulated and experimental melt pools with high length in specimen S7, manufactured with high energy density

Moreover, ANOVA confirmed statistically significant effects of both laser power and scanning speed (Table 10).

Table 20 Results of ANOVA determining the significance of the effects of the laser power and scanning speed on the melt pool length and the regression equation

	R^2 [%]	P-value		Regression equation
		P	v	
Melt pool length	93.82	0.03	0.02	$245 + 0.831\ P - 0.468\ v + 0.00073\ P^2 + 0.000358\ v^2 - 0.000960\ P.v$

Main effect plots (Figure 31) have revealed relatively linear relationship between laser power and melt pool lengths, where the increase of laser power results in gradual increase of the melt pool lengths. In contrast, indirect proportion between the scanning speed and melt pool length has been identified, however the increase of the scanning speed causes the decrease of the melt pool length just until the value of approximately 800 mm/s. Further increase of the scanning speed to 1000 mm/s do not cause the significant change in melt pool length.

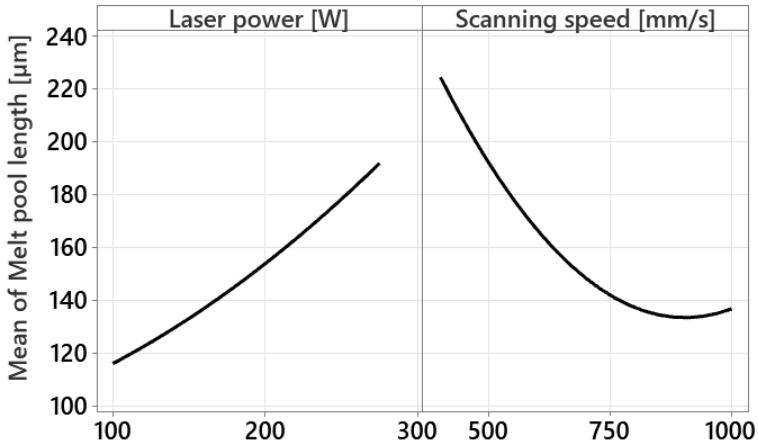

Figure 31 Main effect plots of laser power and scanning speed on the mean melt pool length

Similarly, as in Figure 29, quasi-linear relationship between energy density and LOFs volume was observed. Figure 32, further comparing the simulated and experimental LOFs volumes, depicted in their relationship to the energy density, demonstrates the success of the presented model as the simulated and experimental values were in good agreement.

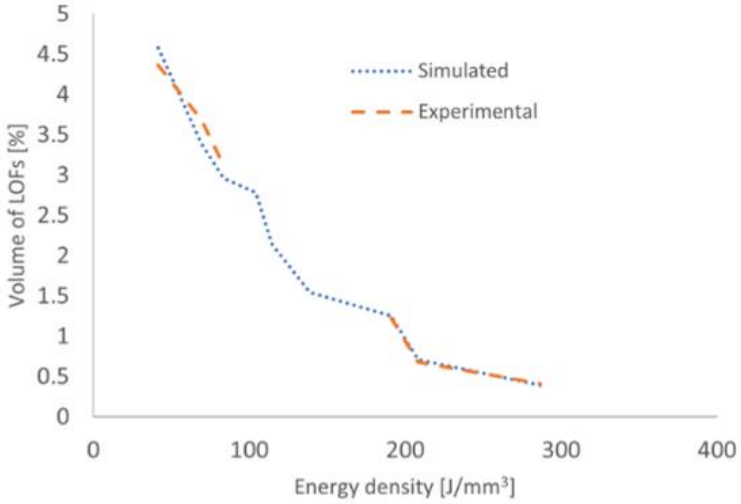

Figure 32 Comparison of simulated and experimentally assessed values of mean LOF volumes, depicted in their relationship to the energy density

Notably, the indirect proportion between the energy density has been proven to be statistically significant by ANOVA (R^2 of 75.68%, P-value of 0.002). The presented results are suggesting that higher energy density resulted in lower volume of LOFs, and vice versa. Figure 33 demonstrates the comparison of simulated and experimentally assessed microstructure in specimen S7 in transversal view. Even though the sampled specimen was manufactured with high energy density, few lack-of-fusions were still observed in examined interlayers.

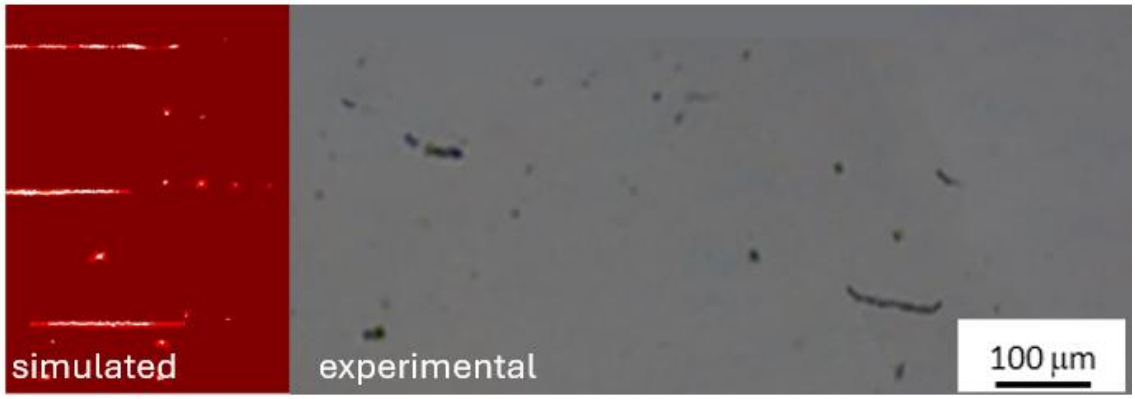

Figure 33 Comparison of simulated and experimentally assessed microstructure in specimen S7

Similarly, as for the melt pool lengths, the ANOVA has determined that the effects of laser power and scanning speed on the volume of LOFs is statistically significant. The results of ANOVA, together with the regression equation, are listed in Table 11.

Table 11 Results of ANOVA determining the significance of the effects of the laser power and scanning speed on the LOF volume and the regression equation

	R^2 [%]	**P-value**	**Regression equation**

		P	v	
LOF volume	99.40	0.000	0.003	2.310 - 0.00192 P + 0.00301 v - 0.000023 P^2 - 0.000008 P.v

Main effect plots (Figure 34) have revealed linear-like relationships between both examined input parameters (laser power and scanning speed) and LOF volumes. While the indirect proportion between the laser power and mean LOF volumes was identified, the relationship between scanning speed and LOF volume was characterized by the direct proportion.

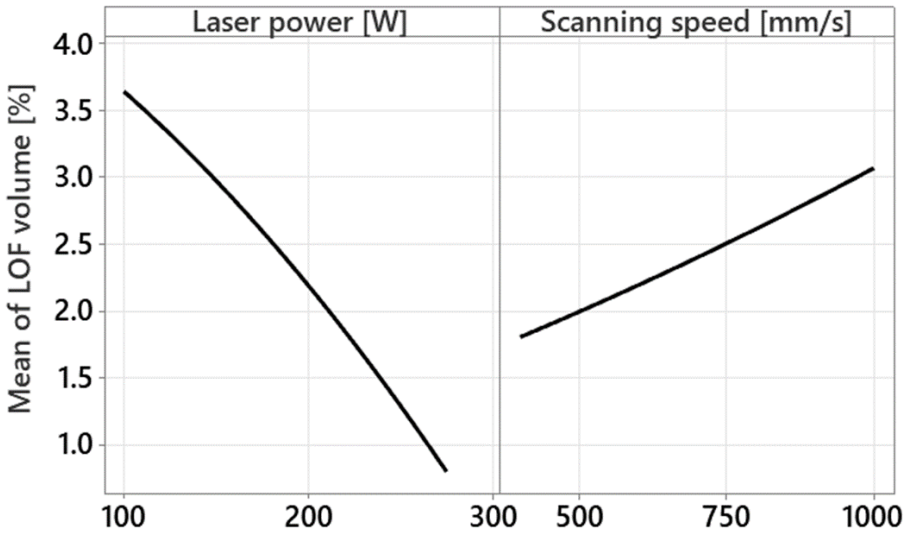

Figure 34Main effect plots of laser power and scanning speed on the mean LOF volume

3.4.2. Lack-of-fusion dimensions

Moreover, the study examined the simulated lack-of-fusion dimensions, and how they are affected by the energy density, laser power, and scanning speed. Figure 35 demonstrates the relationship between mean lack-of-fusions length and depth with the energy density.

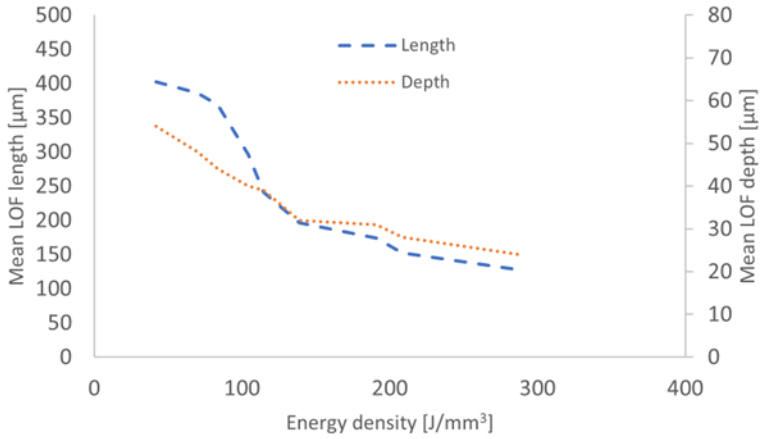

Figure 35 Mean length and depth of lack-of-fusions vs. energy density

The indirect proportion and relatively linear relationship between the energy and mean LOF depth was observed (R^2 of 90.34%, P-value of 0.018), while the curve describing the effects of energy density on the mean LOF length was seemingly much less regular (R^2 of 68.32%, P-value of 0.06).

Moreover, both mean lack-of-fusion depth and length were majorly impacted by the laser power, while the scanning speed impact was slightly less significant (depth) or statistically unsignificant (length), as evidenced by ANOVA (Table 12).

Table 12 Results of ANOVA determining the significance of the effects of the laser power and scanning speed on the LOF dimensions, and the extracted regression equations

	R^2 [%]	**P-value**		**Regression equation**
		P	**v**	
LOF depth	98.57	0.001	0.015	5.784 - 0.00294 P + 0.00301 v - 0.000057 P^2 +0.00031v^2- 0.000003 P.v
LOF length	63.83	0.014	0.126	186.274 + 0.378 P - 0.217 v + 0.0041 P^2 + 0.000184 v^2 - 0.00110 P.v

Described behaviour was caused by low laser absorption of the AlSi10Mg alloy [227]. By analysing the mean effects plots (Figure 36) it was determined that the mean depth of LOFs was directly proportionate to scanning speed and indirectly proportionate to laser power, while the mean length of LOFs was indirectly proportionate to laser power.

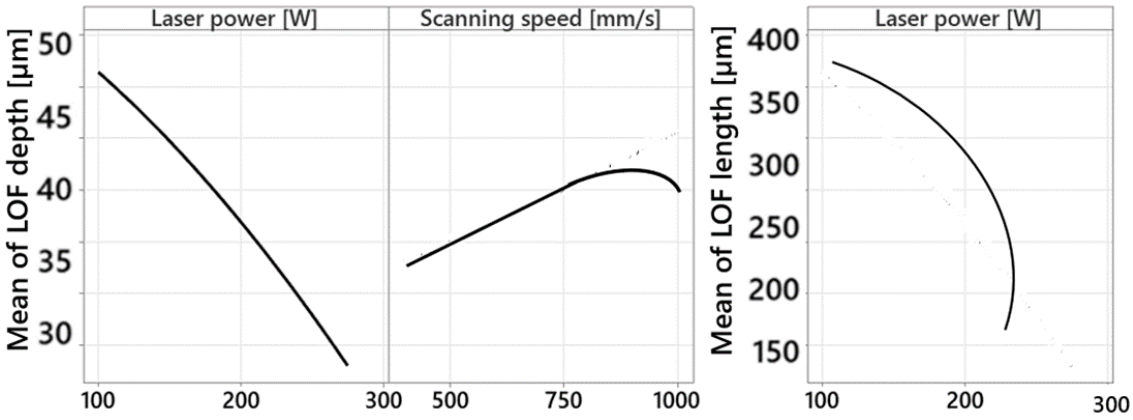

Figure 36 Main effect plots of laser power and scanning speed on the mean LOF depth and main effects plot of laser power and mean LOF length

High scanning speed in combination with low laser power resulted in shorter and shallower LOFs (specimens S7 and S8). On the other hand, the combination low laser power and high scanning speed resulted in longer and deeper lack-of-fusions, as well as higher volume of lack-of-fusions within the specimen (specimens S2, S3).

Significant differences in both examined LOF dimensions in specimens S1 and S9 were observed, even though the energy density was similar. However, in S9, higher laser power was applied, which allowed more efficient melting. Low laser power was thus balanced by the low scanning speed just partially. Similarly, in specimens S4 and S8, differences in geometry and volume of lack-of-fusions were caused by different process parameters, even though the applied energy density was similar. Fiedler et al. [227] suggested that this effect is observable in specimens manufactured from AlSi10Mg alloy, as the laser absorptivity is low.

Notably, low scanning speed resulted in more sufficient melting, better connecting of subsequent layer and neighbouring melt tracks and shorter lack-of-fusion pores [228, 229].

3.4.3. Temperature distribution in manufactured layers

Additionally, the simulated temperature distribution in fused layers was examined and analysed. It was determined that temperature distribution was highly influenced by the energy density (Figure 37). It was observed that the increase of the energy density generally resulted in the significant increase of the temperature of the scanned layers with more uniform temperature distribution. The observed phenomenon is in accordance with the results in literature [230, 231].

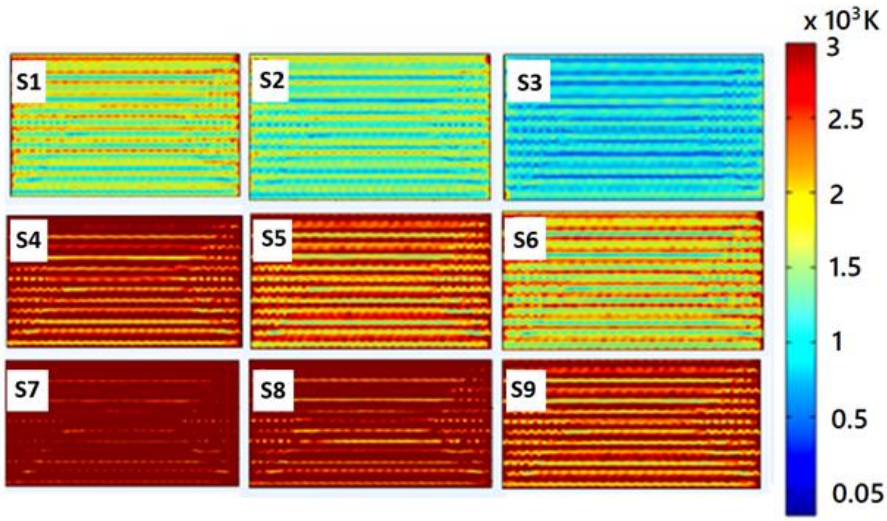

Figure 37 Comparison of temperature distribution in the top layer after the build in specimens manufactured with different process parameters

The investigation revealed that achieving a high energy density, through the combination of a low scanning speed and elevated laser power (e.g., specimen S7), led to the elevation of temperature beyond the melting point, resulting in significant evaporation. Notably, the presented numerical model did not account for mass losses due to evaporation, thereby anticipating a higher overall porosity, even with a calculated low volume of lack-of-fusions [229]. This observation aligns with findings from [232], which identified an energy density exceeding 52.63 J.mm3 as a critical threshold for inducing overheating and excessive evaporation in AlSi10Mg.

Despite the acknowledged limitations in the proposed numerical model, it demonstrates sufficient predictive accuracy and holds scientific and industrial significance. As highlighted in Section 1.4.2, forecasting the formation of melt pools and lack-of-fusions currently stands out as a highly effective tool for comprehensive process control, enhancing the reliability of the LPBF manufacturing process. Furthermore, these sufficiently accurate and efficient numerical models for LPBF fabrication serve as essential prerequisites, augmenting the efficacy of numerical modelling for post-processing treatments applied to components manufactured through LPBF. This letter represents a rapidly evolving area of considerable industrial importance.

4. Investigation of the effects of the building position during the LPBF on the geometrical dimensions, tolerances, and surface characteristics

The precision and overall quality of objects produced through Laser Powder Bed Fusion (LPBF) technology are commonly enhanced through process optimization. However, the intricate relationship between process, structure, and properties poses a substantial challenge to achieving efficiency. While much research focuses on optimizing processes by manipulating energy density, insufficient attention has been given to precise control and modifications of the printing environment and positioning of specimens on the printing platform when constructing multiple objects simultaneously.

To address this research gap, our study aims to investigate the impact of the position of LPBF-manufactured blocks on the building plate on their geometric dimensions, tolerances (GD&T), and surface roughness. Nine cubical specimens were fabricated from AlSi10Mg powder via LPBF using optimized process parameters, consistent across all samples. Subsequent GD&T and surface roughness analyses were conducted using Coordinate Measuring Machine (CMM) and perthometer. Numerical simulations of block fabrication and GD&T analysis were performed to further explain the distortion mechanisms, with validation through experimental results.

Statistical significance of position on GD&T was demonstrated for dimensional deviations, bottom face planarity, parallelism of top and bottom faces, and perpendicularity of top and x-oriented faces. Regression equations were assessed, revealing the lowest dimensional errors in the block positioned centrally on the building plate due to favorable thermal fields created by surrounding blocks. Similar correlations between thermal fields and errors in planarity, parallelism, and perpendicularity were observed, resulting in the least distorted cube located in the middle of the base plate.

These findings bear substantial industrial significance, particularly in applications requiring high precision in fields such as healthcare, implantology, and aerospace. The results emphasize that meticulous control and planning of specimen distribution on the building platform or compensating CAD models for position-induced distortions can significantly enhance the efficacy and reliability of LPBF manufacturing technology. Furthermore, comprehensive knowledge of distortions induced by the LPBF process becomes crucial when specimens

undergo post-processing treatments that may introduce additional displacements. In such cases, careful consideration and prediction of the combined effects of manufacturing process-induced and treatment-induced displacements are essential to ensure that components meet pre-defined requirements for dimensional accuracy or to evaluate if distortions disqualify components from their intended applications.

4.1. Materials and methods

4.1.1. Sample fabrication

Nine cubical 35x35x35 mm specimens were manufactured by means of L-PBF. Gas-atomized AlSi10Mg powder, supplied by EOS Gmbh (EOS, Germany) was utilized in the study. The particle size distribution was 25-70 µm, and the chemical composition is shown in Table 3.

The strip exposure with the 67° angle between each successive layer was adopted as the scanning strategy for all manufactured blocks (Figure 38).

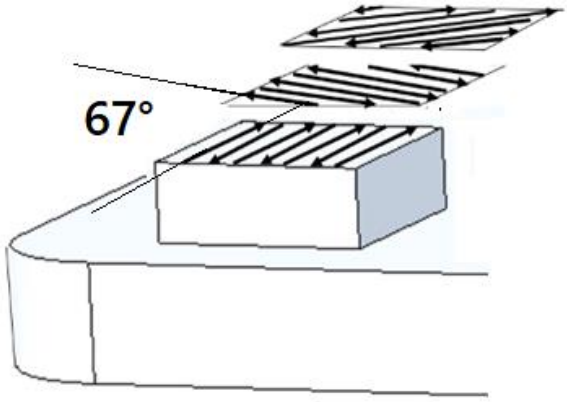

Figure 38. Scanning strategy

AlSi10Mg blocks were manufactured utilizing an EOSINT M270 machine equipped with a 200 W fiber laser, featuring a laser spot diameter of 90 µm at the focal plane. The laser beam was precisely focused on the horizontal plane of the specimens-in-build. To mitigate oxidation during the manufacturing process, a vacuum argon medium was introduced into the building chamber, reducing oxygen content to less than 0.1%. Additionally, pre-heating the building plate to 200 °C was implemented to suppress the residual stress formation. Process parameters were chosen based on the recommendations provided by the manufacturer of the specific material, as outlined in Table 2. Figure 39 visually depicts the as-built blocks affixed to the building plate.

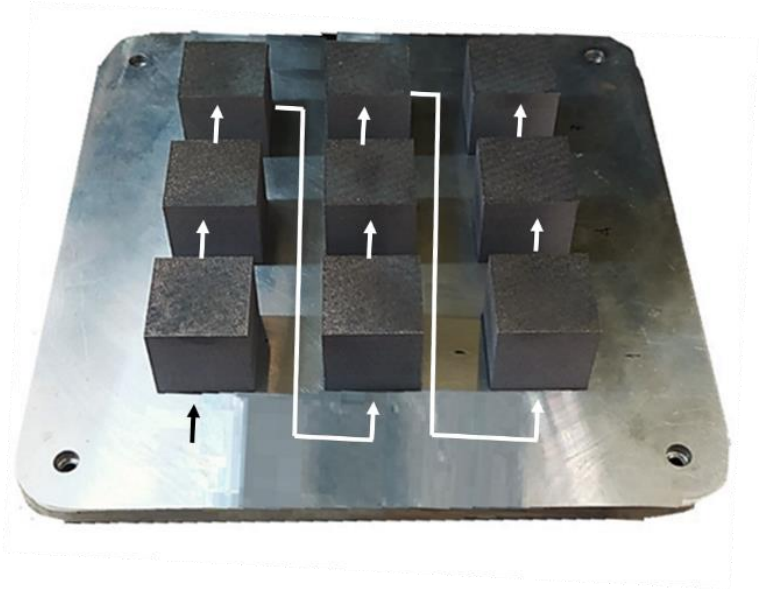

Figure 39. As-built blocks attached to the building plate, the black/white arrows display the building sequence.

During the construction process, the blocks were systematically distributed across the building plate to ensure uniformity. Each block was placed directly on the plate without the utilization of any additional supports. To facilitate seamless data analysis and unambiguous sample identification, a systematic labeling system was implemented. The blocks were assigned numerical labels, wherein the first digit denoted the position along the x-axis (1, 2, 3), and the second digit represented the position along the y-axis (1, 2, 3). The blocks were assembled in a predetermined sequence, specifically in the order of 1.1, 1.2, 1.3, 2.1, 2.2, 2.3, 3.1, 3.2, and 3.3. Refer to Figure 40 for a visual representation illustrating the distribution of samples, their corresponding labels, and the orientation of the plate during the construction process.

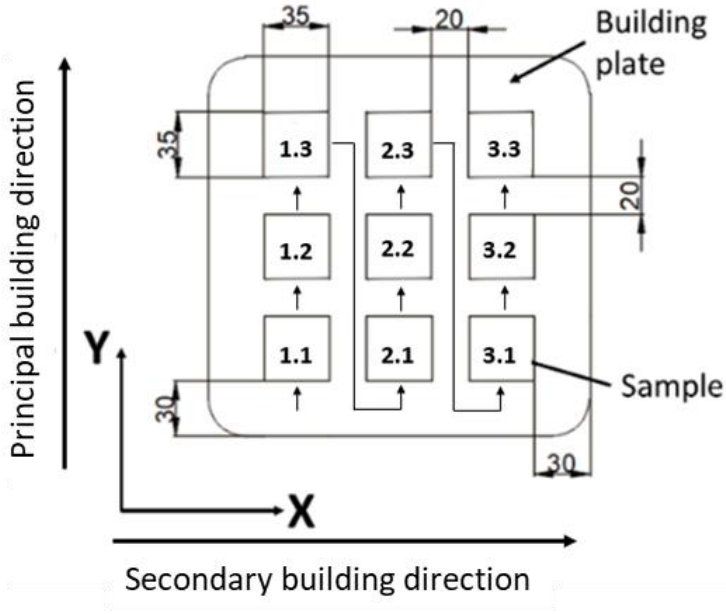

Figure 40. Distribution of labelled cubical samples across the building plate

Blocks were not subjected to post-process treatment as the dimensional accuracy and surface roughness in the as-build state were studied.

4.1.2. Analysis of geometrical dimensions and tolerances of fabricated blocks

The manufactured blocks underwent precise measurements utilizing a tactile coordinate measuring machine (CMM). This comprehensive analysis included an assessment of the planarity of every face of each block, determination of the distances between all parallel faces of the cubes, and evaluation of the parallelism and perpendicularity among the selected faces of the cube. For visual clarity, Figure 41 illustrates the parameters under examination on the appraised faces of the cubical specimens, along with their corresponding labeling.

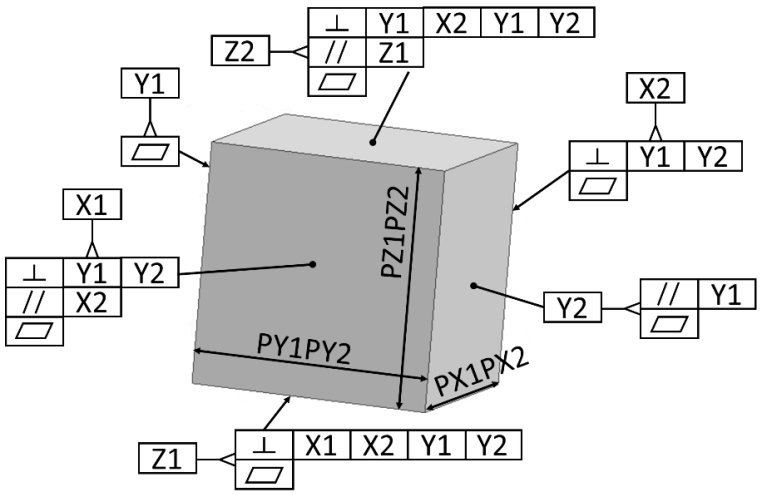

Figure 41. Schematic representation of examined parameters and assessed faces.

The geometric dimensions and tolerances of the specimens under consideration were assessed using the Altera LK coordinate measuring machine. This machine possesses the inherent capability to measure specimens with dimensions of up to 1500x1000x800 millimeters, providing a volumetric accuracy of 1.1 µm+L/375 and a repeatability of 0.7 µm. The applied measuring system achieves a maximum speed of 720 mm/s, coupled with a maximal acceleration of 1,900 mm/s². Figure 42 visually presents the process of measurement.

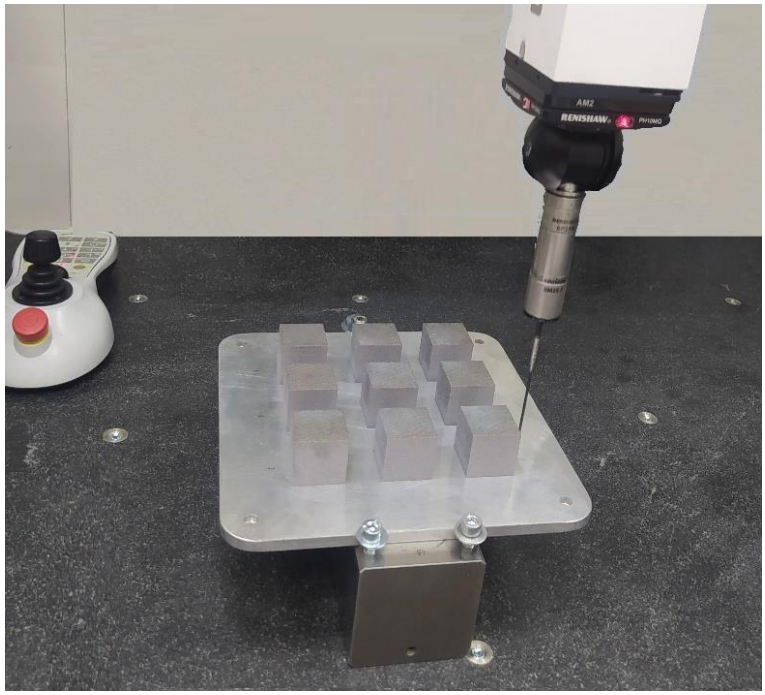

Figure 42. Geometrical dimensions and tolerances assessment

The x-, y-, and z-dimensions of the examined cubes were evaluated according to ISO 15530-3 standard, adopting 17 measuring points at each assessed face, with the distribution as

shown in Figure 43. The measuring procedure included the evaluation of planarity, flatness, and parallelism errors as they all affect the examined dimensions.

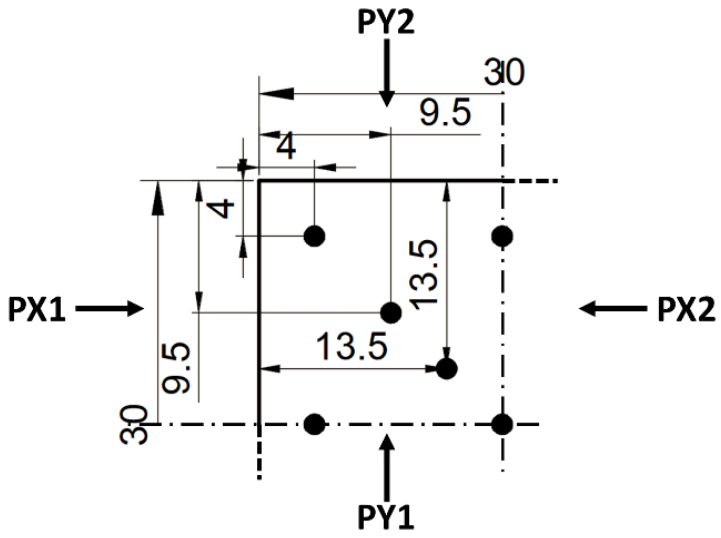

Figure 43. Measuring plan.

The total uncertainty affecting the sides of each cube is obtained from the combination in quadrature of the measuring uncertainty and the relative systematic error, according to the formula (eq. 27):

$$U = \pm\sqrt{u_m^2 + e^2} \quad (27)$$

Where U stands for total uncertainty, u_m is the measuring uncertainty and e denotes the systematic error. The present study applies Ux, Uy, and Uz abbreviations denoting the total uncertainties for x-, y-, and z-dimensions.

4.1.3. Analysis of surface quality of fabricated pieces

Surface quality was assessed via surface roughness measurements by MarSurf XCR 20 (Mahr). The employed perthometer had 2.5 µs sensitivity and measured the surface roughness in ±250 µm. Measurements at intervals of 4 mm, containing 11200 measuring points were conducted on free surfaces of cubical specimens in the same direction. The processing setup is shown in Figure 44.

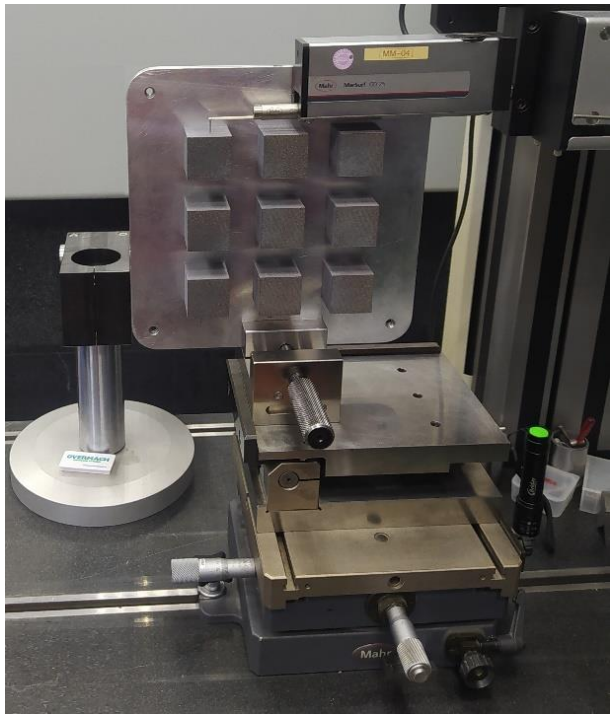

Figure 44. Assessment of surface quality

Four types of surface roughness were evaluated: Ra (roughness profile arithmetic average), Rq (root mean square average of profile height deviations from the mean line), Rz (average of maximum peak to valley heights of the profile in the sampling lengths, over the full assessed length), and Rt (total height of profile over the evaluated length). They were calculated as follows (Eq. 28, 29, 30, 31) [233, 234, 235]:

$$R_a = \frac{1}{l_m}\int_0^{l_m}|z(x)|dx \qquad (28)$$

$$R_q = \sqrt{\frac{1}{l_m}\int_0^{l_m} z^2\, x\, dx} \qquad (29)$$

$$R_z = R_p + R_v \qquad (30)$$

$$R_t = \max\left(R_{pi}\right) + \max\left(R_{vi}\right) \qquad (31)$$

Where lm denotes the measured length, z represents the z-coordinates of assessed peaks, Rp denotes the maximal height of all assed peaks, Rv denotes the maximal depth of all assed peaks, max (Rpi) stands for a sum of heights of 5 highest peaks and max (Rvi) represents the sum of depths of 5 most profound peaks. Term max represents the maximum as the maximal values of both height and depth of the profile are evaluated, as it was explained before.

Given that the blocks remained affixed to the building plate, only certain faces were available to roughness assessment. Consequently, for spatial considerations, exclusive

evaluation was performed solely on the Z2 face across all blocks. Nevertheless, owing to the greater accessibility afforded by the positioning of outer faces, supplementary evaluations were conducted on additional faces within selected blocks. Figure 45 illustrates all evaluated measurements and their respective positions, denoted by arrowed lines. Specifically, selected faces, including the top faces of all scrutinized cubes and the X1 face of cube 1.2, underwent additional assessments in a perpendicular direction.

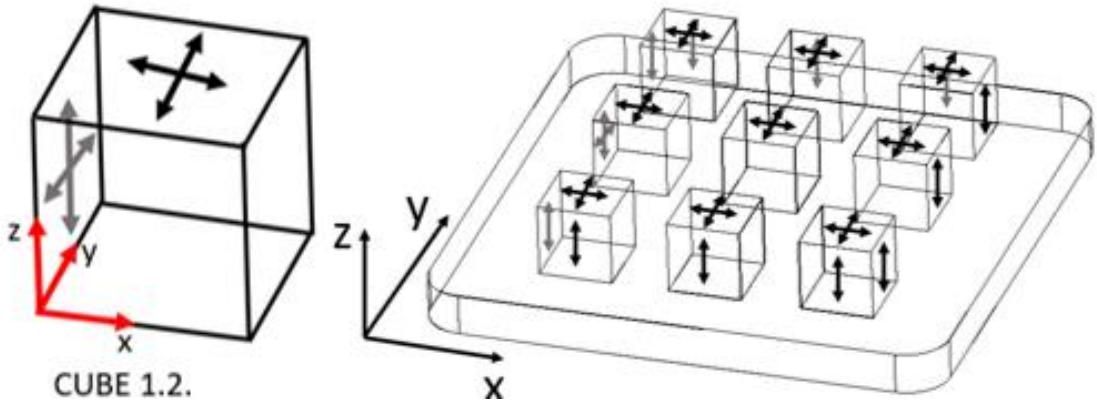

Figure 45. Schematic representation of faces subjected to roughness evaluation.

4.1.4. Statistical analysis

In addressing the quantity of samples and their placement on the building plate, we adopted a comprehensive full factorial design featuring two factors: the x and y coordinates of the blocks, each with three levels. The fabricated blocks were uniformly distributed across the building plate, allowing for a simplified labeling system using numerical designations 1, 2, and 3 within the designated direction. Figure 46 provides a schematic illustration of the complete factorial plan, detailing the precise positioning of the specimens.

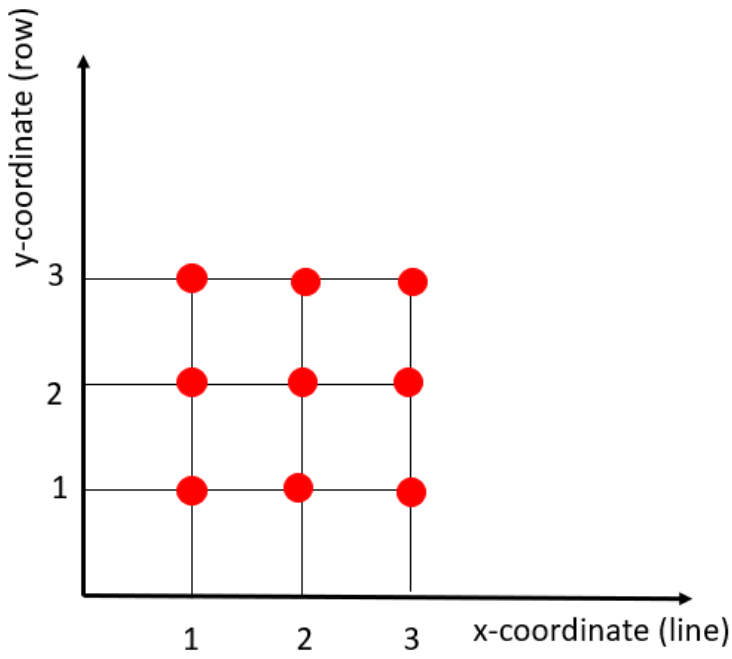

Figure 46. Schematic representation of full factorial plan and position labelling

The effect of the x- and y-coordinate of the position of the fabricated block on measured characteristics was assessed by ANOVA. Response surface methodology was used, and the level of significance (α) was set up to 0.95.

4.2. Numerical model

Notably, the relatively large size and number of the specimens applied in this study require large computational time when reproducing the manufacturing process in numerical simulations. In such cases, it is necessary to find a good balance between the required level of detail and the computational time. We have therefore determined that this experimental set-up requires macroscopic approach, simulating the manufacturing process. Therefore, the mesoscale numerical model, introduced in Chapter 3 could not have been adopted. Instead, the fabrication of nine cubical specimens was reproduced in macroscale simulation within finite element analysis (FEM), where commercial software Simufact Additive (Hexagon, Sweden) was adopted.

The simulation was conducted in thermomechanical mode, consisting of thermal transient analysis and inherent strain method coupled according to the steps of thermal calculation. While the thermal part of the calculation enabled the simulation of the global temperature curve based on the essential process parameters, the mechanical computation predicted the residual stresses and distortion behaviour according to the typical non-elastic strain component – the

inherent strain. This numerical approach is especially suitable for simulating a build with multiple parts on the base plate – such as in this case.

The simulation closely mimicked the experimental sample fabrication with the process properties as described above. Table 13 shows boundary conditions applied in the simulation.

Table 13 Boundary conditions applied in simulation.

Boundary conditions	
$T_{(x,y,z,0)} = T_0$	T_0 =200 °C
$x, y, z \in S$	$k\frac{\partial T}{\partial n} - Q = h(T - T_0) + \sigma_{sb}\varepsilon(T^4 - T_0^4)$

Moreover, the base plate represented a fixed displacement boundary condition at the bottom nodes of the fabricated blocks.

During the building, blocks were discretized into the voxel mesh consisting of about 640000 hexahedral elements. Each block was divided into 40 simulated layers, which consisted of around 41 real powder layers.

All material properties of AlSi10Mg powder used in the simulation were taken from the Simufact material library. Good agreement with material properties stated by the supplier of the powder was confirmed. Table 14 and Figure 47 show selected material properties of AlSi10Mg powder applied in FEM simulations.

Table 14 Selected material properties of AlSi10Mg powder

Thermal properties	
Thermal conductivity [W/(m.K)]	120
Specific heat capacity [J/(g.K)]	0.898
Dissipation factor	0.7
Solidus temperature [°C]	585.0
Melting temperature [°C]	660.0
Evaporation temperature [°C]	2519.0
Mechanical properties	
Poisson's ratio	0.34
Thermal expansion coefficient [1/K]	2.06e-05
Yield strength [MPa]	240.0
Tensile strength [MPA]	460

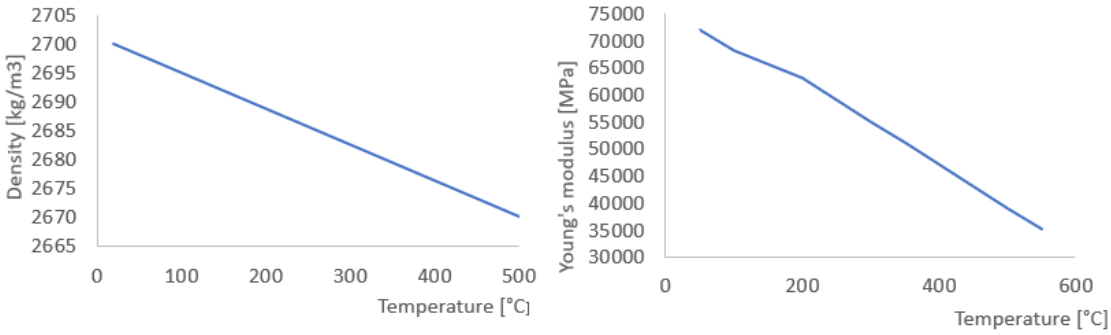

Figure 47. Temperature-dependent density and Young's modulus of AlSi10Mg powder

FEM analysis is conducted to determine the distortions in fabricated parts and deviation in the distance between every two parallel faces.

4.3. Results and discussion

4.3.1. Dimension accuracy

The results of the planarity, parallelism and perpendicularity errors assessment are reported in Table 15. Table 16 reports the measured x-, y-, and z-dimensions of examined cubes, including the related uncertainties. Calculated uncertainties turn out to be at least two orders of magnitude greater than the CCM accuracy, therefore they can be considered negligible. Finally, total uncertainties are displayed in Table 17.

Table 15 Results from the measurement process.

[mm]	Block 1.1	Block 1.2	Block 1.3	Block 2.1	Block 2.2	Block 2.3	Block 3.1	Block 3.2	Block 3.3
PLANARITY X1	0.0819	0.0598	0.1090	0.0939	0.1612	0.0067	0.1134	0.1771	0.1019
PLANARITY X2	0.0869	0.1471	0.1504	0.0997	0.0980	0.1206	0.0777	0.1382	0.0753
PLANARITY Y1	0.1536	0.6980	0.1322	0.0715	0.1540	0.0980	0.1104	0.0722	0.1532
PLANARITY Y2	0.1201	0.1018	0.1240	0.0792	0.1217	0.1605	0.0754	0.1049	0.0809
PLANARITY Z1	0.0164	0.0015	0.0150	0.0079	0.0002	0.0009	0.0190	0.0025	0.0167
PLANARITY Z2	0.2632	0.3335	0.3699	0.1377	0.2572	0.1684	0.1847	0.0205	0.1570
PARALLELISM X1-X2	0.1755	0.1314	0.2397	0.1539	0.1773	0.1571	0.1611	0.1682	0.1062
PARALLELISM Y1-Y2	0.2265	0.1577	0.1415	0.0933	0.1706	0.2210	0.1127	0.1339	0.0903
PARALLELISM Z1-Z2	0.4993	0.5651	0.5149	0.1474	0.2616	0.1767	0.2208	0.2151	0.1998
PERP Z1-X1	0.1248	0.0798	0.1198	0.1454	0.2039	0.0695	0.1196	0.1771	0.1247
PERP Z1-Y1	0.1536	0.0859	0.1903	0.0687	0.1850	0.1598	0.1161	0.1028	0.1485
PERP Z1-X2	0.0997	0.1471	0.1617	0.0952	0.1166	0.1310	0.0941	0.1385	0.0858
PERP Z1-Y2	0.1541	0.1163	0.1623	0.1064	0.1294	0.1859	0.0886	0.1096	0.0914
PERP X1-Y1	0.1975	0.0662	0.1460	0.0747	0.1578	0.1420	0.1176	0.1064	0.1499

PERP X1-Y2	0.1231	0.1320	0.2068	0.0752	0.1221	0.1629	0.1523	0.1259	0.0809
PERP X2-Y1	0.1695	0.0773	0.1316	0.0808	0.1699	0.1447	0.1201	0.0716	0.1461
PERP X2-Y2	0.1572	0.1539	0.1458	0.0945	0.1135	0.1625	0.1129	0.1022	0.0888
PERP Z2-X1	0.3001	0.3607	0.2778	0.1504	0.2171	0.1167	0.1113	0.1771	0.1080
PERP Z2-Y1	0.1580	0.1734	0.1610	0.0983	0.1887	0.1362	0.1778	0.0763	0.1592
PERP Z2-X2	0.3965	0.4422	0.3976	0.0937	0.1025	0.1309	0.1218	0.1490	0.1440
PERP Z2-Y2	0.1264	0.2396	0.1152	0.0867	0.1268	0.1621	0.0993	0.1422	0.1128

Table 16 Dimensions of the sides of the 9 cubes under test and their measuring uncertainties.

Block sides	**Lx [mm]**	**Ly [mm]**	**Lz [mm]**
Block 1.1	35.0461 ± 0.5631	35.0603 ± 0.4214	34.8002 ± 0.7691
Block 1.2	35.0158 ± 0.6293	35.0691 ± 0.7942	34.8984 ± 0.8855
Block 1.3	35.0387 ± 0.6063	35.0468 ± 0.3932	34.8633 ± 0.8233
Block 2.1	35.1344 ± 0.3255	35.1081 ± 0.2308	34.5353 ± 0.3199
Block 2.2	35.0738 ± 0.4240	35.1048 ± 0.4165	34.6156 ± 0.4973
Block 2.3	35.0847 ± 0.3033	35.1186 ± 0.4348	34.5511 ± 0.3351
Block 3.1	35.0859 ± 0.3085	35.0872 ± 0.3055	34.6407 ± 0.3655
Block 3.2	35.0515 ± 0.4276	35.0886 ± 0.2976	34.6823 ± 0.3883
Block 3.3	35.0360 ± 0.2874	35.1267 ± 0.3265	34.6315 ± 0.3466

Table 17 Total uncertainty of the sides of the cubes.

	Block 1.1	**Block 1.2**	**Block 1.3**	**Block 2.1**	**Block 2.2**	**Block 2.3**	**Block 3.1**	**Block 3.2**	**Block 3.3**
U_x	0.5656	0.6295	0.6076	0.3494	0.43044	0.3149	0.3203	0.4307	0.2897
U_y	0.4257	0.7972	0.3959	0.2549	0.42575	0.4507	0.3177	0,3010	0.3502
U_z	0.7947	0.8913	0.8346	0.5641	0.62861	0.5602	0.5125	0.5017	0.5059

The uncertainties in this study were primarily influenced by flatness errors on the Z2 faces, with Cubes 1, 2, and 3 (refer to Figure 37) exhibiting more pronounced construction uncertainties. The maximum calculated uncertainty value is 2.5% at a 68% confidence level. It was observed that the thermal conditions at the boundaries of the cubes during deposition play a substantial role in influencing the uncertainties of their respective sides, a confirmation made evident in subsequent investigations.

To corroborate the experimental findings, a validation process was employed by comparing dimension deviations obtained through numerical simulations. Table 18 provides a comprehensive overview of the experimental and simulated deviations in the distance between each pair of parallel faces for every cubical specimen. In both experimental and numerical campaigns, the deviation was computed based on the nominal value of 35 millimetres, aligning with the CAD models used in the fabrication of the cubes. Additionally, the relative error

between experimental and simulated data was calculated, with face labeling consistent with the conventions outlined in Figure 38.

Table 18 Measured deviation of the distance between parallel faces of the blocks.

	Dimensions deviation [mm]								
	[PX1PX2]			[PY1PY2]			[PZ1PZ2]		
	Exper.	Simulated	Error [%]	Exper.	Simulated	Error [%]	Exper.	Simulated	Error [%]
Block 1.1	0.0461	0.0434	5.86	0.0603	0.0581	3.65	-0.1998	-0.2102	-5.21
Block 1.2	0.0158	0.0149	5.70	0.0691	0.0675	2.32	-0.1015	-0.1078	-6.2
Block 1.3	0.0378	0.0352	6.88	0.0468	0.0476	-1.71	-0.1367	-0.1419	-3.8
Block 2.1	0.1344	0.1298	3.42	0.1081	0.1002	7.31	-0.4647	-0.4762	-2.48
Block 2.2	0.0738	0.0719	2.58	0.1048	0.0996	4.96	-0.3844	-0.3721	3.2
Block 2.3	0.0847	0.0836	1.30	0.1186	0.1009	14.92	-0.4489	-4.4431	1.29
Block 3.1	0.0859	0.0862	-0.35	0.0872	0.0887	-1.72	-0.3593	-0.3607	-3.17
Block 3.2	0.0515	0.0524	-1.74	0.0886	0.0901	-1.69	-0.3177	-0.3099	2.45
Block 3.3	0.0360	0.0376	-4.44	0.1267	0.1281	-1.10	-0.3685	-0.3703	-5.92

The simulated and experimental data exhibited good agreement, with minimal relative error observed in the deviation of the distance between X faces in block 3.1. In contrast, the maximal relative error was noted in the deviation of the distance between Y faces in block 2.3.

Statistical analysis revealed a significant impact of the fabricated blocks' positions on the building plate on the dimensional accuracy of x-oriented, y-oriented, and z-oriented faces of cubes, yielding R^2 values of 96.30%, 93.09%, and 99.79%, respectively. The x-oriented faces' distances were predominantly influenced by the y-coordinate of the position (P-value: 0.029), with a lesser influence from the x-coordinate (P-value: 0.075). Conversely, the distances between y- and z-oriented faces were influenced by the x-coordinate (P-values: 0.021 and 0), while the y-coordinate exhibited P-values of 0.291 and 0.064, respectively.

Figure 48 depicts main effects plots illustrating the impact of blocks' positions on dimension accuracy. Black dots represent average distortion based on cube position during construction. Since cube position is categorical in this study, main effect plots feature unconnected points. Nevertheless, it is evident how the y-coordinate (representing average distortion) changes across 1, 2, or 3 categories on the x-axis (classifying cube position in a row or column). This facilitates the determination of the cube's position effect on average distortion

(y-axis). An increase in the y-coordinate in the positive direction indicates that altering the cube's position on the building plate leads to increased distortion, applicable to all main effect plot figures.

Across all the manufactured specimens, it was detected that the sample heights were suboptimal, necessitating compensation through additional layers or CAD file modification. In the x-direction, position 1 exhibited minimal height distortions, while the y-direction showed almost negligible significance. The first block (1.1) was the coldest, contributing to improved distortions for both PX1PX2 and PY1PY2.

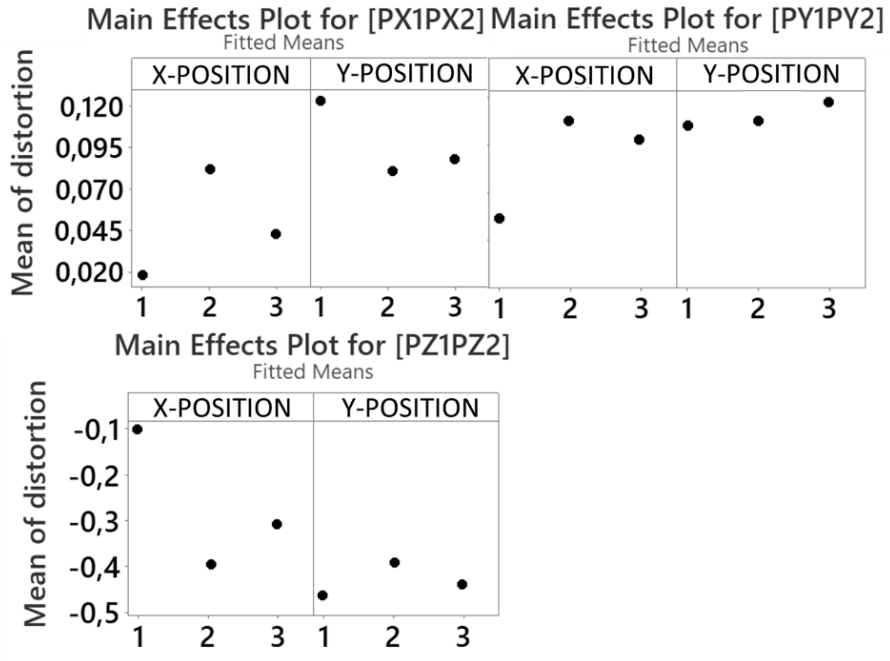

Figure 48. 15 Main effects plots of dimension accuracy

Finally, the regression equations were drawn for each of the measured and analyzed distortions of distances. Regression equations are shown in Table 19. The x and y parameters stand for the x- and y-dimensions of the position on the base plate.

Table 19 Regression equations for distortions of the distances between x-, y- and z-oriented faces.

	Regression equation
[PX1PX2]	$-0.0618 + 0.2416\,x - 0.0923\,y - 0.05212\,x^2 + 0.02378\,y^2 - 0.01040\,xy$
[PY1PY2]	$-0.0010 + 0.1174\,x - 0.0355\,y - 0.03072\,x^2 + 0.00378\,y^2 + 0.01325\,xy$
[PZ1PZ2]	$0.2100 - 0.8068\,x + 0.2949\,y + 0.18542\,x^2 - 0.06178\,y^2 - 0.01808\,xy$

In evaluating dimensional accuracy, our analysis revealed an anomaly limited to undersized z-dimensions of the manufactured blocks. In contrast, Maamoun et al. [236] reported a trend

of oversized specimens. They attributed the increased dimensions to the balling effect, wherein partially melted particles adhered to the sample surface during fabrication. The diminutive dimensions of the examined blocks may be caused by the absence of the balling effect, attributable to distinct dynamics within the manufacturing process [237, 238]. This interpretation is further substantiated by the visibly clean appearance of the manufactured cubes, characterized by a smooth finish devoid of discernible coarse particles attached to the surfaces (Figure 36). The z-dimensions are additionally impacted by the employed slicing algorithm and recoating operations during manufacturing.

The noted influence of position on the dimensional accuracy of the fabricated is caused by variations in thermal fields across different positions on the building plate. Blocks positioned at the horizontal and vertical center experience heat accumulation from both sides, resulting in a lower thermal gradient, as corroborated by simulations (refer to Figure 49).

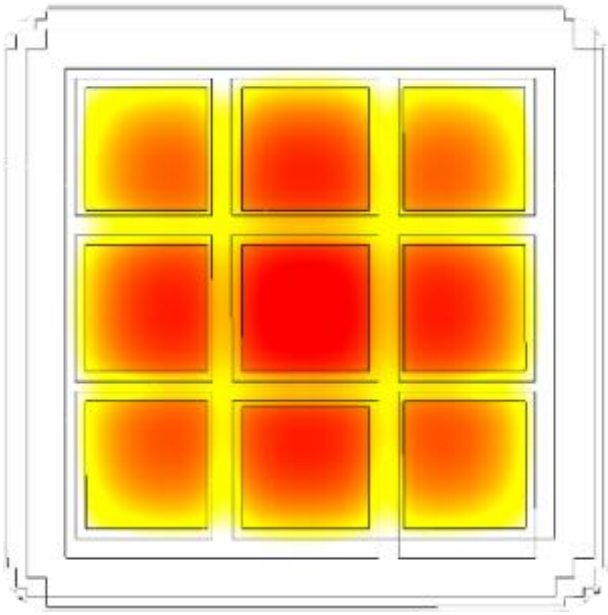

Figure 49. Simulated thermal fields of blocks during the building.

The varying thermal fields within the building plate closely correlate with the strains of the fabricated cubes. The thermal expansion of fabricated cubes gets partially hampered by surrounding colder materials, which results in compressive straining in affected areas. If the yield condition is fulfilled, plastic strains, effectuating the non-restorable plastic deformation occur [238, 239]. During the manufacturing, effective plastic strains were located mainly around the edges and the building plate of fabricating specimens, as such areas represent the interface between high-temperature laser-heated material and colder unheated powder or the

building plate (Figure 50). The effect of cold building platform might be minimized by platform preheating.

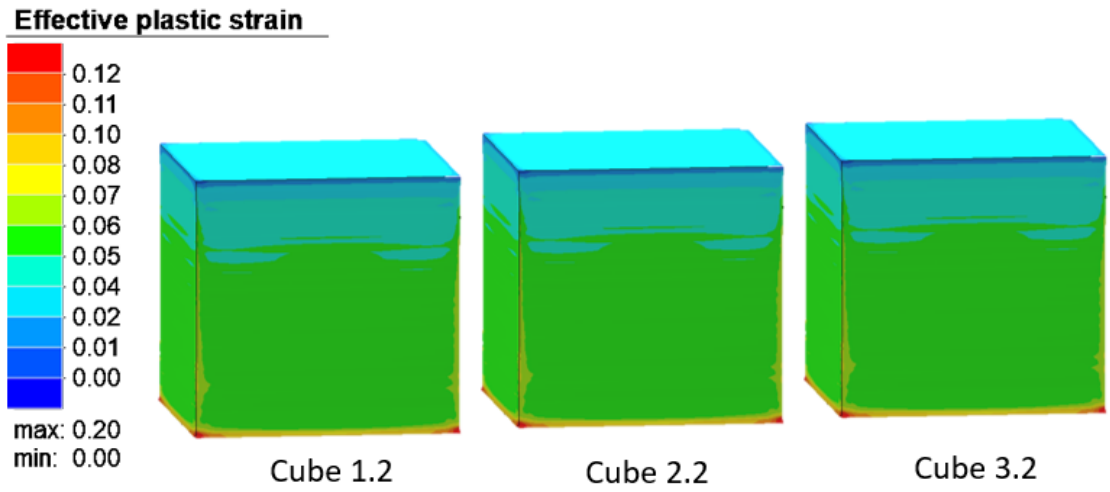

Figure 50. Distribution of plastic strains in cubes during the building phase.

Upon the completion of the construction phase, the specimens ceased to be subjected to laser heating, initiating a phase of rapid cooling characterized by elevated cooling rates. Consequently, the plastic strain distribution within the cooling specimens underwent a notable transformation. Substantial variations, contingent upon the specimen's spatial placement, were discerned among the manufactured samples, with the minimal strains recorded in specimens situated in position 2, as illustrated in Figure 51.

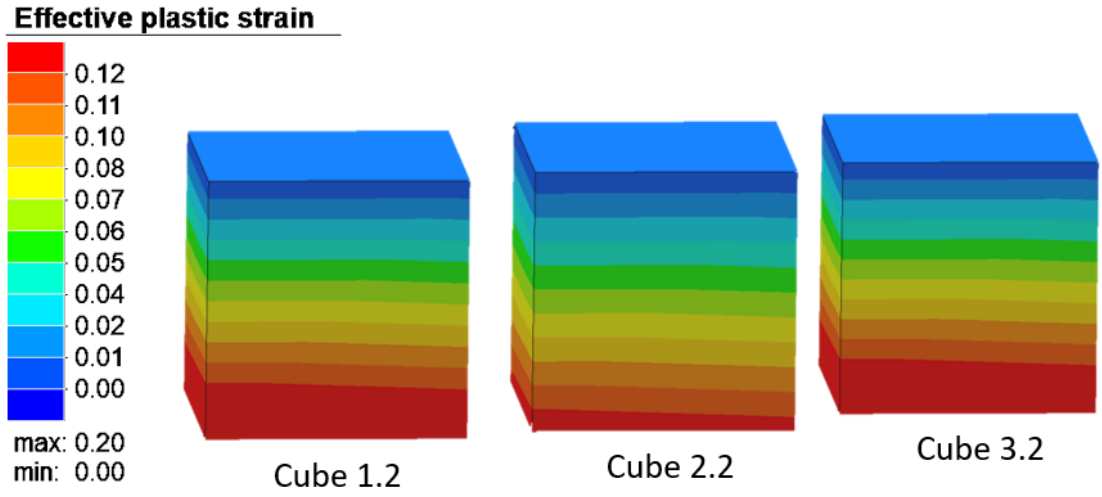

Figure 51. Distribution of effective plastic strains in cubes after cooling

The identified trend is likely attributable to deviations in thermal fields and associated thermal gradients, as illustrated in Figure 46. A conspicuous variation in plastic strains along the z-axis was consistently observed across all specimens, with the highest strains concentrated

near the lower regions where specimens are affixed to the base plate. This observed strain distribution can be rationalized by the constraint of the fabricated cubes to the building platform, which interferes with the expected shrinkage patterns of the cooling material [239, 240].

Examining the strains from a transversal perspective revealed minimal disparities compared to the surface distribution, as depicted in Figure 52. The marginal distinctions in the distribution of effective plastic strains in the ZX- and ZY-planes can potentially be ascribed to variations in the direction of the building order. However, it is noteworthy that the employed scanning strategy exhibits negligible influence on the deviation of plastic strain distribution in the examined planes, given that the scanning direction undergoes rotation between successive layers.

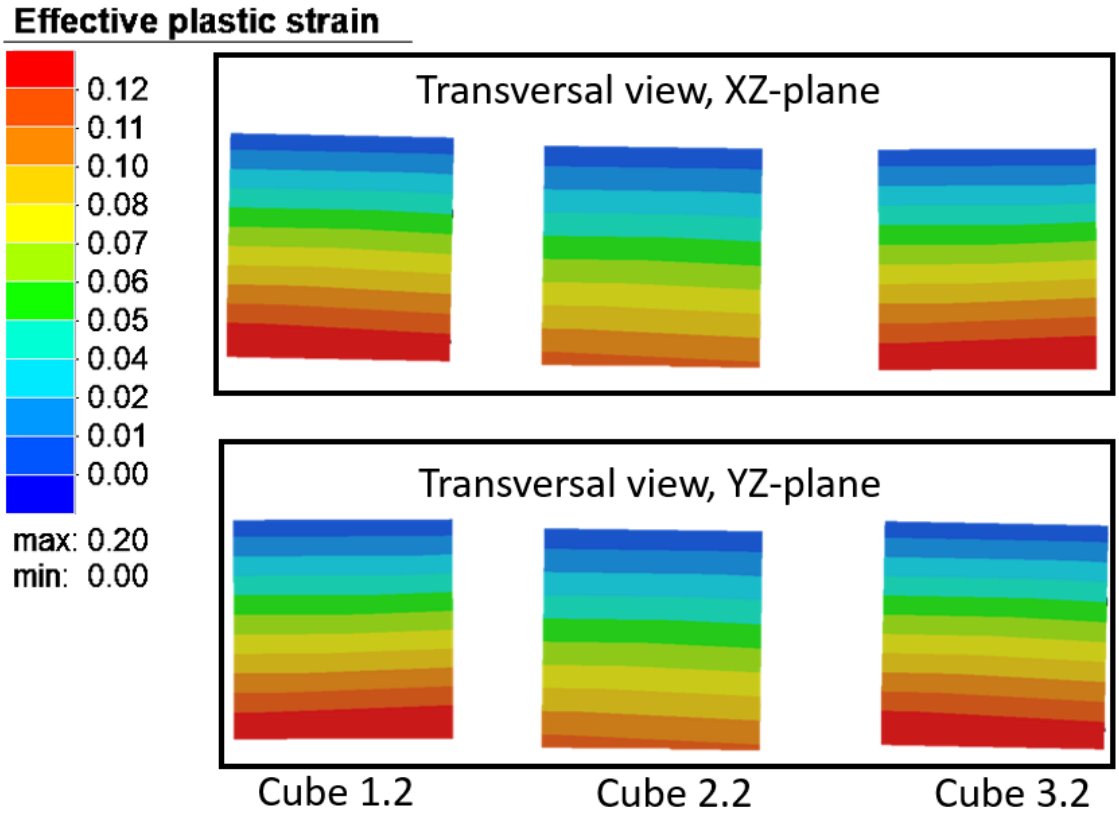

Figure 52. Distribution of effective plastic strains in cooled specimens in transversal view

4.3.2. Planarity

The planarity measurements for all faces of the examined blocks are presented in Table 15. Notably, the Z1 surface, represented by the base plate, exhibited the least planarity deviation. The flatness of the base plate was rigorously verified using a CMM, which accurately detected multiple points on it, excluding the faces of the attached cubes. The Z1 surface was

consequently adopted as the reference for measurements along the z-axis, with any planarity distortion deemed negligible, given the minimal error associated with the base plane in comparison to other assessments.

Conversely, the Z2 faces displayed the highest planarity deviations. The elevated errors in Z2 faces can be attributed to the thermal expansion of the material and the unrestricted flow of material towards the top layers, contrasting with the constrained bottom layers adhering to the previous layers or the building platform. The primary source of distortion lies in the material located at the top layers, manifesting as prominent distortions in the upper faces of the specimens. This observation is supported by FEM simulations, which reveal that the highest distortions are concentrated in the upper part of specimens, while the constrained bottom part, anchored by the building platform, exhibits minimal distortions.

The as-built cube 1.2, in a partially cooled state, vividly illustrates this distortion distribution and uneven top surfaces (see Figure 53).

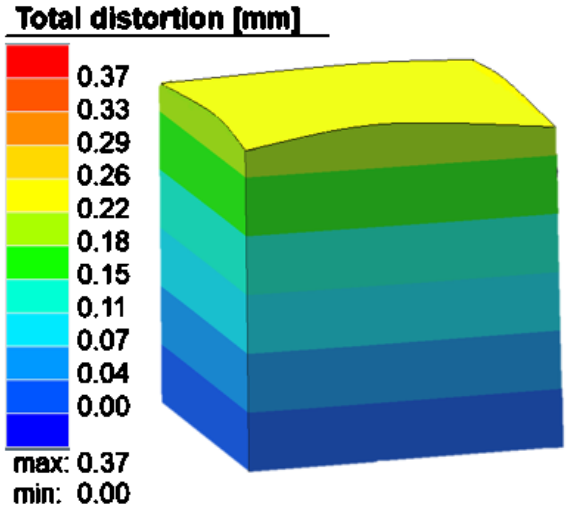

Figure 53. Distortions in cube 1.2 in partially cooled state.

Figure 54 illustrates the distortions exhibited by cube 1.2 in its cooled state along the x-, y-, and z-directions. Notably, the distortions in the z-direction mirror the overall distortion distribution, with minimal distortions near zero predominantly concentrated in the lower section of the specimen. Concurrently, the absolute values of distortions escalate in the z-direction, wherein negative values indicate undersized dimensions of the cube. In contrast, distortions in the y-direction follow a similar distribution pattern, with the least distortions

observed in the lower part of the cube, progressively increasing in the z-direction. At the upper extremity of the specimen, deformation is more pronounced on the front side, less influenced by thermal flux.

The distortions in the x-direction manifest as compressive in the lower portion of the sample and tensile in the upper region. It is noteworthy that the x- and y-distortions are markedly influenced by the applied scanning strategy and building sequence [240].

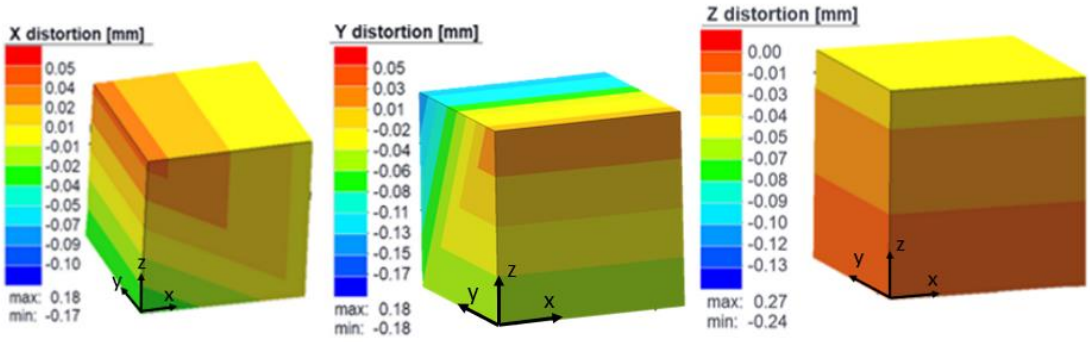

Figure 54. Distribution of unscaled x-, y- and z-distortions in cube 1.2 in cooled state.

Additionally, gravity forces, reacting perpendicularly to Z2 faces, causing viscous flow of molten material, are causing the distorted, bumpy top faces. It should be noted that temperature affects the flowability of the molten metal, as it is described in Bernard-Marangoni convection. The Marangoni effect occurring in molten metals processed by L-PBF is a well discussed topic [241].

Statistical analysis of measured planarity confirmed the position dependence of planarity of Z2 faces (with R^2 of 94.54%). It was, however, mainly influenced by the X-coordinate, the influence of the y-coordinate was not statistically significant (P-value of the x-coordinate was 0.012, while P-value of the y-coordinate was 0.243). Furthermore, the effect of the position of the blocks on the planarity of the remaining faces of the cubes was not statistically significant.

Figure 55 shows the main effect plots for the planarity of Z2 faces. Position 1 presented the worst and better values, respectively in y direction and x direction. There was not a big difference in values of planarity for blocks in position 2 and 3.

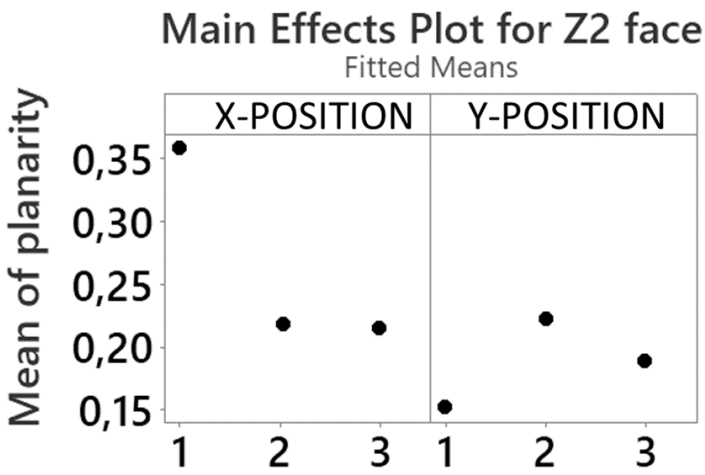

Figure 55. Main effects plots for planarity of Z2 faces.

The strong influence of x-position can be attributed to different thermal gradients, which have been discussed previously. Specimens in position 1 were always the first to be built in their respective line, according to the building sequence, making them the coldest and most susceptible to shrinkage. As specimens in position 2 were built, heat was accumulated and transferred to the rear sides of specimens in position 1. This uneven thermal gradient resulted in distortions affecting the planarity of the top faces of cubes in position 1. The proximity of the front parts of specimens in position 1 to the building chamber door may have contributed to the uneven thermal gradients, as the door did not provide perfect thermal isolation. The effects of proximity to the door of the building chamber on distortions of the specimens manufactured by L-PBF have already been discussed in literature [242].

The effects of x- and y-dimension of the building position on the planarity of Z2 faces can be further described by the regression equation, as shown in Table 20. The regression equation was drawn based on statistically analyzed experimental data.

The significant influence of the x-position is attributed to distinct thermal gradients, which have been extensively addressed in prior discussions. Specimens situated in position 1 consistently being the first ones to be deposited according to the predefined building sequence, are consequently rendered to be the coldest and most prone to shrinkage. As specimens in position 2 were progressively fabricated, thermal energy was accumulated and propagated to the posterior facets of specimens in position 1. This asymmetric thermal gradient precipitated distortions that adversely impacted the planarity of the upper surfaces of cubes in position 1. The proximity of the frontal segments of specimens in position 1 to the entrance of the building chamber potentially contributed to these irregular thermal gradients, given that the door failed

to provide complete thermal isolation. The effects of proximity to the building chamber door on distortions in specimens produced by L-PBF have been previously described in the literature [242].

The impacts of both the x- and y-dimensions of the positioning on the planarity of Z2 faces can be explained further through the regression equation, as delineated in Table 20. This equation was derived from a statistical analysis of experimental data.

Table 20. Regression equation for planarity of Z2 faces.

	Regression equation
Z2	$0.242 - 0.2607\,x + 0.2929\,y + 0.0645x^2 - 0.0518\,y^2 - 0.0336\,xy$

4.3.3. Parallelism

The measured deviations of the parallelism between every two parallel faces of cubical specimens are shown in Table 15.

The analysis revealed minimal deviation in parallelism between Y faces within block 3.3, with a similarly low deviation observed among X faces in the same block. The study, however, did not establish a conclusive link between the position of blocks and the parallelism of X- and Y-oriented faces, as indicated by R^2 values of only 53.87% and 37.20%, respectively. This suggests a nuanced relationship among parameters influencing parallelism errors for X- and Y-faces, extending beyond the second polynomial order between the positional X- and Y-parameters, as assumed in the adopted Response Surface Methodology analysis.

In addition to specimen positioning and the adopted building sequence, factors such as laser head positioning during layer scanning, energy variations, and porosity presence may contribute to parallelism errors [243, 244]. Notably, the parallelism of Z-oriented faces is predominantly influenced by the x-coordinate of block positioning on the building plate (P-value = 0.001), whereas the statistical significance of the y-coordinate remains unsubstantiated (P-value = 0.789). The ANOVA analysis yielded an R^2 of 98.47%, affirming the substantial impact of the x-coordinate, a finding further supported by the regression equation presented in Table 21.

Table 21 Regression equation for parallelism of z-oriented faces

	Regression equation
Z1IIZ2	$0.981 - 0.835\,x + 0.239\,y + 0.1739x^2 - 0.0541y^2 - 0.0092xy$

Figure 56 shows the main effect plot for parallelism between z-oriented faces. A significant resemblance with main effect plots concerning the deviation of the distance between Z faces (Figure 48) was observed.

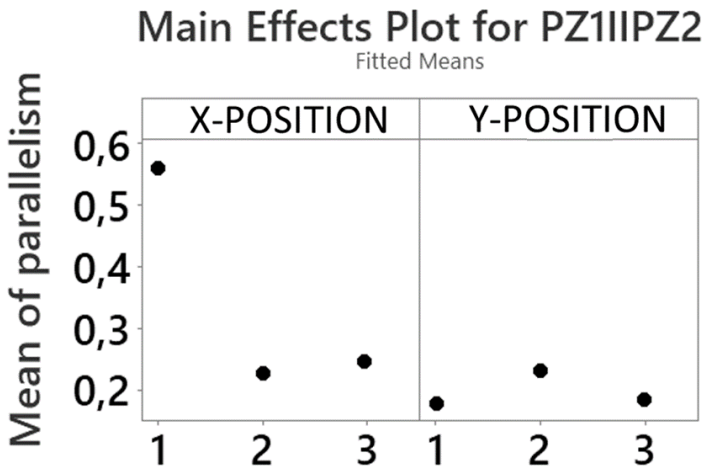

Figure 56. Main effect plots of parallelism between Z-oriented faces.

The parallelism errors between z-oriented faces exhibit a noteworthy correlation with the position-dependent variations in the planarity of the top faces, as described by the main effect plots. This resemblance suggests a commonality in the underlying principles governing the generation of assessed distortions in both planarity and parallelism errors. Consequently, it can be suggested that similar factors contribute to the manifestation of these deviations.

The analysis further reveals that the parallelism error between z-oriented faces is notably influenced by distinct thermal gradients. Specifically, variations in temperature gradients are observed between the colder front section of the manufactured cube and the rear part subjected to heating by specimens in position 2. Moreover, the proximity of the assessed object to the door of the building chamber emerges as an additional factor of influence that warrants consideration in the assessment of parallelism errors.

4.3.4. Perpendicularity

The minimum deviation from perpendicularity was observed between the Z1 and Y1 faces in Block 21, while the maximum deviation occurred between the Z2 and X2 faces in Block 12, as detailed in Table 15.

ANOVA analysis revealed that among all examined faces, the perpendicularity is position-dependent specifically between Z2 and X1 (R^2 99.65%) and Z2 and X2 faces (R^2 99.28%). Significantly, the perpendicularity between Z2 and X1 faces was influenced by the position along the x-axes (P-value of 0), with no statistically significant impact of the y-coordinate within the examined sensitivity range (P-value of 0.073). A similar pattern was noted for the perpendicularity of Z2 and X2 faces, where the x-coordinate exerted a significant influence (P-value of 0), while the y-coordinate exhibited no statistically significant effect (P-value of 0.309). The influence of position on perpendicularity among the remaining faces of the cubes was found to be statistically insignificant.

The perpendicularity error is found to be associated with increasing x- and y-dimensions as the specimen grows. The slight distortion in the x- and y-directions of the initial layers can be attributed to the strong constraint imposed by the building plane, as discussed earlier. As new layers are deposited, the deposition area expands, resulting in the distorted shape of the specimen resembling an inverted frustum of a pyramid. Consequently, adjacent faces cease to be perpendicular. The distorted shape of cube 1.2 in its as-cooled state is illustrated in Figure 57. It is noteworthy that the measured distortions and errors, albeit small, necessitate scaling for meaningful comparison with the cube's dimensions.

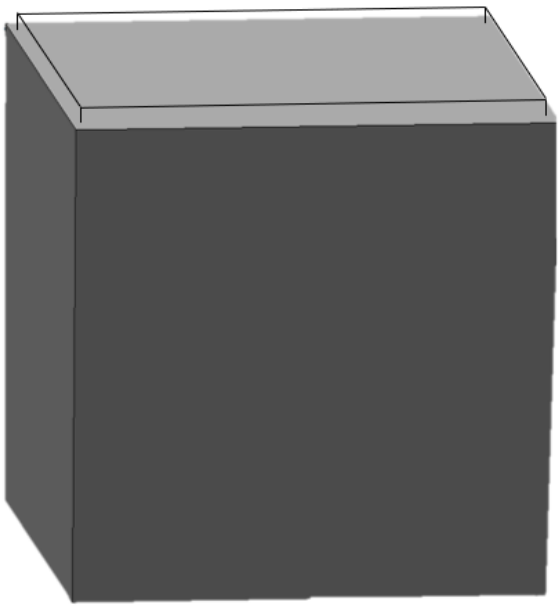

Figure 57. Comparison of intended and distorted shape (10-time magnitude) of cube 1.2 in as-built shape

The perpendicularity errors are intricately tied to the chosen scanning strategy, demonstrating a correlation with distortions in both the x- and y-dimensions, as illustrated in

Figure 45. The dynamic distortions occurring within the x- or y-direction significantly impact the final shape and dimensions of the fabricated cubes, thereby exerting a consequential influence on the perpendicularity among adjacent faces. The positional variations of the blocks play a pivotal role in determining the perpendicularity between faces Z2 and X1, as well as Z2 and X2, as evidenced by the main effect plots in Figure 58.

Notably, the y-position exhibits negligible influence on perpendicularity, whereas in the x-direction, position 1 yields suboptimal results. As previously discussed, the positioning of blocks exerts a discernible impact on perpendicularity errors, specifically between the top and x-oriented faces of the investigated cubes. This correlation is attributed to the adapted building sequence, which induces uneven thermal gradients.

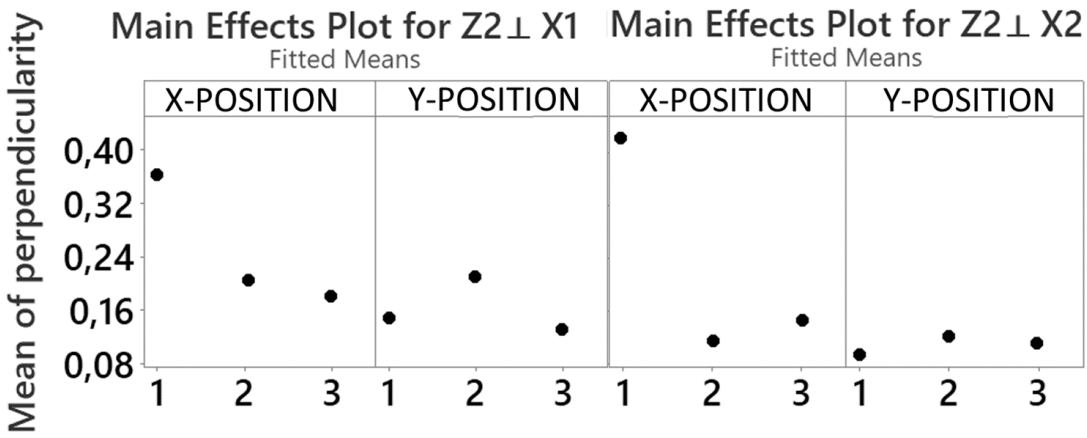

Figure 58. Main effect plots for perpendicularity between Z2 and X1 faces and Z2 and X2 faces.

The regression equations describing the effects of both x- and y-coordinate of building position on the perpendicularity of Z2 and X1, and Z2 and X2 faces are shown in Table 22.

Table 22 Regression equation for perpendicularity of Z2 and X1 faces and Z2 and X2 faces.

	Regression equation
Z2⊥X1	$0.3778 - 0.3443\,x + 0.2776\,y + 0.06110\,x^2 - 0.07425\,y^2 + 0.00475\,xy$
Z2⊥X2	$0.9912 - 0.8121\,x + 0.0681\,y + 0.1662\,x^2 - 0.0171\,y^2 + 0.0053\,xy$

4.3.5. Surface roughness

Table 23 shows the roughness of the selected faces of the blocks.

Table 23 Measured Y2 roughness in selected faces of each examined block.

	Block	**1.1**	**1.2**	**1.3**	**2.1**	**2.2**	**2.3**	**3.1**	**3.2**	**3.3**
X	**Ra**	13.846	14.450	12.389						
1	**Rq**	16.984	17.937	15.763						
	Rz	65.300	73.629	69.653						

	Rt	92.04	97.99	101.53						
X1O	**Ra**		12.529							
	Rq		15.507							
	Rz		65.092							
	Rt		79.77							
X2	**Ra**							20.637	16.846	20.092
	Rq							26.907	21.176	24.890
	Rz							109.950	78.561	95.333
	Rt							136.04	111.96	125.22
Y1	**Ra**	15.868			11.297			15.718		
	Rq	20.135			13.911			19.477		
	Rz	74.935			53.446			76.928		
	Rt	110.81			70.61			100.09		
Y2	**Ra**			16.926			13.802			16.781
	Rq			21.212			18.366			20.919
	Rz			81.307			71.196			85.702
	Rt			111.30			111.57			112.85
Z2	**Ra**	6.843	14.263	9.436	11.365	11.348	10.669	12.337	11.557	8.928
	Rq	10.607	17.596	12.488	17.966	14.592	13.731	17.933	16.763	13.730
	Rz	39.376	70.124	50.643	59.574	55.712	57.545	66.873	58.164	48.378
	Rt	94.98	92.15	75.29	109.43	76.46	85.70	109.54	116.43	116.50
Z2O	**Ra**	11.525	14.053	9.001	14.267	9.340	12.671	9.983	11.670	7.155
	Rq	15.676	19.880	12.697	19.250	13.706	17.644	13.536	16.689	10.667
	Rz	57.223	75.109	48.912	55.176	50.229	58.386	51.932	66.255	40.155
	Rt	94.55	130.98	86.47	99.62	102.36	101.98	86.20	98.82	87.83

Statistical analysis established that the direction of measurements exerted no discernible influence on the surface characteristics of the L-PBF manufactured blocks under evaluation. This conclusion is supported by the non-significant difference in roughness values measured in both standard and orthogonal directions. Specifically focusing on the Z2 faces, our analysis demonstrated that the roughness of these faces remained independent of block position. The R^2 values derived from ANOVA for various roughness parameters (Ra, Rq, Rz, and Rt) on Z2 faces were 62.89%, 55.53%, 61.11%, and 80.50%, respectively. Notably, neither the x- nor y-dimension of the building position exhibited a statistically significant effect on any evaluated roughness type, as evidenced by P-values consistently below the designated threshold for the chosen level of significance.

Addressing a potential concern, the position-dependent length of the laser beam, which could theoretically impact surface roughness, was effectively compensated by position-dependent thermal fields. This compensation was instrumental in demonstrating the absence of a correlation between block position during fabrication and surface roughness. Furthermore, while other research groups have explored the impact of scanning strategy and inert gas flow

on specimen roughness, it is crucial to note that these parameters may be influenced by factors such as the inclination of the laser head during scanning and other machine-related variables [245, 246].

Recognizing the pivotal role of surface roughness in determining the mechanical performance of fabricated specimens, it is crucial to further study the intricate relationship between process parameters, material properties, and overall performance characteristics. A more thorough investigation of this process-property-performance threshold will contribute valuable insights to the field.

5. Pinless friction stir spot process optimisation

In recent years, substantial research efforts have been dedicated to investigating the transformation and enhancement of microstructures, as well as mechanical properties, in specimens produced through LPBF technology. Ongoing research is particularly focused on the application of Friction Stir Spot Processing (FSSP) as a means to achieve these enhancements. However, existing literature highlights that treated specimens frequently experience undesired deformations, especially post-tool retraction [247, 248].

This chapter introduces an innovative approach to FSSP treatment of LPBF-manufactured AlSi10Mg specimens involving a pinless tool. The investigation discerns between deformations induced by the LPBF manufacturing process and those arising from FSSP treatment conducted under diverse processing parameters. The experiments detailed in this chapter substantiate the densifying, homogenizing, and softening effects of the treatment within stir zones and thermo-mechanically affected zones of LPBF-manufactured AlSi10Mg specimens.

Furthermore, this study meticulously analyses the impact of FSSP processing parameters on both the deformation of the processed plane and the effective depth of the treatment. It identifies optimal processing windows where the treatment yields deformations comparable to those originating from the manufacturing process, while ensuring a sufficient effective depth. Remarkably, it is established that this post-processing method is viable even in applications demanding high precision for treated components. Simultaneously, the FSSP treatment with a pinless configuration is found to provide an effective depth surpassing that achievable through alternative methods, such as shot peening treatment.

5.1. Materials and methods

5.1.1. Sample manufacturing

Nine cubical specimens (35x35x35 mm) were fabricated utilizing LPBF technology with the EOSINT M270 manufacturing system, employing AlSi10Mg alloy. All specimens were produced under uniform process parameters, as detailed in Section 4.1.1. The manufacturing process specifics can be found therein. In Figure 59, the produced components are depicted affixed to the base plate, with assigned identification numbers allocated for subsequent processing and analysis.

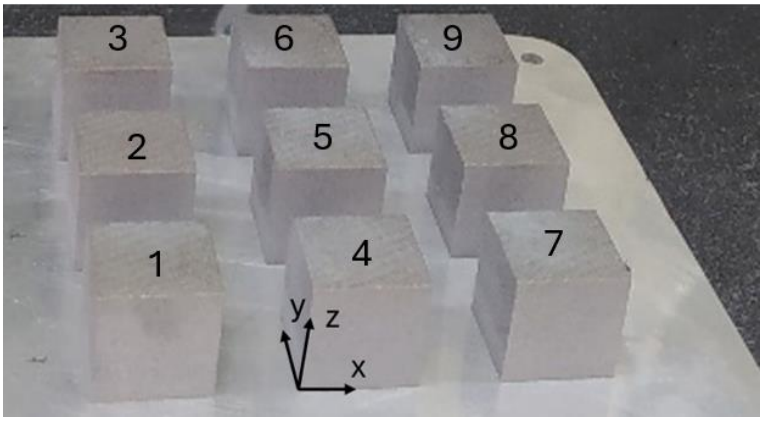

Figure 59 LPBF-manufactured cubes attached to the base plate

5.1.2. Sample processing

In their initial, as-built condition, all specimens underwent processing using the FSSP method. The experimental processing protocol was meticulously formulated in alignment with the principles of the DOE (Design of Experiments). Employing a full factorial design with two factors and three levels, as detailed in Table 24, ensured a comprehensive exploration of the parameter space. The selection of FSSP process parameters was informed by an exhaustive preliminary literature review, aimed at achieving an optimal thermomechanical effect while mitigating the risk of undesirable surface deformations.

Table 24 Parameters of FSSP processing

Cube	**Dwell time** [s]	**Rotational speed** [rpm]
1	5	2000
2	5	1500
3	10	1000
4	7.5	2000
5	7.5	1500
6	7.5	1000
7	10	2000
8	10	1500
9	5	1000

The FSSP treatment was carried out in a position-controlled mode, maintaining a constant plunge depth of 0.8 mm for all specimens throughout the entire process. The rotating tool utilized during the treatment featured a 30-millimeter diameter shoulder. The specimens were subjected to FSSP treatment while remaining affixed to the building plate, and their positions were securely held in place using clamping tools. Figure 60 shows the scheme of FSSP treatment.

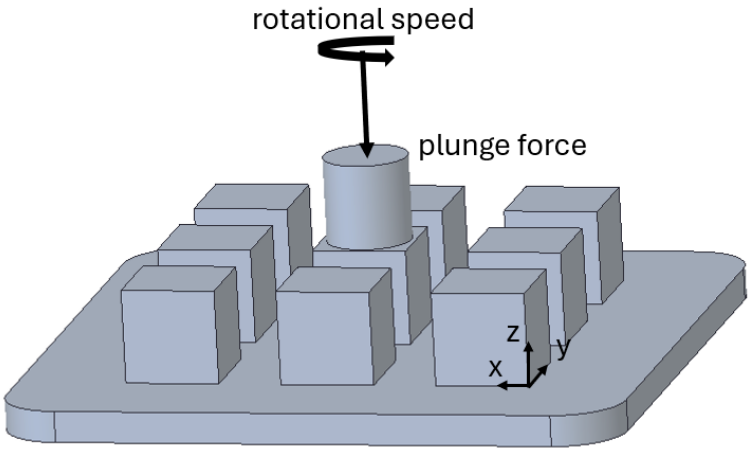

Figure 60 Scheme of FSSP treatment

5.1.3. Deformation assessment

The fabricated blocks were assessed using a tactile coordinate measuring machine (CMM), specifically the Altera LK coordinate measuring machine. This machine is inherently capable of measuring specimens with dimensions up to 1500x1000x800 millimeters, exhibiting a remarkable volumetric accuracy of 1.1 µm+L/375 and a repeatability of 0.7 µm. The applied measuring system boasts a maximal speed of 720 mm/s and a maximal acceleration of 1,900 mm/s^2.

In Section 4.1.2, the methodology for assessing the deformation of the specimens in their as-built state is elucidated. Subsequent to the FSSP treatment, the specimens underwent further measurements using the same equipment employed in their as-built state. The deviation in the height of the specimens in the as-processed state, denoted as Dz, was determined by evaluating the difference in the z-coordinate of measuring points on the top plane of the cubes in both the as-built and as-processed states.

The deformation of the top plane of the processed specimens was assessed by measuring the distances between parallel edges of the cubes at the corners and middle of the lengths, as illustrated in Figure 61.

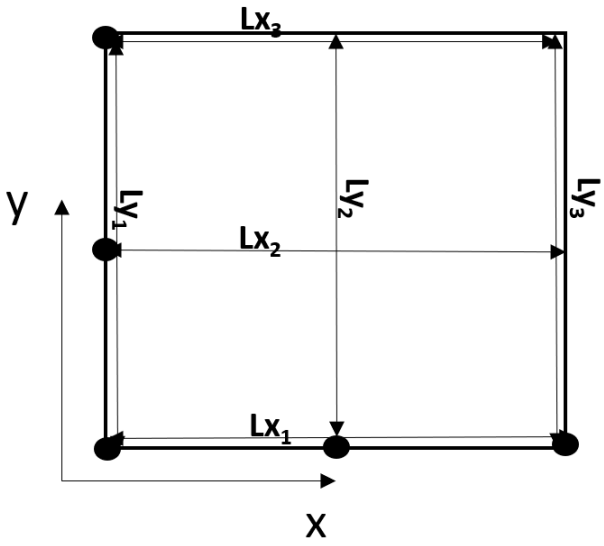

Figure 61 Measured dimensions in processed planes

The level of deformation in the processed plane caused by FSSP treatment was then determined as the difference between LX_2, or LY_2 values with the designed dimension (35 millimeters) and deviation in x-, or y-dimension of the specimen in as built-state (Ax, or Ay): (32, 33)

$$D_x = L_{x2} - 35 - A_x \text{ [mm]} \quad (32)$$

$$D_y = L_{y2} - 35 - A_y \text{ [mm]} \quad (33)$$

5.1.4. Optical analysis

Following the application of the FSSP treatment, the specimens underwent transverse sectioning and were subsequently subjected to metallographic examination. The microstructure of the FSSP-treated samples was inspected through cross-sectional analysis utilizing optical microscopy. Prior to optical assessment, the specimens underwent standard metallographic preparation, involving etching with Keller's reagent solution (composed of 1% HF, 1.5% HCl, 2.5% HNO3, and 95% H2O). The analysis of the maximal width of the TMAZ (Thermomechanically Affected Zone) was conducted based on pixel counting methodology.

5.1.5. Microhardness testing

Microhardness measurements were conducted employing specialized microhardness testers equipped with a Vickers diamond indenter. A precisely controlled load of 0.3 kgf was applied for a dwell time of 15 seconds. The testing trajectory was oriented transversely across the width of the processed specimen in the positive x-direction. To mitigate potential indenter-

induced strain hardening effects, the testing interval was maintained at 5 times the size of the indenter. Importantly, reference microhardness data was exclusively obtained for specimen 1.

5.1.6. Statistical analysis

The influence of FSSP process parameters, specifically rotational speed and dwell time, on the induced deformations and the depth of the Thermal-Mechanical Affected Zone (TMAZ) was systematically investigated through statistical analysis. Analysis of Variance (ANOVA) was employed within the framework of Response Surface Methodology (RSM), considering a significance level of 0.95. Additionally, a desirability analysis was conducted to optimize the FSSP process parameters, aiming to minimize distortions while maximizing the effective depth of processing. The composite desirability parameter was computed to assess the overall performance. The statistical software Minitab 20 (Minitab, USA) was employed for data analysis and interpretation.

5.2. Numerical model

The described experimental campaign was reproduced in FEM simulations applying Simufact Additive (manufacturing of the samples) and Simufact Forming (processing of the samples).

5.2.1. Numerical modelling of building phase

In the simulation of the manufacturing process, we implemented the thermomechanical module, specifically enforcing a nuanced coupling between thermal and mechanical calculations. For an in-depth understanding of the numerical model intricacies and the boundary conditions applied, please refer to Section 4.2.

5.2.2. Numerical model of the processing phase

After the initial step of numerical modelling, simulated outcomes were imported into the commercial Finite Element Analysis (FEA) software Simufact Forming, wherein the FSSP treatment was applied. The temperature distribution within the processed specimen was determined using transient heat conduction and the finite difference method, while the mechanical behaviour was assessed through the incremental finite element method.

Both thermal and mechanical computations were concurrently conducted at each time step of the simulation. Rather than directly computing the precise contact properties between the specimen and the rotating tool, Simufact Forming utilized a near-contact tolerance and a

specific formula to approximate thermal heat transfer. This approach notably enhanced the time-effectiveness of the simulation.

The processing tool, blank holder, and substrate table, which governed the position of the processed cube, were modelled as rigid bodies employing the Lagrangian method. These components were discretized into tetrahedral meshing elements with an initial size of 0.5 mm. Conversely, the cube, treated as a deformable body using the Arbitrary Lagrangian-Eulerian method, was discretized into hexahedral elements with an initial size of 0.3 mm. The generated mesh moved independently from the material, facilitating significant material deformation while preserving the fixed reference configuration. Frequent re-meshing cycles were incorporated, with the re-meshing condition determined by the permissible deformation. The configuration employed in the numerical simulations is illustrated in Figure 62.

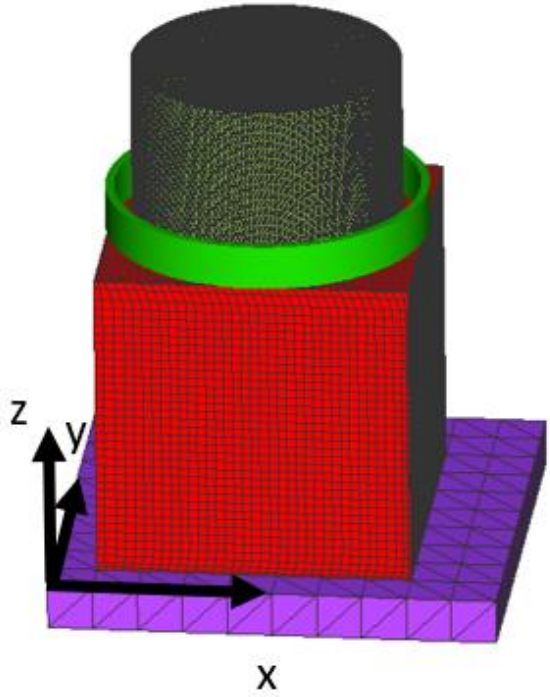

Figure 62 Working set-up applied in numerical simulations

5.3. Results and discussions

5.3.1. Deformations induced by the building process

The LPBF manufacturing process has resulted in seemingly regularly shaped specimens with well-defined edges and rougher surface finish, as it is demonstrated in Figure 63.

Figure 63 Cubes in as-built state

A comparison between the measured and simulated dimensional deviations of the cubes in their as-built state is presented in the Table 25. The experimental and simulated values exhibit a high degree of agreement, as evidenced by the low relative error. This agreement validates the accuracy of the numerical model employed in the simulations.

Table 25 Comparison between experimental and simulated dimension deviations of cubes in as-built state

	Dimensions deviation [mm]								
	[AX]			[AY]			[AZ]		
Block	**Exper.**	**Simulated**	**Error [%]**	**Exper.**	**Simulated**	**Error [%]**	**Exper.**	**Simulated**	**Error [%]**
1	0.0461	0.0434	5.86	0.0603	0.0581	3.65	-0.1998	-0.2102	-5.21
2	0.0158	0.0149	5.70	0.0691	0.0675	2.32	-0.1015	-0.1078	-6.21
3	0.0378	0.0352	6.88	0.0468	0.0476	-1.71	-0.1367	-0.1419	-3.80
4	0.1344	0.1298	3.42	0.1081	0.1002	7.31	-0.4647	-0.4762	-2.47
5	0.0738	0.0719	2.58	0.1048	0.0996	4.96	-0.3844	-0.3721	3.20
6	0.0847	0.0836	1.30	0.1186	0.1009	14.92	-0.4489	-0.4431	1.29
7	0.0859	0.0862	-0.35	0.0872	0.0887	-1.72	-0.3593	-0.3607	-0.39
8	0.0515	0.0524	-1.74	0.0886	0.0901	-1.69	-0.3177	-0.3099	2.46
9	0.0360	0.0376	-4.44	0.1267	0.1281	-1.10	-0.3685	-0.3703	-0.49

The examined cubes exhibited undersized height and oversized x-, and y-dimensions. The measured deformations were relatively small when compared to the overall dimensions of the cubes. The simulated results suggested that the distortion in all manufactured specimens have increasing tendency within the z-direction. The lowest distortions in bottom parts of the cubes are probably caused by the strong constrain of the material to the building platform, while the upper layers undergo substantially more liberated material

flow resulting in higher deformations [249]. The distribution of total distortions in Block 2 is demonstrated in Figure 64.

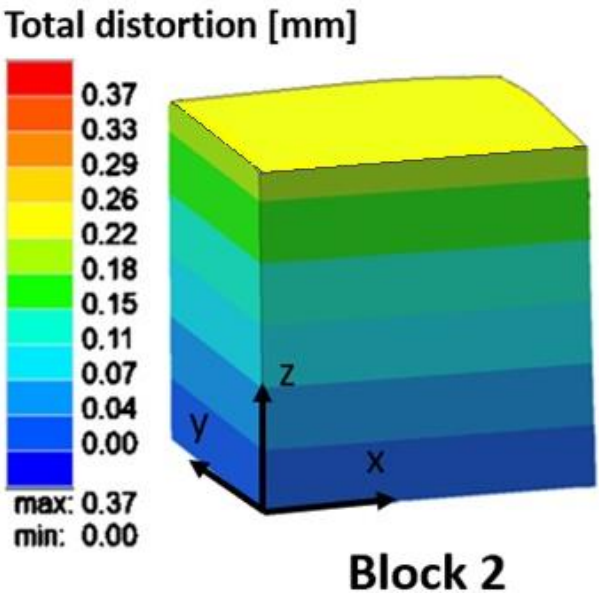

Figure 64 Distribution of total distortions in Block 2

Notably, it was observed that the distortions of the fabricated cubes correlated with the position of the cubes on the building plate. This correlation can be attributed to the varying thermal gradients within the baseplate and their proximity to the door of the building chamber. The effects of the building position of the cubes on the distortions, geometrical dimensions, and tolerances are further explained in Section 4.3.1.

5.3.2. Deformations in treated specimens

Figure 65 demonstrates LPBF-manufactured cubes attached to the base plate after the FSSP treatment.

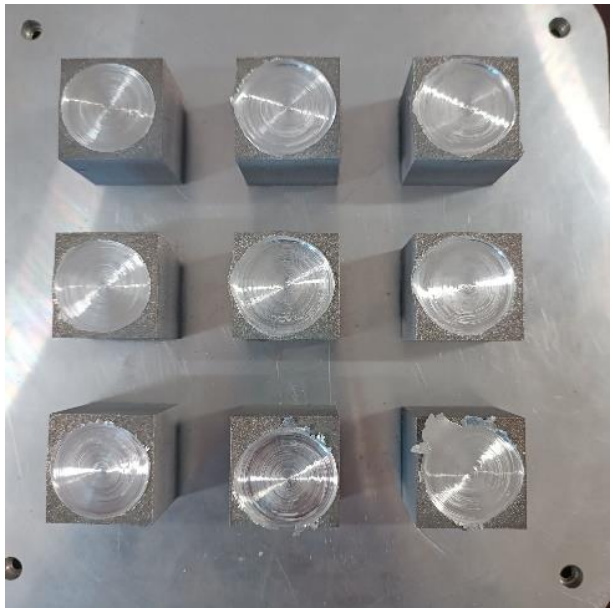

Figure 65 LPBF-manufactured cubes after the FSSP treatment

Simulated and experimental dimensions of the processed plane are listed in Table 26. The low relative error suggests good agreement between the simulated and experimental results. Therefore, the numerical model can be considered validated.

Table 26 Comparison between experimental and simulated dimensions of processed plane and calculated relative error.

Block	**Processed state**											
	Experimental						**Simulated**					
	Lx_1	**Lx_2**	**Lx_3**	**Ly_1**	**Ly_2**	**Ly_3**	**Lx_1**	**Lx_2**	**Lx_3**	**Ly_1**	**Ly_2**	**Ly_3**
	[mm]											
1	35.02	35.20	35.10	35.04	35.08	35.03	35.00	35.20	35.10	35.05	35.05	35.04
2	35.12	35.22	35.08	35.24	35.30	35.12	35.20	35.26	35.18	35.08	35.24	35.10
3	35.22	35.30	35.10	35.02	35.10	35.10	35.22	35.30	35.16	35.12	35.05	35.07
4	35.06	36.55	35.10	35.08	35.70	35.30	35.05	36.42	35.08	35.10	35.84	35.14
5	35.08	36.40	35.22	35.08	36.08	35.20	35.07	36.51	35.15	35.10	36.03	35.17
6	34.70	36.08	35.01	35.02	35.50	35.18	35.09	36.04	35.05	35.05	35.94	36.09
7	35.80	36.82	35.32	35.20	36.16	35.22	35.14	36.75	35.24	35.20	36.15	35.22
8	35.06	37.02	35.12	35.20	36.08	35.10	35.18	37.15	35.12	35.22	36.54	35.18
9	35.11	35.70	35.10	35.22	35.06	35.18	35.20	35.56	35.14	35.12	35.40	35.16

	Relative error [%]					
	Lx1	**Lx2**	**Lx3**	**Ly1**	**Ly2**	**Ly3**
1	0.057	0.000	0.000	-0.029	0.086	-0.029
2	-0.228	-0.114	-0.285	0.454	0.170	0.057
3	0.000	0.000	-0.171	-0.286	0.142	0.085
4	0.029	0.356	0.057	-0.057	-0.392	0.453
5	0.029	-0.302	0.199	-0.057	0.139	0.085
6	-1.124	0.111	-0.114	-0.086	-1.239	-2.587
7	1.844	0.190	0.227	0.000	0.028	0.000
8	-0.342	-0.351	0.000	-0.057	-1.275	-0.228

9	-0.256	0.392	-0.114	0.284	-0.970	0.057

Remarkably, a consistent trend in incremental displacements along the z-direction persists in the global distortions observed in the full-sized specimens. This phenomenon aligns with the patterns identified in specimens in their as-built state. This uniform distribution of displacements transcends variations in processing parameters, as depicted in Figure 66 across all processed specimens.

Consequently, it can be determined that deformations primarily affect the upper segment of the LPBF-manufactured and FSSP-treated specimens, while the lower sections exhibit commendable geometrical accuracy. Thus, a comprehensive examination of both LPBF-induced and FSSP-induced distortions in the upper portions of the specimens becomes imperative. Subsequently, potential calibrations should be explored to mitigate the risk of excessive deformations that could potentially impede a series of industrial applications [250].

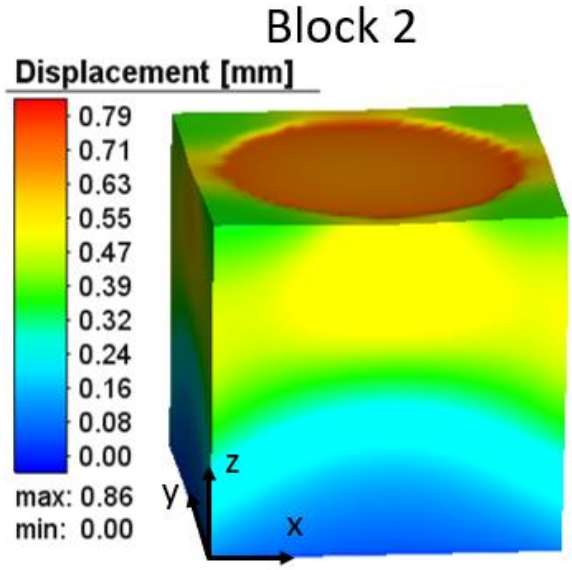

Figure 66 Distribution of displacements in FSSP-treated specimen

It is noteworthy that the dimensions of the treated planes, specifically those measured along the edges (Lx_1, Lx_3, Ly_1, Ly_3), exhibit minimal deviation from the corresponding dimensions of the specimens in their as-built state. In contrast, significant variation is observed in the dimensions of the machined planes measured at the midpoint of the sides' lengths (Lx_2, Ly_2), diverging notably from the dimensions of the cubes in their original, as-built state. This discrepancy strongly suggests an outward material flow in these particular regions, leading to the resultant distortions, as illustrated in Figure 67 [251]. It is pertinent to note that these

distortions were consistently observed across all processed specimens; however, the overall extent of distortion varied in accordance with the specific process parameters applied.

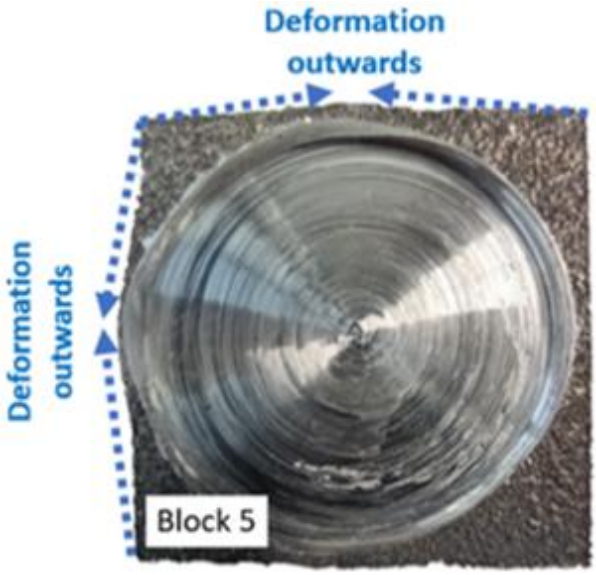

Figure 67 Outwards-directed deformation of processed plane in Block 5

Interestingly, an observation of particular note reveals that in specimens subjected to extended dwell times and higher rotational speeds (blocks 4, 5, 7, 8), there was a discernible increase in the outward-directed distortions of the processed planes. These distortions became more pronounced, to the extent that they were readily visible to the naked eye, as depicted in Figure 68.

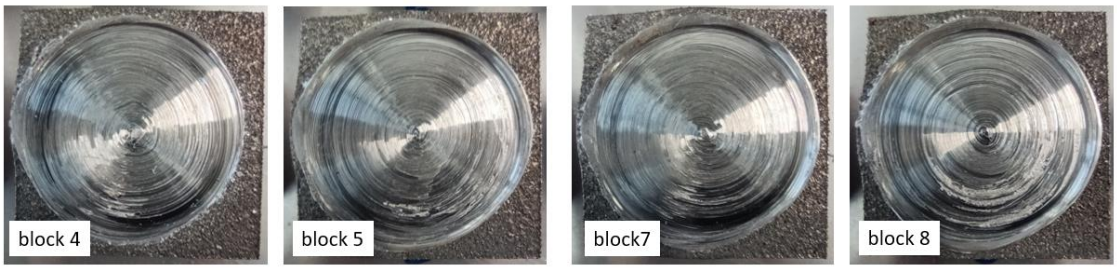

Figure 68 Deformation of processed plane in specimens processed with the combination of longer dwell times and higher rotational speed

In contrast, specimens processed with shorter dwell times and lower rotational speeds (blocks 1, 2, 9) demonstrate lower distortions of the processed plane, however with substantial amount of flesh (Figure 69).

Figure 69 Deformation and flash in specimens processed with the combination of short dwell time and low rotational speed

The observed phenomenon can be explained by considering the broader thermally affected zones evident in specimens subjected to a combination of elevated rotational speed and prolonged dwell times. In such instances, the softened material within these zones facilitates substantial material flow, as documented in previous studies [252]. Conversely, employing lower rotational speeds along with shorter dwell times leads to markedly narrower thermally affected zones. In this scenario, the softened material remains encapsulated by the unaffected, harder material, acting as a constraint against continued material flow and consequent distortion. Consequently, the softened material undergoes an upward displacement towards the peripheries and outer regions, wherein it solidifies into a flash-like structure, as illustrated in previous research findings [253]. The validity of this assertion is reinforced by numerical results, as depicted in Figure 70.

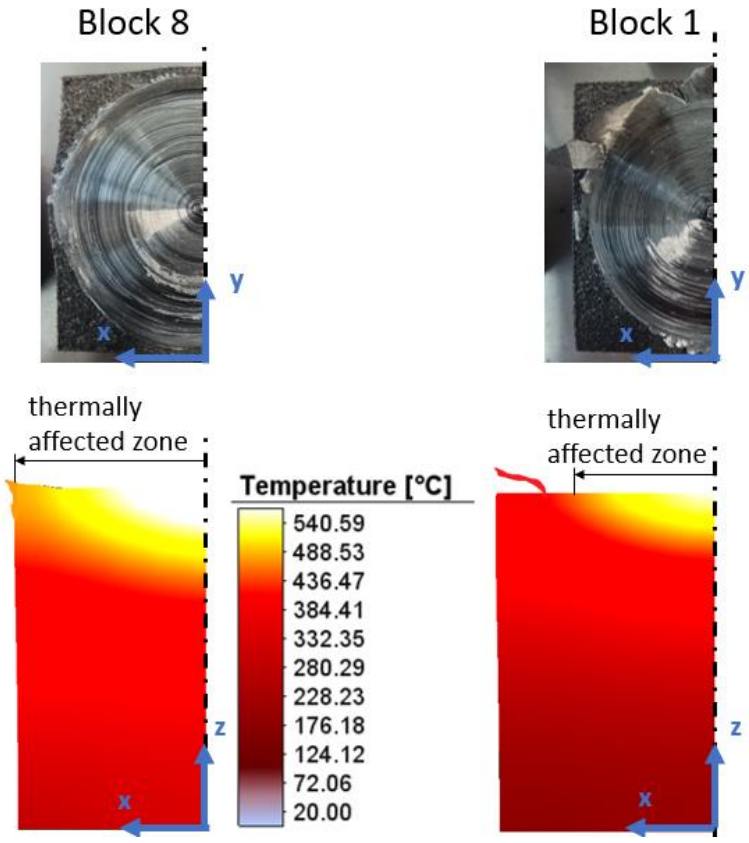

Figure 70 Simulated thermally affected zones and deformation of the processed planes in blocks 8 and 1

Both simulated and experimental findings consistently reveal a discernible degree of symmetry in the displacements along both the x- and y-directions. Notably, the simulated results exhibit a heightened level of symmetry compared to their experimental counterparts. This discrepancy implies that the marginal asymmetry observed in the distortions of experimental specimens is likely attributable to the off-centered positioning of the processing tool rather than an asymmetric material flow. This inference gains additional credence from the relatively uniform distribution of distortions oriented along the x- and y-axes within their respective directions, a phenomenon consistently observed across all simulated processed specimens (refer to Figure 71).

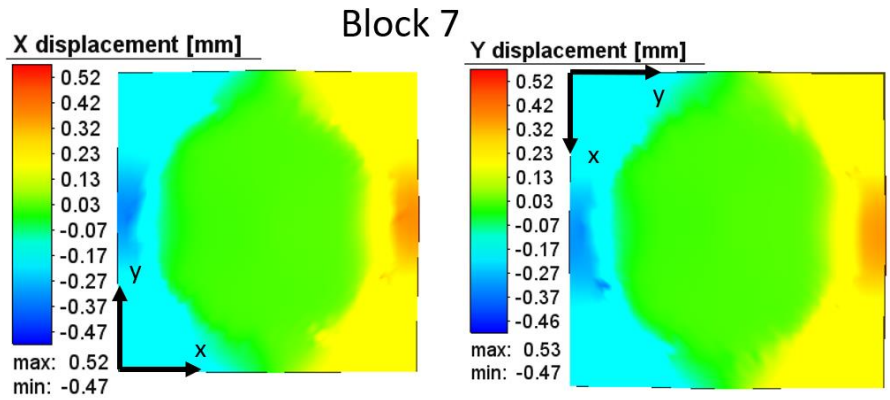

Figure 71 Simulated distribution of x-, and y-displacement in the processed plane of block 7

The FSSP-induced distortions of the upper faces of the processed cubes, considering the pre-deformed state resulting from the manufacturing process, are further presented in Table 27.

Table 27 Experimental values of maximal distortions of processed planes in x-, y-, and z-directions, induced by FSSP treatment

	Cube								
	1	**2**	**3**	**4**	**5**	**6**	**7**	**8**	**9**
Dx [mm]	0.1539	0.2042	0.2622	1.4156	1.3262	0.9953	1.7341	1.9685	0.6640
Dy [mm]	0.0197	0.2309	0.0532	0.5919	0.9752	0.3814	1.0728	0.9914	-0.0667
Dz [mm]	-0.06	-0.15	-0.21	-0.08	-0. 21	-0.28	-0.06	-0.1	-0.05

Through an examination of the distortions induced by FSSP in the z-direction of the cubes, it was noted that, despite a consistent plunge depth of 0.8 mm during processing across all specimens, the resulting distortions exhibited considerable variability. The distribution of z-displacement within the processed plane remained consistent across all specimens, with the most pronounced distortions observed in the central region where the processing tool was initially positioned. Notably, relatively high distortions were also evident in peripheral areas at the midpoints of the cubes' edges, as illustrated in Figure 72. This observation implies an outward and upward orientation of material flow in these specific regions.

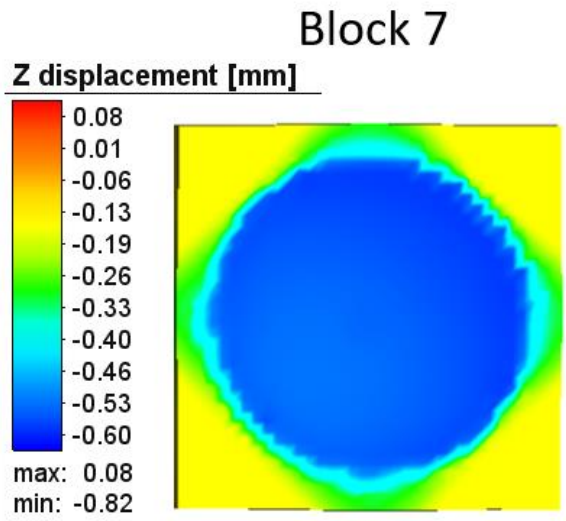

Figure 72 Distribution of the z-displacement in processed plane of the Block 7

It is noteworthy that the distortions observed in all analysed cubes were consistently lower than the applied plunge depth. Moreover, distortions induced by the FSSP method in the z-direction were generally inferior to those caused by LPBF manufacturing process. Consequently, it can be inferred that the utilization of a pinless tool yields commendable geometrical accuracy in the z-dimension of the processed specimen. The FSSP technique, particularly when coupled with a pinless tool, emerges as an appealing configuration for applications demanding precise geometrical accuracy in the z-direction.

However, it is essential to highlight that the ANOVA analysis refutes the statistically significant effects of both rotational speed and dwell time on the resulting distortion in the z-direction. Nevertheless, it should be acknowledged that the response surface methodology employed in this study may not have adequately captured the dynamic processes that ensue during material processing [254].

In contrast, our statistical analysis has unequivocally established the impact of dwell time on the deformation of the x-dimension within the processed plane, as indicated by a statistically significant P-value. Conversely, the effect of rotational speed was determined to be statistically insignificant, with a P-value of 0.258. On the other hand, the deformation of the y-dimension within the processed plane exhibited sensitivity to both process parameters—dwell time (P-value = 0.011) and rotational speed (P-value = 0.031). These discerned variations in influencing effects, coupled with the presence of slightly asymmetric deformations, can be ascribed to the off-centered position of the processing tool rather than inherent asymmetries in material flow. The Pareto charts, visually representing the statistical significance of dwell time and rotational

speed as FSSP parameters in influencing deformations along the x- and y-directions in processed planes, are presented in Figure 73.

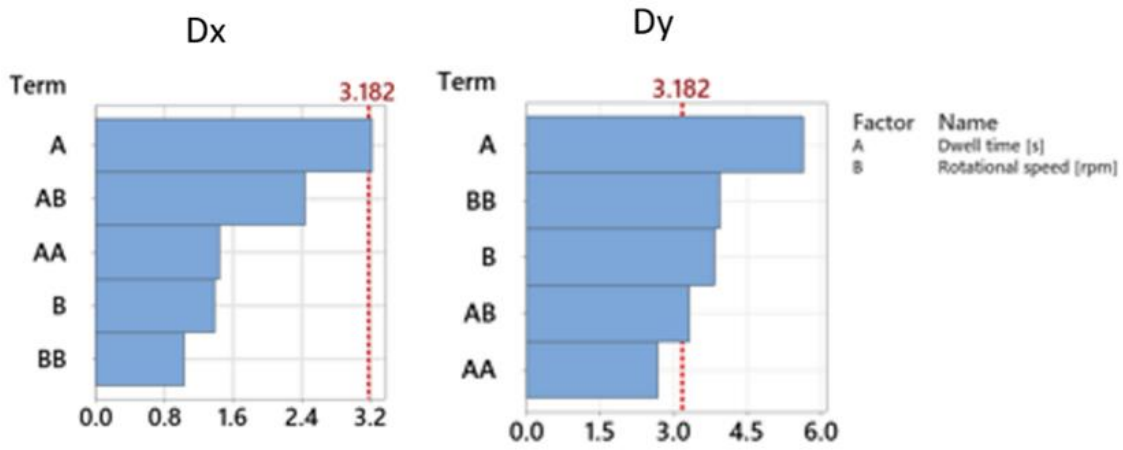

Figure 73 Pareto charts determining the significance of the effects of dwell time and rotational speed on FSSP-induced distortion in x- and y-direction

The statistical analysis conducted in this study revealed a quasi-direct proportionality between dwell time and deformation in the x-dimension of the processed plane, as illustrated in Figure 74a. Additionally, Figure 74b demonstrates a quasi-direct proportionality between dwell time and rotational speed (Figure 74c), and the resulting deformation in the y-dimension of the processed plane. Notably, an increase in dwell time from 5 to 7.5 seconds led to a significant augmentation in distortions in both analyzed directions. Subsequent increments in dwell time to approximately 9 seconds resulted in only a marginal increase in distortions compared to the 7.5-second dwell time. However, extending the dwell time to 10 seconds led to a slight reduction in distortions, although the distortions remained higher than those observed in specimens processed for 7.5 seconds.

A similar trend was observed for the influence of rotational speed on distortion in the y-direction. Specifically, an increase in rotational speed from 1000 to 1500 rpm resulted in a significant augmentation of distortions, with the maximum distortion anticipated in specimens processed at approximately 1630 rpm. Further elevating the rotational speed to 2000 rpm produced a decrease in distortion, with the value slightly lower than that in specimens processed at 1500 rpm.

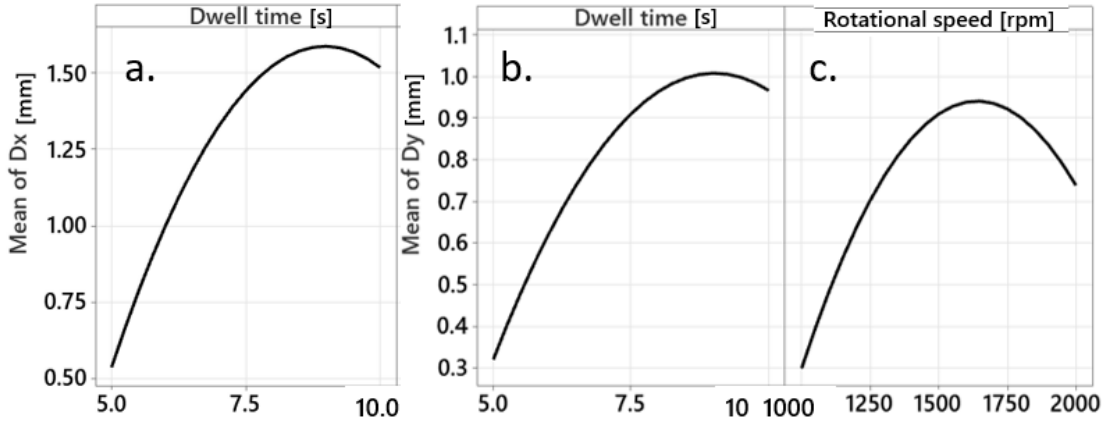

Figure 74 Main effects plots describing the effects of a.) dwell time on Dx, b.) dwell time on Dy, c.) rotational speed on Dy

Finally, Figure 75, demonstrating the contour plots, summarizes the interactions of FSSP processing parameters (dwell time and rotational speed) in their effects on distortions in x-, y-, and z-direction.

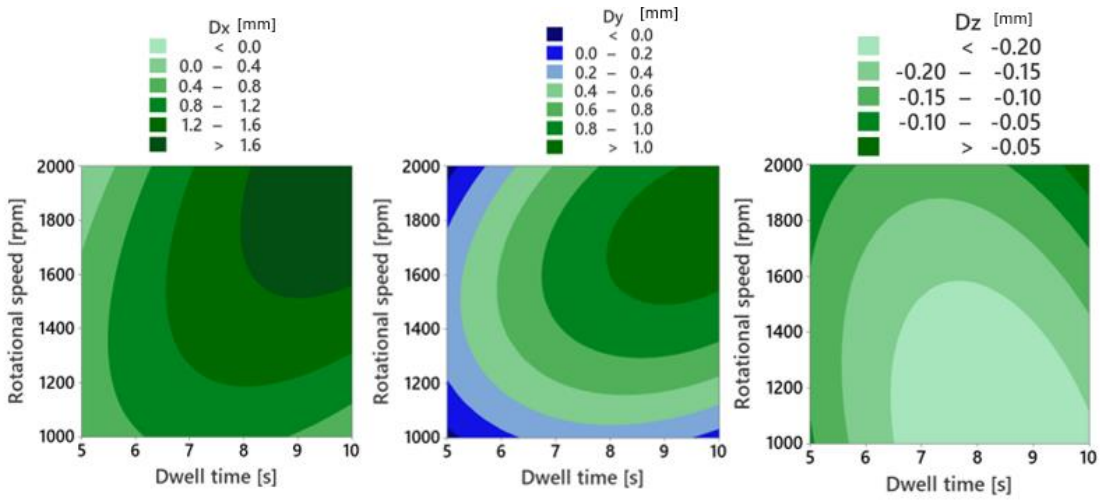

Figure 75 Contour plots describing the effects of interaction of rotational speed and dwell time on distortions of the processed planes in x-, y-., and z-direction

5.3.3. Microstructure and microhardness in FSSP-treated specimens

Figure 76 demonstrates the microstructurally diverse zones in FSSP-treated specimen S1.

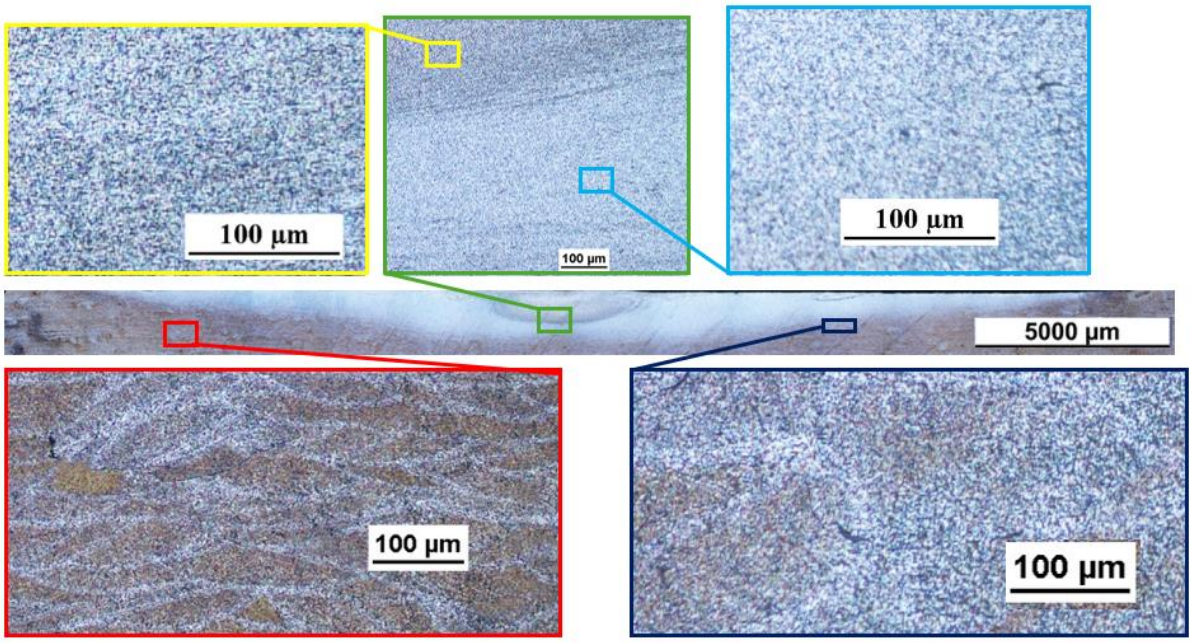

Figure 76 Microstructurally diverse zones in FSSP-treated specimen S1

The analysis presented in Figure 76 reveals distinct zones within FSSP-treated specimens, each exhibiting unique characteristics. These zones are identified as the stir zone (SZ), thermo-mechanically affected zone (TMAZ), heat-affected zone (HAZ), and base material (BM). It is crucial no note that the depth of the described zones highly varied amongst the analysed specimens and it depended on the adopted processing parameters.

Notably, the BM and HAZ zones retains the distinctive "fish-scaled" structure, featuring half-cylindrical melt pools, indicative of typical LPBF manufacturing. As it is further described in Section 2.2.2., the BM in the transverse section contains a heterogeneous microstructure with columnar dendrites characterized by epitaxial grain growth.

In stark contrast, the SZ and TMAZ exhibit a significantly fine-grained and homogenized microstructure. While the SZ contains predominantly fine equiaxed grains, several residual elongated grains can be observed within TMAZ (Figure 77). At the boundaries of the SZ and TMAZ, a series of banding structures resembling "onion rings" were identified (Figure 76).

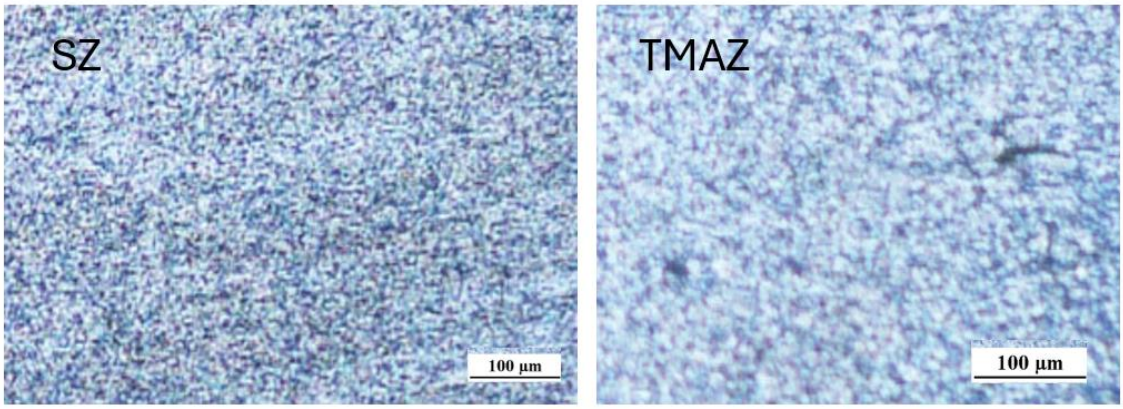

Figure 77 Comparison of microstructure in SZ and TMAZ

A detailed comparison between the BM and TMAZ zones reveals a notable densification effect in the latter. Figure 78a depicts the BM with observable pores and lack-of-fusions, while Figure 78b illustrates the TMAZ with a markedly lower occurrence of lack-of-fusions and virtually no pores.

This densification phenomenon is consistent with findings presented by [255], supporting the assertion that FSSP is more effective in suppressing pores compared to HIP treatment.

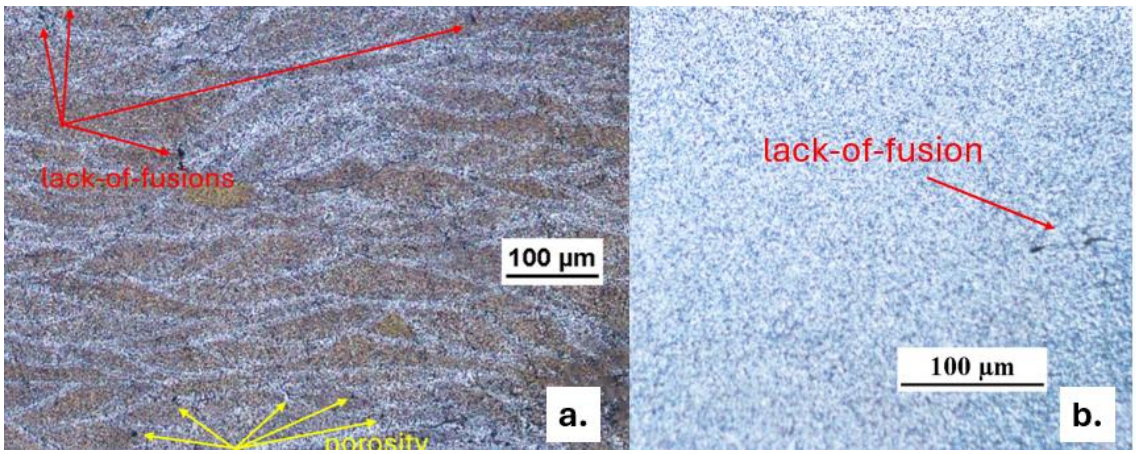

Figure 78 Comparison of microstructure in a.) BM and b.) TMAZ in specimen S1

The HAZ serves as the transitional interface between the BM and the TMAZ. Within this region, the distinctive fish-scaled microstructure remains perceptible, albeit subjected to structural changes induced by the applied heat. Optical microscopy alone may face challenges in unequivocally delineating the boundaries of the HAZ and BM. However, existing literature points towards the discernible development of a Si-rich eutectic morphology, a phenomenon substantiated by variations in microhardness [256].

Detailed insights into the variations in TMAZ depths, determined under diverse FSSP process parameters, are presented in Table 28, showcasing the maximal widths observed across the specimens.

Table 28 Maximal widths of TMAZ in specimens processed with different process parameters

Specimen								
S1	**S2**	**S3**	**S4**	**S5**	**S6**	**S7**	**S8**	**S9**
Maximum TMAZ depth [mm]								
1.963	1.193	1.058	2.661	1.827	0.918	3.292	2.524	0.914

It was observed that the TMAZ depths were significantly affected by the FSSP processing parameters. The most shallow TMAZ was identified in specimen S9, processed with the lowest rotational speed for the shortest dwell time. As demonstrated in Figure 79, the gradual increase of dwell time resulted in the widening of the TMAZ, even if the rotational speed was kept constant on 1000 rpm.

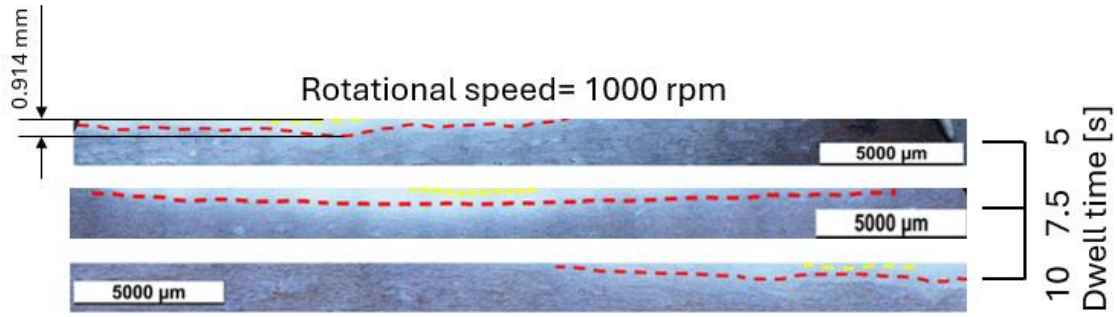

Figure 79 Shapes and dimensions of SZ and TMAZ in specimens processed with 1000 rpm for different dwell times

Similarly, the increase of the rotational speed to 1500 rpm has led to an increase in the TMAZ depth. The most shallow TMAZ depth out of all specimens manufactured with the rotational speed of 1500 rpm was identified in the specimen processed with a dwell time of 5 seconds. Notably, while the shape of TMAZ in specimen processed with dwell time of 5 seconds was relatively regular and half-cylindrical, the shapes of TMAZs in specimens processed with longer dwell times were irregular, with prominent deepenings alongside the lateral SZ boundaries. Similarly, the specimens processed with longer dwell times were characterized by more pronounced, well visible SZs (Figure 80).

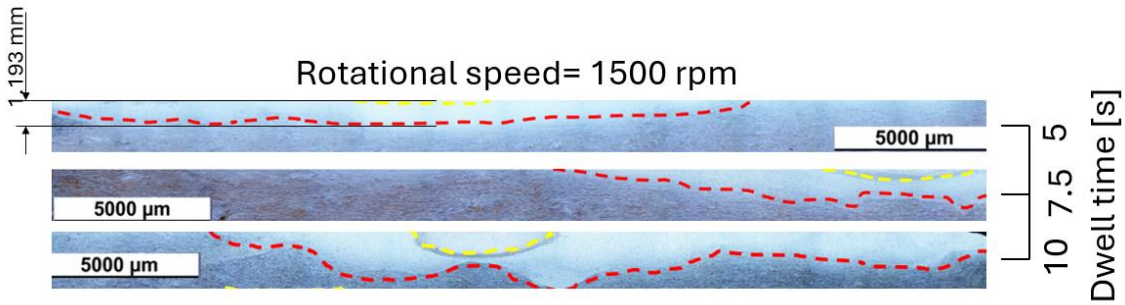

Figure 80 Shapes and dimensions of SZ and TMAZ in specimens processed with 1500 rpm for different dwell times

Notably, further increase of the rotational speed has caused yet another deepening of the TMAZ (Figure 81). The TMAZ depth increased gradually with the increase of the dwell time. Similarly, as it was observed in specimens processed with rotational speed of 1500 rpm combined with higher dwell time, the shapes of TMAZs were relatively irregular. While in specimens processed for 5 and 10 seconds, the prominently deepened areas of TMAZs were located alongside the lateral SZs boundaries, both TMAZ and SZ shapes of specimen processed with rotational speed of 200 rpm and dwell time of 7.5 seconds were significantly irregular. The SZs in all three specimens were well-pronounced and easily identifiable.

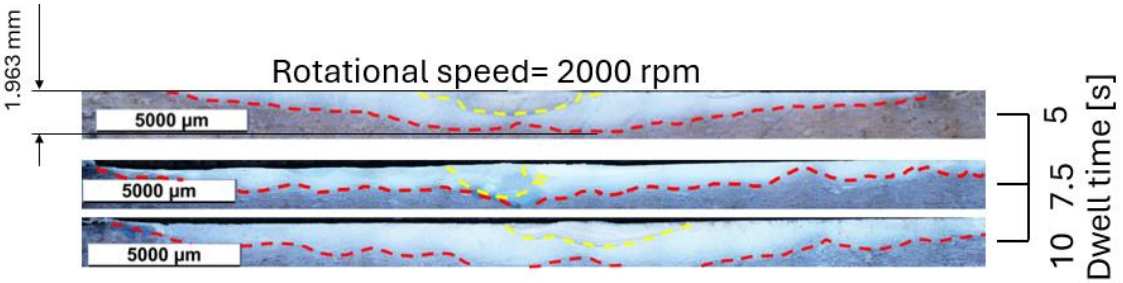

Figure 81 Shapes and dimensions of SZ and TMAZ in specimens processed with 2000 rpm for different dwell times

Significantly, the morphological characteristics of the TMAZs exhibited distinct patterns among the examined specimens, denoted as S1, S2, S4, S7, and S8, where the TMAZ shapes were notably quasi-symmetric and half-cylindrical. In contrast, specimens S3, S5, S6, and S9 displayed TMAZ shapes characterized by pronounced irregularities. It is important to highlight that these irregularities did not result from irregular material flow but rather stemmed from the off-centred position of the processing tool. This assertion finds support in the spatial distribution of TMAZs within the processed specimens.

Statistical analysis has substantiated the noteworthy impact of both dwell time (with a corresponding P-value of 0.011) and rotational speed (with a corresponding P-value of 0.002) on the maximal depth of the TMAZ, as illustrated in Figure 82. Notably, the influence of

rotational speed on the width of the TMAZ surpasses that of dwell time, signifying a more pronounced and statistically significant effect.

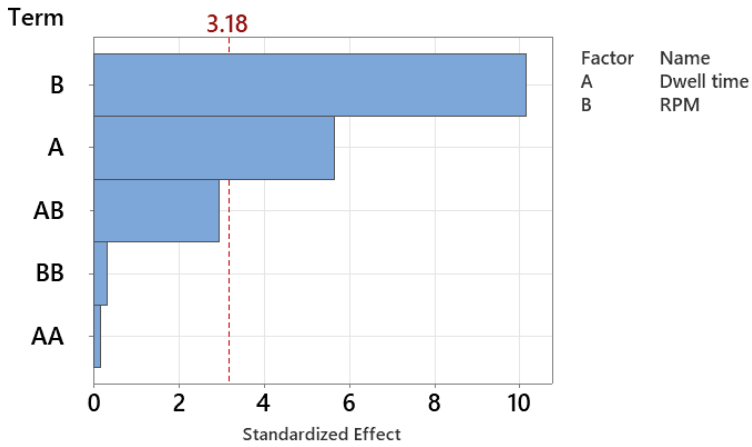

Figure 82 Pareto charts determining the significance of the effects of dwell time and rotational speed on the maximal depth of TMAZ

The correlation between dwell time and rotational speed with the maximal depth of the TMAZ exhibited a quasi-linear trend, indicating a direct proportionality between the two factors, as illustrated in Figure 83. Subsequently, it was established that employing the minimum dwell time (5 seconds) in conjunction with the lowest rotational speed (1000 rpm) yielded the most superficial TMAZ. Notably, elevating both input parameters led to a gradual expansion of the TMAZ width.

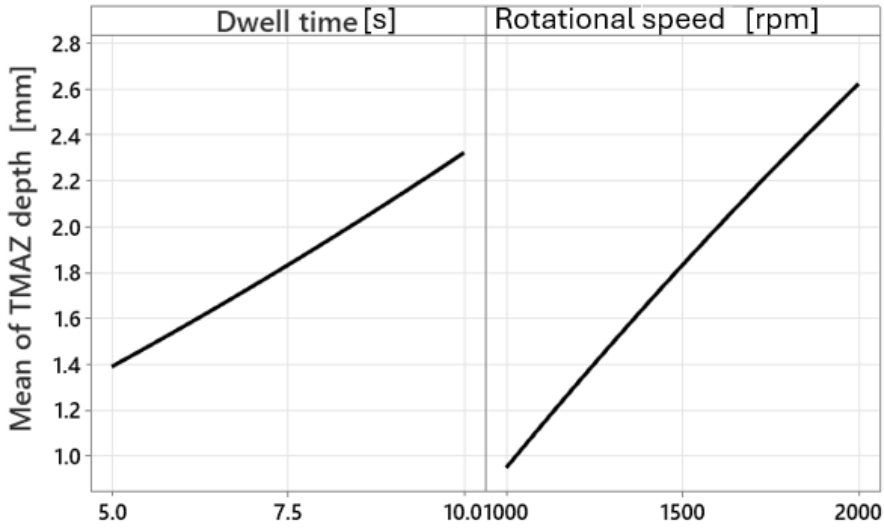

Figure 83 Main effects plots describing the effects of dwell time and rotational speed on TMAZ depth

Figure 84 determined the effects of the interactions of various levels of dwell time and rotational speed as the FSSP processing parameters on the resulting dimensions of TMAZ depths.

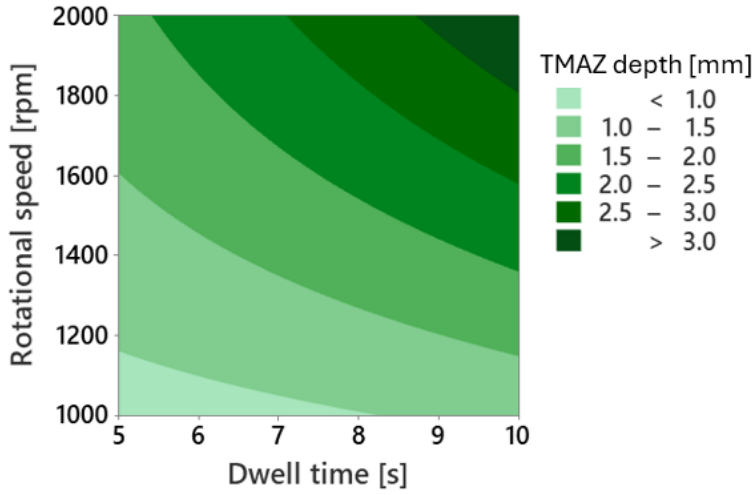

Figure 84 Contour plots describing the effects of the interaction of rotational speed and dwell time on the resulting TMAZ depth

It is reasonable to anticipate that the heterogeneous microstructure is inherently evidenced by an uneven distribution of hardness within the region treated by FSSP. As illustrated in Figure 85, portraying the outcomes of microhardness assessments across the cross-section of specimen S1, the hardness in the HAZ is notably inferior to that of the BM and diminishes with proximity to the tool probe surface. Although microhardness in the SZ and TMAZ demonstrates practical interchangeability, it is evident that the material within the HAZ does not undergo a commensurate degree of softening.

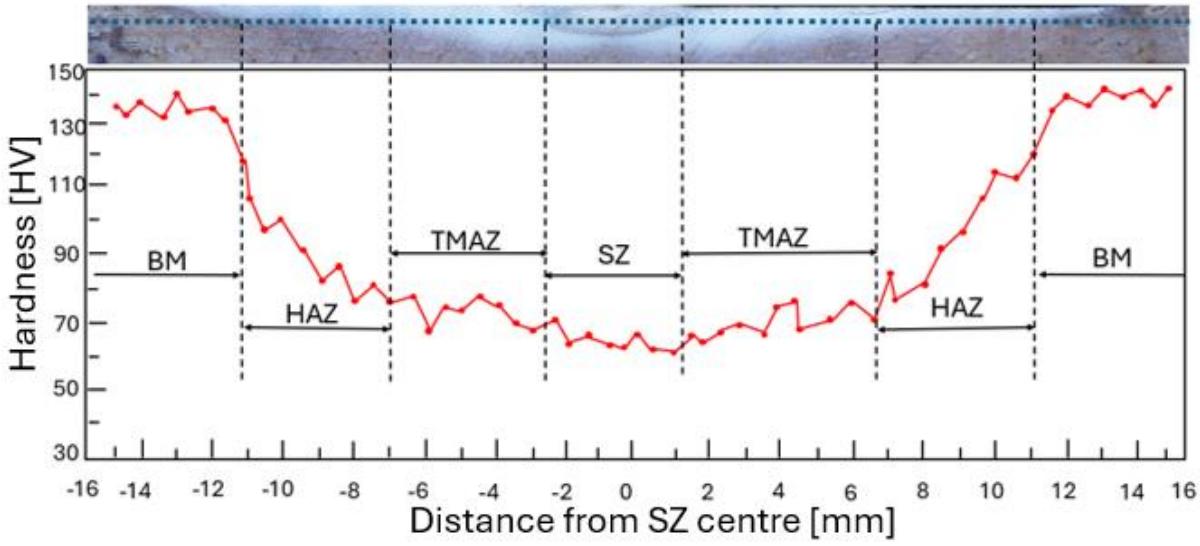

Figure 85 Microhardness in specimen S1 after FSSP treatment

The localized modification of mechanical properties within the TMAZs of LPBF-manufactured components treated by FSSP technology has significant implications for a variety of industrial applications. This technique facilitates the creation of regions with distinct

mechanical characteristics, such as brittleness and ductility, within a single component. Such capability is particularly relevant in fields like healthcare and aerospace, where customized material properties can greatly enhance the functionality and performance of components. Furthermore, the FSSP technology's ability to tailor mechanical properties extends the industrial relevance of LPBF, which, on its own, allows for the customization of component shapes with virtually no limitations. This attribute underscores the versatility and transformative potential of this novel method of treatment in advanced manufacturing sectors.

5.3.4. Desirability analysis and process optimisation

Table 29 lists the results of the optimisation process, containing the optimized FSSP process parameters and predicted values of TMAZ widths and Dx, Dy, and Dz distortions. It is important to highlight that the optimization process focused on maximizing the TMAZ depth and Dz values, while minimizing the Dx and Dy parameters. The input objectives of the optimization were carefully chosen to enhance the overall performance. The composite desirability of the optimized process parameters achieved sufficient value of 79%.

Table 29 Results of the optimization process

Dwell time [s]	**Rotational speed** [rpm]	**Dz fit** [mm]	**Dy fit** [mm]	**Dx fit** [mm]	**TMAZ fit [mm]**	**Composite desirability**
5.16	2000	-0.06	0.08	0.02	1.887	0.79

The anticipated deformation resulting from the FSSP treatment, employing the optimized process parameters, is notably minimal and comparable to distortions induced by the LPBF manufacturing process. Simultaneously, the predicted maximum depth of TMAZ, serving as an effective measure of the processing depth, reached 1.887 millimetres for specimens processed with the optimized parameters. In contrast, techniques like shot peening typically yield effective depths ranging between 0.1 and 0.2 mm for LPBF-manufactured AlSi10Mg alloy [257, 258]. This observation underscores the superior effectiveness of FSSP treatment.

The achievable low level of deformation suggests the feasibility of FSSP as a treatment technique, even in scenarios demanding high precision and excellent geometrical accuracy.

Moreover, the potential of FSSP treatment lies in its capacity for significant depth enhancement through adjustments in dwell time and rotational speed. However, such enhancements would correlate with increased deformations in and around the processed surface. Consequently, striking a satisfactory balance between the effective processing depth

and induced deformations becomes imperative. When applying FSSP treatment, the selection of processing parameters should be approached individually, guided by informed decisions supported by a profound understanding of the treatment process and/or numerical simulations.

It is noteworthy that in situations requiring a substantial effective treatment depth, mitigating undesired deformations can be achieved through initial shape compensation. Recognizing that high deformations tend to concentrate around the top surface of LPBF-manufactured specimens, with significantly lower deformations in areas proximal to the base plate, the positioning of the specimen during the build phase becomes crucial. Strategically placing the FSSP-processed plane, experiencing the highest FSSP-induced deformation, in contact with the base plate during the building phase is a compelling consideration, given that LPBF-induced deformations in this area are negligible. This insight offers an avenue to optimize specimen positioning for improved outcomes during the FSSP treatment process.

6. Numerical modelling of friction stir spot processing

In light of the findings explained in Chapter 5, the pinless configuration of Friction Stir Spot Processing (FSSP) can be perceived as an efficacious post-process treatment for components fabricated using Laser Powder Bed Fusion (LPBF) technology. This technique represents a promising choice for applications such as microstructure homogenization and porosity mitigation. However, given the intricate nature of this treatment modality, a comprehensive understanding of how processing parameters influence the effective depth of treatment and potential deformations remains elusive. Consequently, a bespoke evaluation of processing parameters is necessary, tailored to the specific requirements of effective depth and permissible deformation levels.

Presently, numerical modelling is increasingly recognized as a pivotal tool in guiding parameter selection for both LPBF and FSSP processes. Nonetheless, FSSP's intrinsic complexity, characterized by significant strains and plastic deformations, poses formidable challenges to traditional Finite Element Method (FEM) formulations. The use of conventional numerical models in simulating FSSP treatments frequently encounters severe mesh distortions, leading to issues with convergence behaviour. To overcome these limitations, the numerical model introduced in this chapter adopts an innovative approach, utilizing the Coupled Eulerian-Lagrangian (CEL) formulation.

The validation of the developed numerical model confirms the efficacy of the CEL approach, in conjunction with the proposed physical descriptions, for accurately simulating material flow. This capability enables precise predictions of Thermo-Mechanically Affected Zone (TMAZ) dimensions, measured distortions, and flash formation. Additionally, the model demonstrates a commendable ability to capture the suppression of lack-of-fusion defects, underscoring its potential as a robust tool in FSSP treatment simulations.

6.1. Experimental set-up

6.1.1. Sample manufacturing

Nine specimens, each featuring 35 mm long edges, were fabricated using AlSi10Mg powder via Laser Powder Bed Fusion (LPBF). Comprehensive details regarding the fabrication

process of these samples are provided in Section 5.1.1. Nevertheless, this chapter focuses specifically on the examination and analysis of cubes 1, 2, and 3, as illustrated in Figure 86.

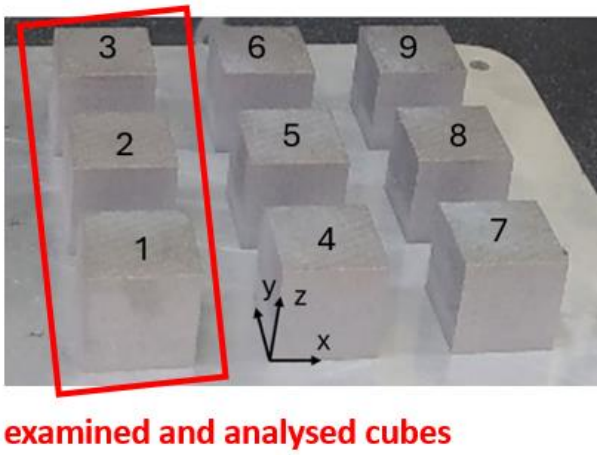

Figure 86 Manufactured and examined cubes

6.1.2. Sample processing

In this chapter, the study focuses on the treatment of cubes 1, 2, and 3 utilizing Friction Stir Spot Processing (FSSP) with a pinless tool, as illustrated in Figure 87.

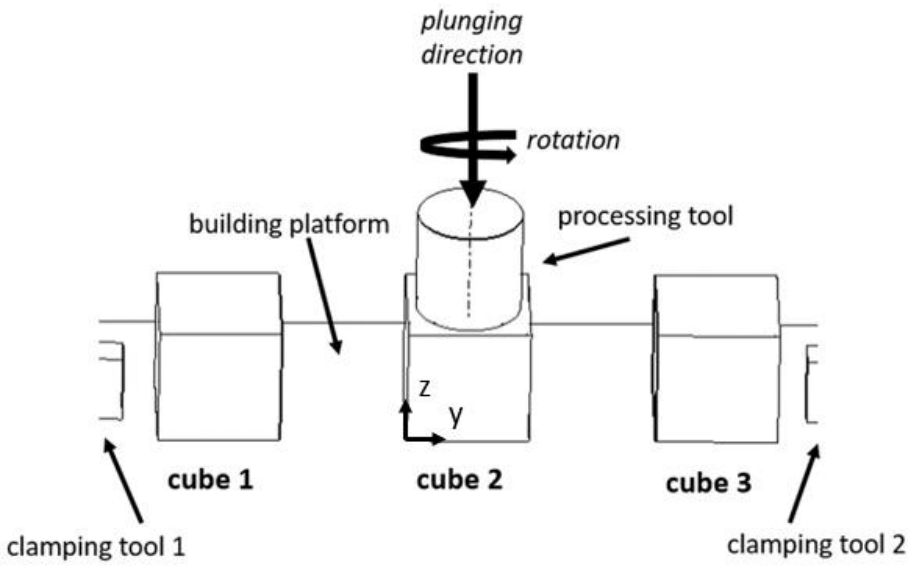

Figure 87 FSSP treatment of analysed cubes

The methodology of the applied treatment is detailed in Section 5.1.2. of this thesis. FSSP processing parameters are listed in Table 30.

Table 30 FSSP processing parameters

	Cube 1	Cube 2	Cube 3
Rotational speed [rpm]	2000	1500	1000

Dwell time [s]	5	5	10

6.1.3. Deformation assessment

A deformation assessment of the analysed cubes in their as-built and processed state was performed as described in Section 5.1.3. of this thesis.

6.1.4. Analysis of TMAZ dimensions

The maximal depths of the Thermo-Mechanically Affected Zone (TMAZ) in LPBF-manufactured cubic samples, post-FSSP treatment, were quantitatively assessed. This assessment was conducted through optical analysis of the transverse sections of the processed cubes. Specifically, the maximal TMAZ depth was determined by measuring the greatest z-dimension of the TMAZ in each sample, utilizing pixel count as the metric for measurement. Further details regarding the microscopic preparation of these samples are elaborated in Section 5.1.4 of this study.

6.2. Numerical models

6.2.1. Numerical model of the LPBF-production phase

In this study, we employed a coupled thermo-mechanical numerical model, characterized by a mesoscale approach as described in Chapter 3, to simulate the LPBF manufacturing process of AlSi10Mg alloy cubes. Given the substantial computational demands of this model, the simulation was restricted to the fabrication of three specific cubes (labelled 1, 2, and 3, as illustrated in Figure 88). It is important to note that, in these simulations, the thermo-mechanical influences exerted by the presence of additional cubes on the base plate were not considered. This simplification was necessary to maintain computational feasibility while still providing meaningful insights into the fundamental aspects of the LPBF process for AlSi10Mg.

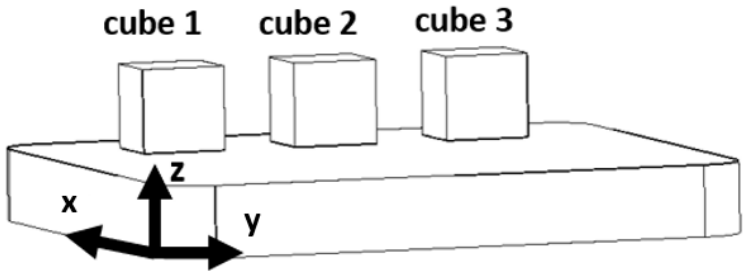

Figure 88 Simulated configuration of the LPBF-manufactured cubes on the base plate

The simulation was conducted using the ABAQUS/Explicit solver. Cubical specimens were discretized into a mesh of cubic elements, with each element's edge length corresponding to the layer thickness utilized in the experimental campaign. Conversely, the mesh for the base plate was designed to be considerably coarser, as illustrated in Figure 89.

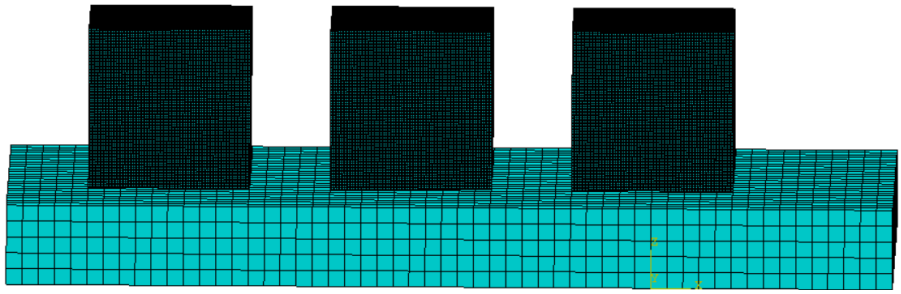

Figure 89 Specimens and base plate discretized into meshing elements

6.2.2. Numerical model of the FSSP treatment

The present numerical model utilizes the Coupled Eulerian–Lagrangian (CEL) methodology, integrating both Eulerian and Lagrangian frameworks within the simulation. In this model, the Eulerian domain is designated for the workpiece, whereas the Lagrangian elements represent the base plate and the blank holder. Furthermore, a 2-millimetre void layer has been incorporated to facilitate the simulation of free material flow, thereby enabling the prediction of phenomena such as flash formation.

The full model was governed by mass, momentum and energy conservation equations (34, 35, 36).

$$\frac{\partial \rho}{\partial t} + \nabla.(\rho v) = 0 \qquad (34)$$

$$\rho\left(\frac{\partial v}{\partial t} + \nabla.(v \otimes \mathrm{v})\right) = \nabla.\sigma + \rho g \qquad (35)$$

$$\rho C_p\left(\frac{\partial T}{\partial t} + v.\nabla T\right) = \nabla.(k\nabla T) + \nabla.(\sigma.v) + \dot{Q} \qquad (36)$$

The Eulerian-based equations (34-36) can be written in their general conservation form (37):

$$\frac{\partial \phi}{\partial t} + \nabla.\Phi = S \qquad (37)$$

Where the Φ represents the flux function and the S represents the source term.

Notably, the term (35) is distinctly fivided through a specialized splitting algorithm into two components: the Lagrangian step, which encompasses the source term, and the Eulerian step, which is characterized by the convective term. The outcomes of this division are systematically presented: the Lagrangian step is detailed in equation (38), while the Eulerian step is described in equation (39).

$$\frac{\partial \phi}{\partial t} = S \qquad (38)$$

$$\frac{\partial \phi}{\partial t} + \nabla . \Phi = 0 \qquad (39)$$

The distinction between the Lagrangian step and the standard Lagrangian governing equation lies primarily in their treatment of the time derivative. Specifically, the Lagrangian step incorporates a spatial time derivative, whereas the standard Lagrangian method utilizes a material time derivative within a fixed mesh framework. Conversely, the Eulerian step is concerned with calculating the transport of material volume across adjacent elements, contrasting the static original mesh with the deformed mesh. It is crucial to recognize that solution variables derived from the Lagrangian step are subsequently modified to account for material flow, as dictated by the transport algorithm. The underlying principles of the CEL approach are illustrated in Figure 90.

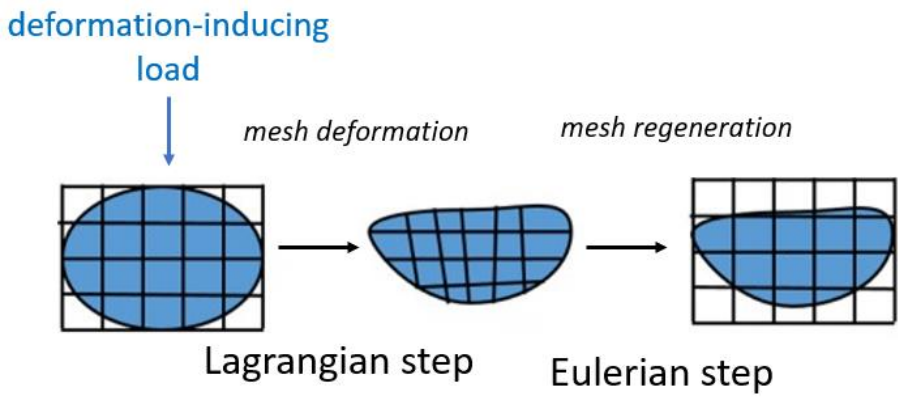

Figure 90 Principles of CEL numerical method

Considering the physics of the FSSP treatment, where the flow stress is a function of the strain, strain rate and temperature, the Johnson-Cook material model (40, 41) was chosen to represent the material of the treated specimen.

$$\sigma_{ys} = (\sigma_{ys0} + k(\varepsilon_{pe})^{n})(1 + C \log(\frac{\dot{\varepsilon}_{pe}}{\dot{\varepsilon}_0}))(1 - T_h^m) \qquad (40)$$

$$T_h = \frac{T - T_{ref}}{T_m - T_{ref}} \quad (41)$$

Where σ_{ys} denotes the yield stress, σ_{ys0} stands for initial yield stress, k is the strength coefficient, ε_{pe} denotes the effective plastic strain, n is the hardening exponent, C is strain rate strength coefficient, $\dot{\varepsilon}_{pe}$ is equivalent plastic strain, $\dot{\varepsilon}_0$ is reference equivalent plastic strain rate, $\dot{\varepsilon}_0$ is thermal softening coefficient, T_{ref} is the reference temperature ,and T_m is the melting temperature.

In a manner analogous to the numerical model developed for sample fabrication, the von Mises yield criterion was employed to more accurately depict the elastic-plastic behaviour of the material under applied loads. This approach is vital in understanding the material's response to stress and strain.

Considering the significant disparity in rigidity between the material of the processing tool and that of the processed components, it is noted that the blank holder and base plate exhibit only minimal deformations in comparison to the workpieces. Therefore, for the purposes of this model, the processing tool, base plate, and blank holder are assumed to be completely rigid bodies.

The interaction between the specimen and the rapidly rotating tool is characterized using a modified Coulomb friction model. This model distinguishes between sticking and sliding conditions based on the contact shear stress between the tool and the sample. The transition between these two states is governed by predefined criteria, as outlined in condition (42) of the model. These criteria delineate the threshold at which sticking transits to sliding or vice versa, based on the stress conditions at the contact interface.

$$\tau_{eq} < \tau_{max} \rightarrow \textit{sticking} \text{ and } \tau_{eq} > \tau_{max} \rightarrow \textit{sliding} \quad (42)$$

Where τ_{eq} is equivalent friction stress and τ_{max} is yield shear stress.

In the presented numerical model, the sum of shear stresses corresponded to the tool's torque, as seen in (43).

$$M = \int_0^{2\pi} \int_0^R r\tau dA \quad (43)$$

Contact and maximal shear stresses were then defined as follows (44, 45, 46, 47):

$$\tau_{eq} = \sqrt{(\tau^2{}_1 + \tau^2{}_2)} \quad (44)$$

$$\tau_{crit} = \mu P \quad (45)$$

$$\tau_{crit} = min(\mu P, \tau_{yie}) \quad (46)$$

$$\tau_{yie} = \frac{\sigma_y}{\sqrt{3}} \quad (47)$$

Where $\tau_{1,2}$ are orthogonal components of equivalent shear stress, τ_{crit} is critical friction shear stress, μ is friction coefficient, σ_y is a yield stress. The friction coefficient was set up to 0.3 and was constant regardless of the temperature.

Finally, the frictional heating was calculated as it is stated in (48, 49):

$$dQ = \omega dM = \omega r dF = \omega r \tau_{eq} dA \quad (48)$$

$$Q = \frac{3}{2}\pi\omega\tau_{eq} R^3 \quad (49)$$

Where Q denotes the heat source, M symbolises the moment, r is the cylindrical coordinate of the tool, F is the normal force, and A is the contact surface. In (49), directly fitted for the tool's geometry, R denotes the tool's radius.

The loading conditions and boundary constraints in this study were meticulously calibrated to replicate the experimental environment detailed in Chapter 5 of this thesis. Importantly, significant amendments were made to the simulated positioning of the rotating tool, drawing on insights from these experimental findings described in Chapter 5 of this thesis.

In the computational simulations, each specimen was discretized into 250,000 hexahedral elements, utilizing a relatively fine mesh for enhanced accuracy. The specimens undergoing processing were represented using multi-material, thermally coupled, eight-node Eulerian elements (EC3D8RT). It is imperative to note that employing a finer mesh in CEL formulations

is recommended, as it significantly enhances computational precision and reduces the likelihood of Eulerian material erroneously passing through the Lagrangian mesh. A distinctive feature of the model is the incorporation of a void layer at the upper portion of the specimen, initially devoid of any material.

The processing tool, base plate, and blank holder were discretized using four-node, thermally coupled tetrahedral elements (C3D4T), characterized by a higher mesh density. This study presents a comparative analysis of the finer Eulerian mesh applied to the processed specimens and the comparatively coarser tetrahedral Lagrangian mesh used for the processing tool, as illustrated in Figure 91.

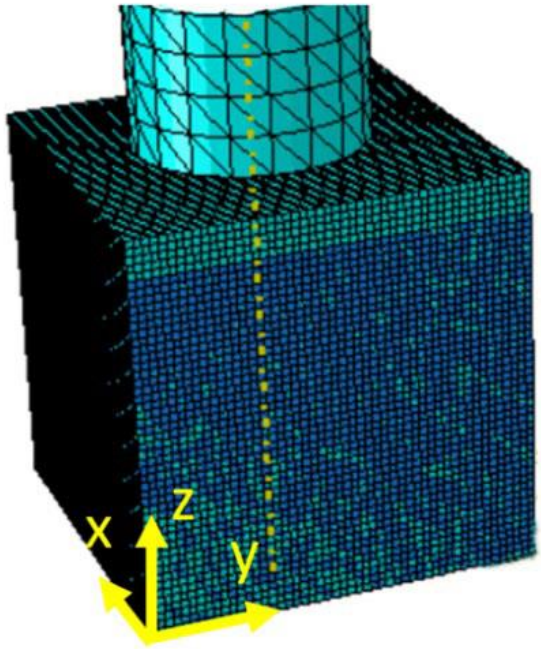

Figure 91 Comparison between the finer Eulerian mesh applied of cube specimen, and coarser tetrahedral Lagrangian mesh of the processing tool

6.3. Results

6.3.1. Cubical specimens in the as-built state

As it was described in Chapter 4 of this work, the LPBF manufacturing process has resulted in specimens with slight distortions, accumulated especially in their upper parts, as it is demonstrated in cube 2 in Figure 92.

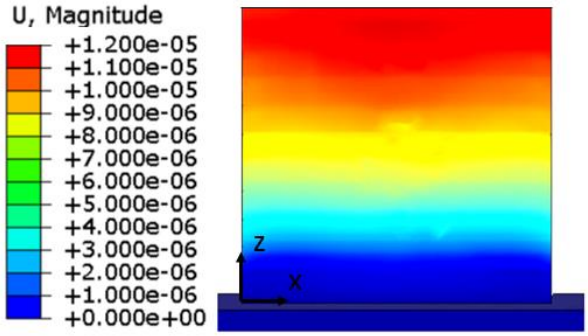

Figure 92 Simulated distribution of distortions in LPBF-manufactured cube 2

The adopted numerical model provided results of satisfactory accuracy, as the simulated distortions were in good agreement with the experimental one (Table 31).

Table 31 Comparison between simulated and experimentally assessed dimensions of manufactured cubes

	x-dimension [mm]			**y-dimension [mm]**			**z-dimension [mm]**		
	Exper.	**Sim.**	**Relative error** [%]	**Exper.**	**Sim.**	**Relative error** [%]	**Exper.**	**Sim.**	**Relative error** [%]
Cube 1	35.0461	35.0458	0.0009	35.0603	35.0598	0.0014	34.8002	34.8009	-0.0020
Cube 2	35.0158	35.0143	0.0043	35.0691	35.0688	0.0009	34.8984	34.8991	-0.0020
Cube 3	35.0387	35.0377	0.0029	35.0468	35.0464	0.0011	34.8633	34.8640	-0.0020

Moreover, the adopted numerical model was able to reasonably predict the LPBF-induced voids and lack-of-fusions, as it is demonstrated in Figure 93.

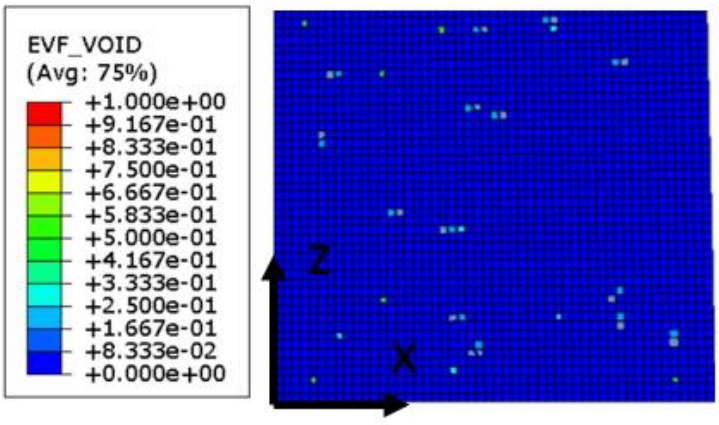

Figure 93 Simulated volume fraction of voids in LPBF-manufactured cube 2

6.3.2. Cubical specimens after the FSSP treatment

6.3.2.1. Distortions of the processed plane

The comparison between the simulated and experimental deformations of the processed plane and the specimens' height is summarized in Table 32.

Table 32 Comparison between the simulated and experimental deformations of the processed plane and the specimens' height

	Dx [mm]			**Dy** [mm]			**Dz** [mm]		
	Exper.	**Sim.**	**Relative error** [%]	**Exper.**	**Sim.**	**Relative error** [%]	**Exper.**	**Sim.**	**Relative error** [%]
Cube 1	0.1539	0.1487	3.37884	0.0197	0.0203	-3.0457	-0.0600	-0.0600	0
Cube 2	0.2042	0.2128	-4.2116	0.2309	0.2281	1.2126	-0.1500	-0.1421	5.5595
Cube 3	0.2622	0.2531	3.4706	0.0532	0.0508	4.5113	-0.2100	-0.2084	0.7678

The numerical modelling effectively replicated the material flow within the processed components, resulting in outwardly directed deformations predominantly localized around the midsections of the edges of the processed planes. Concurrently, there was an upward displacement of material, which served to counterbalance the deformation following tool retraction. Crucially, the precise positioning of the processing tool significantly influenced the distribution of distortions observed on the top planes of the cubes processed under various FSSP parameters, as illustrated in Figure 94.

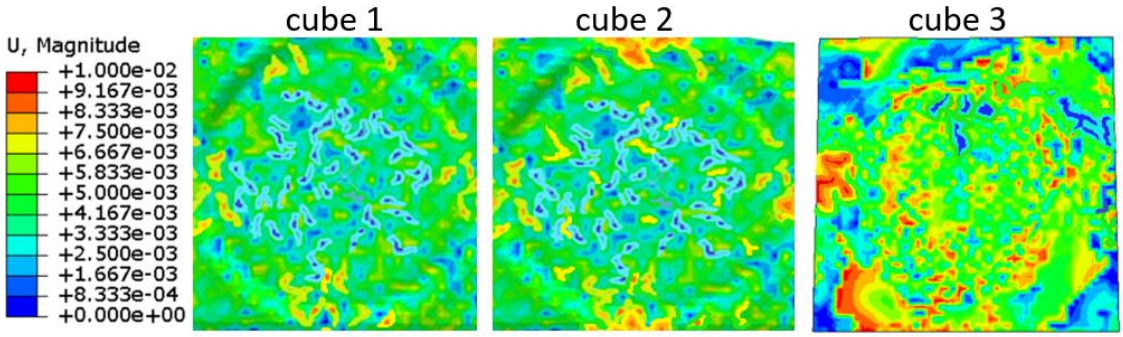

Figure 94 Simulated distribution of distortions in FSSP treated cubes

6.3.2.2. Appearance of the processed planes

The regions subjected to processing manifested a glossy surface texture, characterized by concentric corrugations encompassing the entire area beneath the processing tool, as depicted in Figure 95(a). Notably, the processed plane of Cube 1 exhibited relative clarity, in contrast to Cubes 2 and 3, which demonstrated a significant presence of flash. Additionally, all processed planes displayed the formation of short brims at the juncture of the unprocessed and processed materials, where they interface with the rotating tool. The dimensions of these brims varied among the processed cubes, correlating with the differing rotational velocities of the tool.

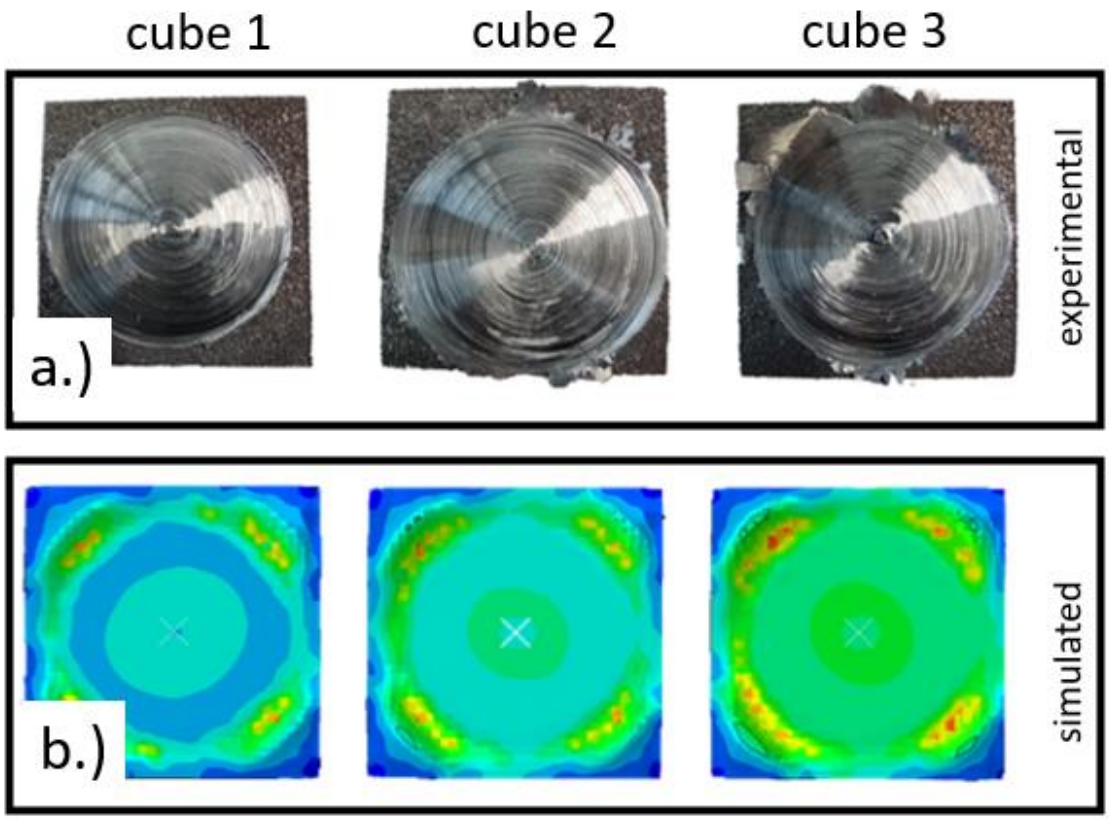

Figure 95 The appearance of the processed planes in a.) experimental and b.) simulated cubes

The implementation of the CEL numerical method in our model successfully replicated, to a certain extent, the concentric corrugation pattern observed on the surfaces of processed zones. This morphological feature, characterized by concentric, circle-like ridges, has been linked in prior studies [27,28] to the spatial variations in temperature and velocity of the material within these zones. These variations are notably influenced by the proximity to the processing center. Figure 95 b depicts the different velocities on the surface of the processed zone, which align closely with its observed concentrically ridged morphology.

It is critical to highlight that the use of a coarse computational mesh in discretizing the specimen led to a diminished representation of the corrugations. Nonetheless, it is plausible to anticipate a more accurate simulation of the surface topography of the processed zones through the application of a finer mesh. This adjustment is expected to enhance the model's ability to capture the intricate details of the surface features more faithfully.

6.3.2.3. Flesh formation

The simulation results reveal that regions exhibiting elevated velocities, predominantly located along the periphery of the processed zones (refer to Figure 95b), can be interpreted as

flash formations. This hypothesis posits that the material, excessively heated and rendered pliable, is expelled outward due to centrifugal forces. Upon reaching the cold outer space, where it is no longer exposed to heating, this material undergoes rapid solidification. Supporting this hypothesis, our simulations demonstrated a direct correlation between the emergence of flash-like structures (as depicted in Figure 96) and the specific areas exhibiting these high velocities.

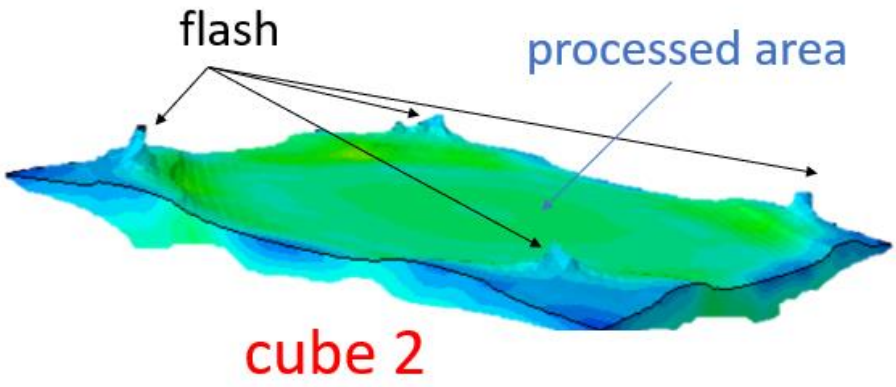

Figure 96 Detailed of processed area with formed flash

The findings indicate that the CEL numerical method provides a clear demonstration of flash formation. However, it is critical to acknowledge that the flash structures generated in simulations employing the CEL approach do not entirely coincide with those observed in experimental samples. Notably, the simulated flash was observed to be shorter and thicker compared to its experimental counterpart. This discrepancy can be primarily attributed to the insufficiently modelled thickness of the void layer, which impedes an accurate replication of material flow into the surrounding environment. Furthermore, the use of an excessively coarse computational mesh in the simulations restricts the development of suitably fine structures. Despite these limitations, the chosen mesh density and void layer thickness represent an effective balance between computational efficiency and the fidelity of the simulation. Figure 97 offers an in-depth illustration of the flash formation in cube 2, highlighting its spatial correlation with the position of the processing tool at the conclusion of the operation.

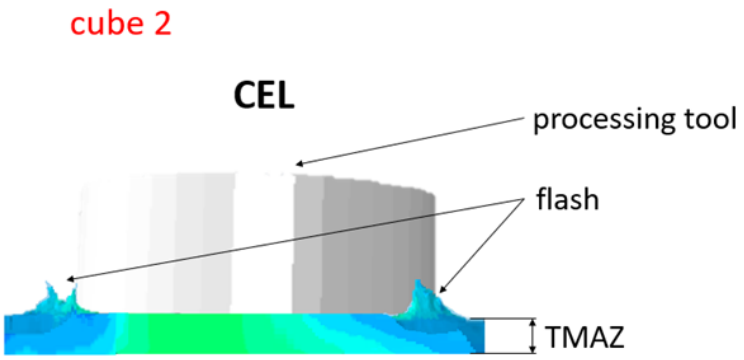

Figure 97Detailed view of the flash formed in cube 2, illustrating its relationship with the position of the processing tool at the end of the processing

The inclusion of a void layer in numerical model facilitated the realistic outward flow of material, resulting in brims that exhibited a relatively precise shape and size (Figure 98).

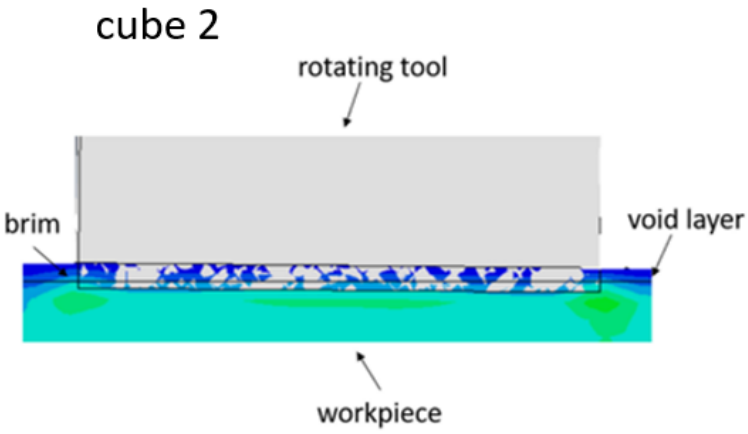

Figure 98 Flesh formation related to the presence of the void layer

6.3.2.4. Thermo-mechanically affected zones

The numerical model exhibits a high degree of accuracy in simulating the dimensions and spatial characteristics of the thermo-mechanically affected zones (TMAZ) in treated components, as depicted in Figure 96a. These simulated results closely align with the outcomes observed in the experimental campaign, illustrated in Figure 99b. Moreover, Table 33 provides a comparative analysis between the experimentally measured and numerically simulated maximal depths of the TMAZ. The low relative errors calculated in this comparison underscore the high fidelity and reliability of the proposed numerical model.

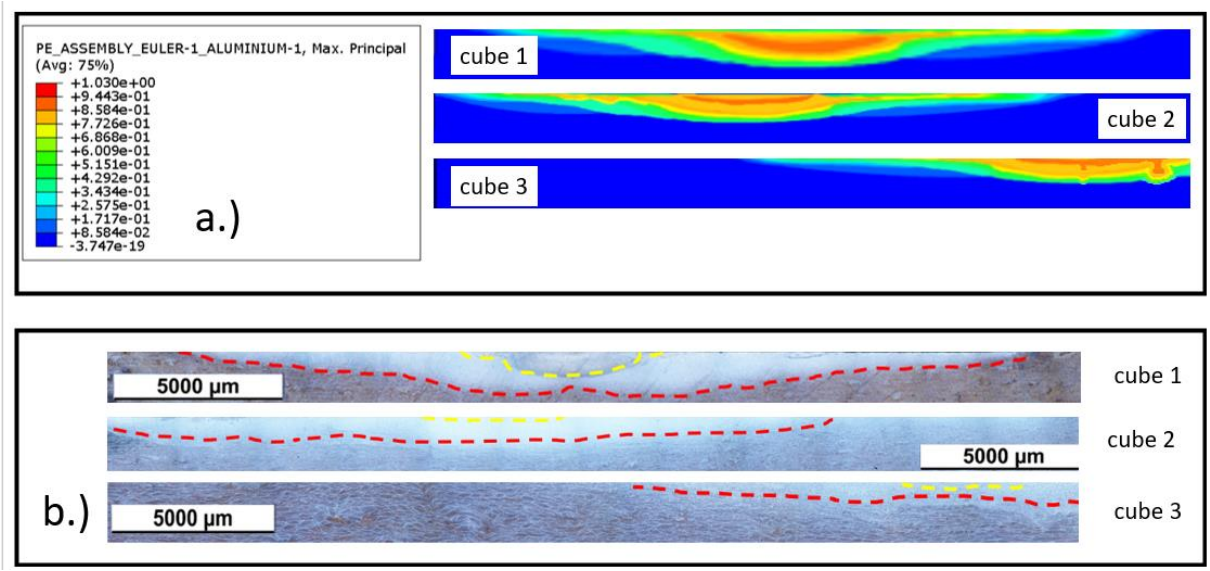

Figure 99 Comparison between a.) simulated and b.) experimental shapes and dimensions of the TMAZ

Table 33 Comparison between experimental and simulated values of maximal TMAZ depth in specimens processed under different parameters

	Maximal TMAZ depth [mm]		
	Exper.	**Sim.**	**Relative error** [%]
Cube 1	1.963	2.017	-2.751
Cube 2	1.193	1.144	4.107
Cube 3	1.058	1.107	-4.631

Moreover, the numerical model introduced in this study effectively replicates the densification effect induced by FSSP within the TMAZ, as evidenced in Figure 100. It is important to note that the fidelity of the simulated densification is highly contingent upon the chosen mesh size. A finer mesh is anticipated to substantially enhance the precision of the densification simulation. Furthermore, employing a mesh size correlating with the pore dimensions would facilitate a more comprehensive simulation of the interactions between FSSP-induced material flow and the void structures. This approach would enable the model to capture intricate processes such as void wall cracking and collapse. However, it is pertinent to consider that utilizing a finer mesh would also lead to a marked increase in the computational duration required for these numerical simulations.

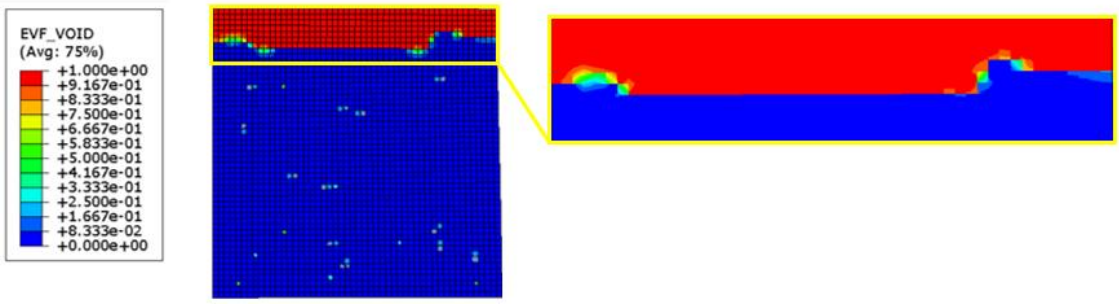

Figure 100 Void suppression in TMAZ

The findings of this investigation indicate that the developed numerical model effectively strikes a balance between computational efficiency and the accuracy for simulation. This model introduces the physical dynamics of the system, resulting in a precise representation of material flow, which, in turn, mitigates distortions and suppresses the occurrence of lack-of-fusion defects commonly associated with LPBF.

Additionally, the model potentially offers valuable insights into the temperature profiles within the treated specimens. It is important to note, however, that the fidelity of the temperature predictions has not yet been validated against empirical data. Expanding the scope of this research to include an experimental-numerical investigation of temperature distribution is proposed. Such an approach could predict the dimensions and morphology of the Heat-Affected Zone (HAZ), and indirectly infer the microstructural characteristics of the treated specimens through accurate estimations of heating rates, cooling rates, and thermal gradients.

The good knowledge of microstructural transformations resultant from FSSP is of importance for the potential precision-tailored localized modification of microstructures in components manufactured using LPBF. The differential mechanical response resulting from transformed microstructure in treated area might be especially beneficial in the production of medical implants, where it can potentially reduce the risk of stress shielding. The confluence of LPBF, with its unmatched design versatility, and FSSP's capacity for site-specific modification of mechanical properties, represents a groundbreaking advancement for the medical industry. Nonetheless, additional research is essential to fully harness the potential of these combined technologies.

7. Conclusions

The research in this thesis investigated the characteristics of AlSi10Mg components fabricated via Laser Powder Bed Fusion (LPBF) and explored innovative methods to enhance their properties by post-processing them. The study addressed the challenge posed by the improvement of LPBF process through the understanding of complex interplay among process parameters, resulting structures, and final product properties. Specifically, it was demonstrated that the unique microstructure of LPBF-manufactured AlSi10Mg components influences their response to thermal loading, reflecting microstructural alterations induced by the process. Consequently, the behavior can be further examined and applied in physical simulations, potentially advancing the development of digitalization of the entire manufacturing process for customized applications.

Therefore, the thesis tackled the fabrication of components with reduced density due to voids and porosity. We proposed a numerical model using a mesoscale approach to simulate lack-of-fusion levels based on processing parameters. The validated model encompasses phase transitions from powder to liquid and subsequent solidification, offering a detailed view of the dynamics within mushy zones. It considers also factors like a volumetric moving heat source, the non-isothermal metal flow, thermal expansion, and Marangoni effect. The proposed model is pivotal in enhancing understanding and control over the LPBF process, contributing to the broad understanding of additive manufacturing in industry.

Furthermore, the thesis examined the geometric dimensions and tolerance, and surface roughness of LPBF-manufactured blocks. The findings are highly relevant for industries requiring precision, such as healthcare, implantology, and aerospace. Optimizing specimen distribution on the build platform or compensating for position-induced distortions in CAD models can significantly improve LPBF technology effectiveness and reliability. Understanding distortions from the LPBF process is very important when specimens undergo post-processing treatments that might introduce additional displacements.

A novel thermomechanical treatment was proposed. A pinless Friction Stir Spot Process was studied for microstructure homogenization, porosity suppression, and mechanical property transformation. The low deformation levels achieved suggest FSSP capability, even in high-precision and geometrically accurate applications. Experimental trials indicated the need to select the right depth and deformation when applying pinless FSSP. Processing parameters

should be selected based on a thorough understanding of the process and/or numerical simulations. Recognizing that high deformations tend to concentrate near the specimen top surface, permits to the right placement during the build phase, which is crucial for optimizing FSSP.

To facilitate informed decision-making in selecting parameters and further understanding of FSSP physics, this thesis has proposed a novel numerical model simulating material flow in FSSP-treated AlSi10Mg components manufactured by LPBF. Given FSSP complexity and associated high strains and plastic deformations, conventional Finite Element Method (FEM) formulations often leads to mesh distortions and convergence issues. Hence, the model employs a Coupled Eulerian-Lagrangian (CEL) formulation, which, along with the physical descriptions, effectively simulated material flow, accurately predicting TMAZ dimensions, measured distortions, and flash formation, and reasonably capturing suppression of lack-of-fusions. Expanding research to include experimental-numerical studies of temperature distribution predicted the size and shape of the Heat-Affected Zone (HAZ) and indirectly determined the microstructure of treated specimens.

An enhanced understanding of microstructural transformations resulting from FSSP can be significant in the precise modification of microstructures in components fabricated via LPBF. As prior research has demonstrated, localized microstructural heterogeneity within the TMAZ of FSSP-treated materials evokes an anisotropic mechanical response, exemplified by variations in stiffness compared to regions unaffected by FSSP.

The integration of LPBF, which offers unparalleled design flexibility, with FSSP's capability for localized mechanical property customization holds a transformative potential for the various industries. However, further research is necessary to fully exploit these technological synergies.

The future works will include the study of the effects of FSSP on the mechanical performance of the treated components. Further optimisation endeavours will include the tool’s size and shape optimisation. We will study the feasibility of FSSP processing of the irregularly shaped specimens. Moreover, our future research will include the study of the synergies of LPBF and FSSP techniques for biocompatible materials, as we see their potential benefit for healthcare and implant manufacturing.

References

[1] Ngo TD, Kashani A, Imbalzano G, Nguyen KTQ, Hui D. Additive manufacturing (3D printing): A review of materials, methods, applications and challenges. Composites Part B: Engineering. 2018;143:172-196. doi:10.1016/j.compositesb.2018.02.012

[2] Praveena BA, Lokesh N, Buradi A, Santhosh N, Praveena BL, Vignesh R. A comprehensive review of emerging additive manufacturing (3D printing technology): Methods, materials, applications, challenges, trends and future potential. Materials Today: Proceedings. 2022;52(3):1309-1313. doi:10.1016/j.matpr.2021.11.059

[3] Jandyal A, Chaturvedi I, Wazir I, Raina A, Ul Haq MI. 3D printing – A review of processes, materials and applications in industry 4.0. Sustainable Operations and Computers. 2022;3:33-42. doi:10.1016/j.susoc.2021.09.004

[4] Mansi, Kumar H, Singholi AKS, Moona G. Additive Manufacturing: A Brief Introduction. In: Aswal DK, Yadav S, Takatsuji T, Rachakonda P, Kumar H, editors. Handbook of Metrology and Applications. Springer, Singapore; 2022. doi:10.1007/978-981-19-1550-5_59-1

[5] Diegel O. Additive Manufacturing: An Overview. In: Hashmi S, Batalha GF, Van Tyne CJ, Yilbas B, editors. Comprehensive Materials Processing. Elsevier; 2014. p. 3-18. doi:10.1016/B978-0-08-096532-1.01000-1

[6] Tempelman E, Shercliff H, Ninaber van Eyben B. Additive Manufacturing. In: Tempelman E, Shercliff H, Ninaber van Eyben B, editors. Manufacturing and Design. Butterworth-Heinemann; 2014. p. 187-200. doi:10.1016/B978-0-08-099922-7.00011-1

[7] Song XT, Kuo JY, Chen CH. Design methodologies for conventional and additive manufacturing. In: Patel CD, Chen CH, editors. Digital Manufacturing. Elsevier; 2022. p. 97-143. doi:10.1016/B978-0-323-95062-6.00007-3

[8] Leary M. AM production economics. In: Leary M, editor. Additive Manufacturing Materials and Technologies, Design for Additive Manufacturing. Elsevier; 2020. p. 7-31. doi:10.1016/B978-0-12-816721-2.00002-6

[9] Leary M. Introduction to AM. In: Leary M, editor. Additive Manufacturing Materials and Technologies, Design for Additive Manufacturing. Elsevier; 2020. p. 1-6. doi:10.1016/B978-0-12-816721-2.00001-4

[10] Cai C, Zhou K. Metal additive manufacturing. In: Patel CD, Chen CH, editors. Digital Manufacturing. Elsevier; 2022. p. 247-298. doi:10.1016/B978-0-323-95062-6.00005-X

[11] Park S, Deng K, Fu KK. Additive manufacturing including laser-based manufacturing. In: Narayanan RG, Gunasekera JS, editors. Sustainable Manufacturing Processes. Academic Press; 2023. p. 285-311. ISBN 9780323999908. https://doi.org/10.1016/B978-0-323-99990-8.00010-2.

[12] Gibson I, Rosen D, Stucker B, Khorasani M. Generalized Additive Manufacturing Process Chain. In: Additive Manufacturing Technologies. Springer; 2021. https://doi.org/10.1007/978-3-030-56127-7_3.

[13] Alghamdi SS, John S, Roy Choudhury N, Dutta NK. Additive Manufacturing of Polymer Materials: Progress, Promise and Challenges. Polymers. 2021; 13(5):753. https://doi.org/10.3390/polym13050753.

[14] Nath SD, Nilufar S. An Overview of Additive Manufacturing of Polymers and Associated Composites. Polymers. 2020; 12(11):2719. https://doi.org/10.3390/polym12112719.

[15] Sames WJ, List FA, Pannala S, Dehoff RR, Babu SS. The metallurgy and processing science of metal additive manufacturing. Int Mater Rev. 2016;61(5):315-360. https://doi.org/10.1080/09506608.2015.1116649.

[16] Tan C, Weng F, Sui S, Chew Y, Bi G. Progress and perspectives in laser additive manufacturing of key aeroengine materials. Int J Mach Tools Manuf. 2021;170:103804. https://doi.org/10.1016/j.ijmachtools.2021.103804.

[17] Chowdhury S, Yadaiah N, Prakash C, Ramakrishna S, Dixit S, Gupta LR, Buddhi D. Laser powder bed fusion: a state-of-the-art review of the technology, materials, properties & defects, and numerical modelling. J Mater Res Technol. 2022;20:2109-2172. https://doi.org/10.1016/j.jmrt.2022.07.121.

[18] Kushwaha AK, Rahman MH, Slater E, Patel R, Evangelista C, Austin E, Tompkins E, McCarroll A, Rajak DK, Menezes PL. Powder bed fusion–based additive manufacturing: SLS, SLM, SHS, and DMLS. In: Kumar P, Misra M, Menezes PL, editors. Tribology of Additively Manufactured Materials. Elsevier; 2022. p. 1-37. ISBN 9780128213285. https://doi.org/10.1016/B978-0-12-821328-5.00001-9.

[19] Cacace S, Demir AG, Grande AM, Sala G, Influence of production batch related parameters on static and fatigue resistance of LPBF produced AlSi7Mg0.6. Int J Fatigue. 2022;165:107227. https://doi.org/10.1016/j.ijfatigue.2022.107227.

[20]Aboulkhair NT, Everitt NM, Ashcroft I, Tuck C. Reducing porosity in AlSi10Mg parts processed by selective laser melting. Addit Manuf. 2014;1-4:77-86. https://doi.org/10.1016/j.addma.2014.08.001.

[21] Rashid R, Masood S, Ruan D, Palanisamy S, Huang X, Rahman Rashid RA. Design Optimization and Finite Element Model Validation of LPBF-Printed Lattice-Structured Beams. Metals. 2023;13(2):184. doi:10.3390/met13020184.

[22] Wurst J, Mozgova I, Lachmayer R. Sustainability Assessment of Products manufactured by the Laser Powder Bed Fusion (LPBF) Process. Procedia CIRP. 2022;105:243-248. doi:10.1016/j.procir.2022.02.040.

[23] Abd-Elaziem W, Elkatatny S, Abd-Elaziem AE, Khedr M, Abd El-baky MA, Hassan MA, Abu-Okail M, Mohammed M, Järvenpää A, Allam T, Hamada A. On the current research progress of metallic materials fabricated by laser powder bed fusion process: a review. J Mater Res Technol. 2022;20:681-707. doi:10.1016/j.jmrt.2022.07.085.

[24] Nandhakumar R, Venkatesan K. A process parameters review on selective laser melting-based additive manufacturing of single and multi-material: Microstructure, physical properties, tribological, and surface roughness. Mater Today Commun. 2023;35:105538. doi:10.1016/j.mtcomm.2023.105538.

[25] Großmann A, Gosmann J, Mittelstedt C. Lightweight lattice structures in selective laser melting: Design, fabrication and mechanical properties. Mater Sci Eng A. 2019;766:138356. doi:10.1016/j.msea.2019.138356.

[26] Yan C, Hao L, Hussein A, Young P, Raymont D. Advanced lightweight 316L stainless steel cellular lattice structures fabricated via selective laser melting. Mater Des. 2014;55:533-541. doi:10.1016/j.matdes.2013.10.027.

[27] ZHU J, ZHOU H, WANG C, ZHOU L, YUAN S, ZHANG W. A review of topology optimization for additive manufacturing: Status and challenges. Chin J Aeronaut. 2021;34(1):91-110. doi:10.1016/j.cja.2020.09.020.

[28] Ponnusamy P, Rahman Rashid RA, Masood SH, Ruan D, Palanisamy S. Mechanical Properties of SLM-Printed Aluminium Alloys: A Review. Materials. 2020;13(19):4301. doi:10.3390/ma13194301.

[29] Brough D, Jouhara H. The aluminium industry: A review on state-of-the-art technologies, environmental impacts and possibilities for waste heat recovery. Int J Thermofluids. 2020;1–2:100007. doi:10.1016/j.ijft.2019.100007.

[30] Alamdari H. Aluminium Production Process: Challenges and Opportunities. Metals. 2017;7(4):133. doi:10.3390/met7040133.

[31] Ambroziak A, Solarczyk M. Application and mechanical properties of aluminium alloys. In: Editors' Name(s), ed. Book Title. Publisher; Year. p. Page Numbers. doi: 10.1201/9781315166605-121.

[32] Rometsch PA, Zhu Y, Wu X, Huang A, Review of high-strength aluminium alloys for additive manufacturing by laser powder bed fusion. Mater Des. 2022;219:110779. doi: 10.1016/j.matdes.2022.110779.

[33] Zhu Z, Hu Z, Seet HL, Liu T, Liao W, Ramamurty U, Nai SML. Recent progress on the additive manufacturing of aluminum alloys and aluminum matrix composites: Microstructure, properties, and applications. Int J Mach Tools Manuf. 2023;190:104047. doi: 10.1016/j.ijmachtools.2023.104047.

[34] Aboulkhair NT, Simonelli M, Parry L, Ashcroft I, Tuck C, Hague R. 3D printing of Aluminium alloys: Additive Manufacturing of Aluminium alloys using selective laser melting. Prog Mater Sci. 2019;106:100578. doi: 10.1016/j.pmatsci.2019.100578.

[35] Olakanmi EO, Cochrane RF, Dalgarno KW. A review on selective laser sintering/melting (SLS/SLM) of aluminium alloy powders: Processing, microstructure, and properties. Prog Mater Sci. 2015;74:401-477. doi: 10.1016/j.pmatsci.2015.03.002.

[36] Louvis E, Fox P, Sutcliffe CJ. Selective laser melting of aluminium components. J Mater Process Technol. 2011;211(2):275-284. doi: 10.1016/j.jmatprotec.2010.09.019.

[37] Ghasemi A, Fereiduni E, Balbaa M, Jadhav SD, Elbestawi M, Habibi S. Influence of alloying elements on laser powder bed fusion processability of aluminum: A new insight into the oxidation tendency. Addit Manuf. 2021;46:102145. doi: 10.1016/j.addma.2021.102145.

[38] Zhang J, Song B, Wei Q, Bourell D, Shi Y. A review of selective laser melting of aluminum alloys: Processing, microstructure, property and developing trends. J Mater Sci Technol. 2019;35(2):270-284. doi: 10.1016/j.jmst.2018.09.004.

[39] Kleiven D, Akola J. Precipitate formation in aluminium alloys: Multi-scale modelling approach. Acta Mater. 2020;195:123-131. doi: 10.1016/j.actamat.2020.05.050.

[40] Tisza M. Physical metallurgy for engineers. ASM International and Fruend Publishing House Ltd.; 2002.

[41] Totten GE, Mackenzie DS. Handbook of Aluminum: Physical Metallurgy and Processes. 1st ed. New York: CRC Press; 2003.

[42] Zhao H, White DR, DebRoy T. Current issues and problems in laser welding of automotive aluminium alloys. Int Mater Rev. 1999;44:238-66.

[43] Rogers S, Dargusch M, Kent D. Impacts of Temperature and Time on Direct Nitridation of Aluminium Powders for Preparation of AlN Reinforcement. Materials. 2023;16(4):1583. doi:10.3390/ma16041583

[44] Xiao Z, Yu W, Fu H, Deng Y, Wu Y, Zheng H. Recent progress on microstructure manipulation of aluminium alloys manufactured via laser powder bed fusion. Virtual Phys Prototyp. 2023;18(1). doi:10.1080/17452759.2022.2125880

[45] Cacace S, Semeraro Q. Influence of the atomization medium on the properties of stainless steel SLM parts. Addit Manuf. 2020;36:101509. doi:10.1016/j.addma.2020.101509

[46] Powell D, Rennie AEW, Geekie L, Burns N. Understanding powder degradation in metal additive manufacturing to allow the upcycling of recycled powders. J Clean Prod. 2020;268:122077. doi:10.1016/j.jclepro.2020.122077

[47] Brika SE, Letenneur M, Dion CA, Brailovski V. Influence of particle morphology and size distribution on the powder flowability and laser powder bed fusion manufacturability of Ti-6Al-4V alloy. Addit Manuf. 2020;31:100929. doi:10.1016/j.addma.2019.100929

[48] Hu Z, Gao S, Zhang L, et al. Micro laser powder bed fusion of stainless steel 316L: Cellular structure, grain characteristics, and mechanical properties. Mater Sci Eng A. 2022;848:143345. doi:10.1016/j.msea.2022.143345

[49] Nguyen QB, Luu DN, Nai SML, Zhu Z, Chen Z, Wei J. The role of powder layer thickness on the quality of SLM printed parts. Arch Civil Mech Eng. 2018;18(3):948-955. doi:10.1016/j.acme.2018.01.015

[50] Nagarajan B, Hu Z, Song X, Zhai W, Wei J. Development of Micro Selective Laser Melting: The State of the Art and Future Perspectives. Engineering. 2019;5(4):702-720. doi:10.1016/j.eng.2019.07.002

[51] Alijagic A, Engwall M, Särndahl E, et al. Particle Safety Assessment in Additive Manufacturing: From Exposure Risks to Advanced Toxicology Testing. Front Toxicol. 2022;4:836447. doi:10.3389/ftox.2022.836447. PMID: 35548681; PMCID: PMC9081788.

[52] Arrizubieta JI, Ukar O, Ostolaza M, Mugica A. Study of the Environmental Implications of Using Metal Powder in Additive Manufacturing and Its Handling. Metals. 2020;10(2):261. https://doi.org/10.3390/met10020261

[53] Faludi J, Baumers M, Maskery I, Hague R. Environmental Impacts of Selective Laser Melting: Do Printer, Powder, Or Power Dominate? J Ind Ecol. 2017;21:S144-S156. https://doi.org/10.1111/jiec.12528

[54] Feng Y, Zhou Q, Wang C, Yan Z, Liu B. Effect of powder reuse on powder characteristics and properties of Inconel 718 parts produced by selective laser melting. J Mater Res Technol. 2021;13:524-533. https://doi.org/10.1016/j.jmrt.2021.04.091

[55] Cordova L, Campos M, Tinga T. Revealing the Effects of Powder Reuse for Selective Laser Melting by Powder Characterization. JOM. 2019;71:1062–1072. https://doi.org/10.1007/s11837-018-3305-2

[56] Coşkun M, Dizdar KC, Tarakçi G, Özer G, Dispinar D. Recycling of additive manufactured AlSi10Mg and its effect on mechanical properties. Mater Chem Phys. 2022;289:126411. https://doi.org/10.1016/j.matchemphys.2022.126411

[57] Weiss C, Haefner CL, Munk J. On the Influence of AlSi10Mg Powder Recycling Behavior in the LPBF Process and Consequences for Mechanical Properties. JOM. 2022;74:1188–1199. https://doi.org/10.1007/s11837-021-05080-4

[58] Emminghaus N, Hoff C, Hermsdorf J, Kaierle S. Residual oxygen content and powder recycling: Effects on surface roughness and porosity of additively manufactured Ti-6Al-4V. Addit Manuf. 2021;46:102093. https://doi.org/10.1016/j.addma.2021.102093

[59] Rausch AM, Küng VE, Pobel C, Markl M, Körner C. Predictive Simulation of Process Windows for Powder Bed Fusion Additive Manufacturing: Influence of the Powder Bulk Density. Mater. 2017;10(10):1117. https://doi.org/10.3390/ma10101117

[60] Masiagutova E, Cabanettes F, Sova A, Cici M, Bidron G, Bertrand P. Side surface topography generation during laser powder bed fusion of AlSi10Mg. Addit Manuf. 2021;47:102230. https://doi.org/10.1016/j.addma.2021.102230

[61] DePond PJ, Fuller JC, Khairallah SA, et al. Laser-metal interaction dynamics during additive manufacturing resolved by detection of thermally-induced electron emission. Commun Mater. 2020;1:92. doi:10.1038/s43246-020-00094-y.

[62] Narasimharaju SR, Zeng W, See TL, et al. A comprehensive review on laser powder bed fusion of steels: Processing, microstructure, defects and control methods, mechanical properties, current challenges and future trends. J Manuf Process. 2022;75:375-414. doi:10.1016/j.jmapro.2021.12.033.

[63] Martin AA, Calta NP, Hammons JA, et al. Ultrafast dynamics of laser-metal interactions in additive manufacturing alloys captured by in situ X-ray imaging. Mater Today Adv. 2019;1:100002. doi:10.1016/j.mtadv.2019.01.001.

[64] Sendino S, Gardon M, Lartategui F, Martinez S. The Effect of the Laser Incidence Angle in the Surface of L-PBF Processed Parts. Coatings. 2020;10(11):1024. doi:10.3390/coatings10111024.

[65] Sendino S, Martinez S, Lartategui F, et al. Effect of powder particle size distribution on the surface finish of components manufactured by laser powder bed fusion. Int J Adv Manuf Technol. 2023;124:789-799. doi:10.1007/s00170-022-10423-9.

[66] Le TN, Lo YL. Effects of sulfur concentration and Marangoni convection on melt-pool formation in transition mode of selective laser melting process. Mater Des. 2019;179:107866. doi:10.1016/j.matdes.2019.107866.

[67] Korner C, Attar E, Heinl P. Mesoscopic simulation of selective beam melting processes. J Mater Process Technol. 2011;211(6):978-987.

[68] Khairallah SA, Anderson AT, Rubenchik A, King WE. Laser powder-bed fusion additive manufacturing: physics of complex melt flow and formation mechanisms of pores, spatter, and denudation zones. Acta Mater. 2016;108:36-45.

[69] Das S. Physical aspects of process control in selective laser sintering of metals. Adv Eng Mater. 2003;5(10):701-711.

[70] Zhang D, Zhang P, Liu Z, et al. Thermofluid field of molten pool and its effects during selective laser melting (SLM) of Inconel 718 alloy. Addit. Manuf. 2018;21:567-578.

[71] Liu J, Wen P. Metal vaporization and its influence during laser powder bed fusion process. Materials & Design. 2022;215:110505. doi:10.1016/j.matdes.2022.110505.

[72] Yin J, Zhang W, Ke L, Wei H, Wang D, Yang L, Zhu H, Dong P, Wang G, Zeng X. Vaporization of alloying elements and explosion behavior during laser powder bed fusion of Cu–10Zn alloy. Int J Mach Tools Manuf. 2021;161:103686. doi:10.1016/j.ijmachtools.2020.103686.

[73] Jakumeit J, et al. 2020. IOP Conf. Ser.: Mater. Sci. Eng. 861:012011.

[74] Qin Y, Liu J, Chen Y, Wen P, Zheng Y, Tian Y, Voshage M, Schleifenbaum JH. Influence of Laser Energy Input and Shielding Gas Flow on Evaporation Fume during Laser Powder Bed Fusion of Zn Metal. Materials. 2021;14(10):2677. doi:10.3390/ma14102677.

[75] Viale V, Stavridis J, Salmi A, et al. Optimisation of downskin parameters to produce metallic parts via laser powder bed fusion process: an overview. Int J Adv Manuf Technol. 2022;123:2159–2182. doi:10.1007/s00170-022-10314-z.

[76] Ur Rehman A, Mahmood MA, Ansari P, Pitir F, Salamci MU, Popescu AC, Mihailescu IN. Spatter Formation and Splashing Induced Defects in Laser-Based Powder Bed Fusion of AlSi10Mg Alloy: A Novel Hydrodynamics Modelling with Empirical Testing. Metals. 2021;11(12):2023. doi:10.3390/met11122023.

[77] Lutter-Günther M, Bröker M, Mayer T, Lizak S, Seidel C, Reinhart G. Spatter formation during laser beam melting of AlSi10Mg and effects on powder quality. Procedia CIRP. 2018;74:33-38. doi:10.1016/j.procir.2018.08.008.

[78] Matthews MJ, Guss G, Khairallah SA, Rubenchik AM, Depond PJ, King WE. Denudation of metal powder layers in laser powder bed fusion processes. Acta Mater. 2016;114:33-42. doi:10.1016/j.actamat.2016.05.017.

[79] Khmyrov RS, Ableeva RR, Gusarov AV. Metallographic study of denudation in laser powder-bed fusion. Procedia CIRP. 2020;94:194-199. doi:10.1016/j.procir.2020.09.037.

[80] Zhang B, Li Y, Bai Q. Defect Formation Mechanisms in Selective Laser Melting: A Review. Chin J Mech Eng. 2017;30:515–527. doi:10.1007/s10033-017-0121-5.

[81] Le TN, Lo YL, Chen KY, Hung W. Numerical and experimental investigation into powder entrainment and denudation phenomena in laser powder bed fusion process. Powder Technol. 2022;410:117907. doi:10.1016/j.powtec.2022.117907.

[82] Kaserer L, Bergmueller S, Braun J, et al. Vacuum laser powder bed fusion—track consolidation, powder denudation, and future potential. Int J Adv Manuf Technol. 2020;110:3339–3346. doi:10.1007/s00170-020-06071-6.

[83] Li X, Guo Q, Chen L, Tan W. Quantitative investigation of gas flow, powder-gas interaction, and powder behavior under different ambient pressure levels in laser powder bed fusion. Int J Mach Tools Manuf. 2021;170:103797. doi:10.1016/j.ijmachtools.2021.103797.

[84] Glicksman ME. Principles of solidification: an introduction to modern casting and crystal growth concepts. Springer Science & Business Media; 2010.

[85] Gong X, Chou K. Phase-field modeling of microstructure evolution in electron beam additive manufacturing. JOM. 2015;67(5):1176-1182.

[86] Niendorf T, Leuders S, Riemer A, Richard HA, Schwarze D, Troster T. Highly anisotropic steel processed by selective lasermelting. Minerals, Metals & Materials Society and ASM International; 2013.

[87] Marola S, Manfredi D, Fiore G, Poletti MG, Lombardi M, Fino P, Battezzati L. A comparison of Selective Laser Melting with bulk rapid solidification of AlSi10Mg alloy. J Alloys Compd. 2018;742:271-279. doi:10.1016/j.jallcom.2018.01.309.

[88] Van Cauwenbergh P, Samaee V, Thijs L, et al. Unravelling the multi-scale structure–property relationship of laser powder bed fusion processed and heat-treated AlSi10Mg. Sci Rep. 2021;11:6423. doi:10.1038/s41598-021-85047-2.

[89] Qin H, Dong Q, Fallah V, et al. Rapid Solidification and Non-equilibrium Phase Constitution in Laser Powder Bed Fusion (LPBF) of AlSi10Mg Alloy: Analysis of Nano-precipitates, Eutectic Phases, and Hardness Evolution. Metall Mater Trans A. 2020;51:448–466. doi:10.1007/s11661-019-05505-5.

[90] Tang M, Pistorius P, Narra S, Beuth J. Rapid Solidification: Selective Laser Melting of AlSi10Mg. JOM. 2016;68. doi:10.1007/s11837-015-1763-3.

[91] Pelevin IA, Ozherelkov DY, Nalivaiko AY, Bodyakova AI, Chernyshikhin SV, Zotov BO, Korshunov AV, Gromov AA. AlSi10Mg/AlN Interface Grain Structure after Laser Powder Bed Fusion. Metals. 2022;12(12):2152. doi:10.3390/met12122152

[92] Moura DA, et al. 2023. IOP Conf. Ser.: Mater. Sci. Eng. 1274:012016.

[93] Zhao L, Song L, Santos Macías JG, Zhu Y, Huang M, Simar A, Li Z. Review on the correlation between microstructure and mechanical performance for laser powder bed fusion AlSi10Mg. Additive Manufacturing. 2022;56:102914. doi:10.1016/j.addma.2022.102914.

[94] Albu M, Krisper R, Lammer J, Kothleitner G, Fiocchi J, Bassani P. Microstructure evolution during in-situ heating of AlSi10Mg alloy powders and additive manufactured parts. Additive Manufacturing. 2020;36:101605. doi:10.1016/j.addma.2020.101605.

[95] Du J, Ren Y, Liu X, Xu F, Wang X, Zhou R, Baker I, Wu H. Microstructural Evolution, Mechanical Properties and Tribological Behavior of B4C-Reinforced Ti In Situ Composites Produced by Laser Powder Bed Fusion. Materials. 2023;16(13):4890. doi:10.3390/ma16134890

[96] Snopiński P, Woźniak A, Pagáč M. Microstructural Evolution, Hardness, and Strengthening Mechanisms in SLM AlSi10Mg Alloy Subjected to Equal-Channel Angular Pressing (ECAP). Materials (Basel). 2021 Dec 10;14(24):7598. doi:10.3390/ma14247598.

[97] Kaess M, Werz M, Weihe S. Residual Stress Formation Mechanisms in Laser Powder Bed Fusion—A Numerical Evaluation. Materials. 2023;16(6):2321. doi:10.3390/ma16062321

[98] Serrano-Munoz I, Mishurova T, Thiede T, et al. The residual stress in as-built Laser Powder Bed Fusion IN718 alloy as a consequence of the scanning strategy induced microstructure. Sci Rep. 2020;10:14645. doi:10.1038/s41598-020-71112-9

[99] Smith WL, Roehling JD, Strantza M, et al. Residual stress analysis of in situ surface layer heating effects on laser powder bed fusion of 316L stainless steel. Additive Manufacturing. 2021;47:102252. doi:10.1016/j.addma.2021.102252.

[100] Homami RM, Ojo O. Residual stress analysis through numerical simulation in powder bed additive manufacturing using the representative volume approach. Int J Adv Manuf Technol. 2023. doi:10.1007/s00170-023-12634-0

[101] Jha A, Shukla S, Choudhary A, Manoharan R, Muvvala G. A study on developing process-structure–property relationship with molten pool thermal history during laser surface remelting of Inconel 718. Optics & Laser Technology. 2023;157:108732. doi:10.1016/j.optlastec.2022.108732.

[102] Guan J, Wang Q. Laser Powder Bed Fusion of Dissimilar Metal Materials: A Review. Materials (Basel). 2023;16(7):2757. doi:10.3390/ma16072757.

[103] Jiang Q, Li S, Guo S, Fu M, Zhang B. Comparative study on process-structure-property relationships of TiC/Ti6Al4V and Ti6Al4V by selective laser melting. International Journal of Mechanical Sciences. 2023;241:107963. doi:10.1016/j.ijmecsci.2022.107963.

[104] Yu T, Hyer H, Sohn Y, Bai Y, Wu D. Structure-property relationship in high strength and lightweight AlSi10Mg microlattices fabricated by selective laser melting. Materials & Design. 2019;182:108062. doi:10.1016/j.matdes.2019.108062.

[105] Pan W, Ye Z, Zhang Y, Liu Y, Liang B, Zhai Z. Research on Microstructure and Properties of AlSi10Mg Fabricated by Selective Laser Melting. Materials. 2022;15(7):2528. doi:10.3390/ma15072528

[106] Scipioni Bertoli U, Wolfer AJ, Matthews MJ, Delplanque J-PR, Schoenung JM. On the limitations of volumetric energy density as a design parameter for selective laser, Melt Mater Des. 2017;113:331-340.

[107] Schleifenbaum H, Meiners W, Wissenbach K, Hinke C. Individualized production by means of high power Selective Laser Melting. CIRP J Manuf Sci Technol. 2010;2:161-169.

[108] Kamath C, El-dasher B, Gallegos GF, King WE, Sisto A. Density of additively-manufactured, 316L SS parts using laser powder-bed fusion at powers up to 400W. Int J f Addit Manuf Techol. 2013;74:65-78.

[109] Buchbinder D, Schleifenbaum H, Heidrich S, Meiners W, Bültmann J. High power selective laser melting (HP SLM) of aluminum parts. Phys Proc. 2011;12(Part A):271-278.

[110] Aboulkhair NT, Maskery I, Tuck C, Ashcroft I, Everitt NM. On the formation of AlSi10Mg single tracks and layers in selective laser melting: microstructure and nano-mechanical properties. J Mater Process Technol. 2016;230:88-98.

[111] Thijs L, Kempen K, Kruth JP, Van Humbeeck J. Fine-structured aluminium products with controllable texture by selective laser melting of pre-alloyed AlSi10Mg powder. Acta Mater. 2013;61:1809-1819.

[112] Zhuang JR, Lee YT, Hsieh WH, Yang AS. Determination of melt pool dimensions using DOE-FEM and RSM with process window during SLM of Ti6Al4V powder. Opt Laser Technol. 2018;103:59-76. https://doi.org/10.1016/j.optlastec.2018.01.013.

[113] Coen V, Goossens L, Van Hooreweder B. Methodology and experimental validation of analytical melt pool models for laser powder bed fusion. J Mater Process Technol. 2022;304:117547. https://doi.org/10.1016/j.jmatprotec.2022.117547.

[114] Naderi M, Weaver J, Deisenroth D, et al. On the Fidelity of the Scaling Laws for Melt Pool Depth Analysis During Laser Powder Bed Fusion. Integr Mater Manuf Innov. 2023;12:11–26. https://doi.org/10.1007/s40192-022-00289-w.

[115] Hann DB, Iammi J, Folkes J. A simple methodology for predicting laser-weld properties from material and laser parameters. J Phys D Appl Phys. 2011;44(44):445401.

[116] Liu X, Zhao C, Zhou X, Shen Z, Liu W. Microstructure of selective laser melted AlSi10Mg alloy. Mater Des. 2019;168:107677. https://doi.org/10.1016/j.matdes.2019.107677.

[117] Trevisan F, Calignano F, Lorusso M, et al. On the Selective Laser Melting (SLM) of the AlSi10Mg Alloy: Process, Microstructure, and Mechanical Properties. Materials. 2017;10(1):76. https://doi.org/10.3390/ma10010076.

[118] Guzanová A, Draganovská D, Ižaríková G, et al. The Effect of Position of Materials on a Build Platform on the Hardness, Roughness, and Corrosion Resistance of Ti6Al4V Produced by DMLS Technology. Metals. 2019;9(10):1055. https://doi.org/10.3390/met9101055.

[119] Maamoun AH, Xue YF, Elbestawi MA, Veldhuis SC. The Effect of Selective Laser Melting Process Parameters on the Microstructure and Mechanical Properties of Al6061 and AlSi10Mg Alloys. Materials. 2019;12(1):12. https://doi.org/10.3390/ma12010012.

[120] Yang M, Wang L, Yan W. Phase-field modeling of grain evolution in additive manufacturing with addition of reinforcing particles. Addit Manuf. 2021;47:102286. https://doi.org/10.1016/j.addma.2021.102286.

[121] Lu HZ, Ma HW, Yang Y, et al. Tailoring phase transformation behavior, microstructure, and superelasticity of NiTi shape memory alloys by specific change of laser power in selective laser melting. Mater Sci Eng A. 2023;864:144576. https://doi.org/10.1016/j.msea.2022.144576.

[122] Lin WC, Chang YJ, Hsu TH, et al. Microstructure and tensile property of a precipitation strengthened high entropy alloy processed by selective laser melting and post heat treatment. Addit Manuf. 2020;36:101601. https://doi.org/10.1016/j.addma.2020.101601.

[123] Großmann A, Mölleney J, Frölich T, et al. Dimensionless process development for lattice structure design in laser powder bed fusion. Mater Des. 2020;194:108952. https://doi.org/10.1016/j.matdes.2020.108952.

[124] Sola A, Defanti S, Mantovani S, et al. Technological Feasibility of Lattice Materials by Laser-Based Powder Bed Fusion of A357.0. 3D Print Addit Manuf. 2020;7(1):1-7. https://doi.org/10.1089/3dp.2019.0119.

[125] Levkulich NC, Semiatin SL, Gockel JE, Middendorf JR, DeWald AT, Klingbeil NW. The effect of process parameters on residual stress evolution and distortion in the laser powder bed fusion of Ti-6Al-4V. Addit Manuf. 2019;28:475-484. https://doi.org/10.1016/j.addma.2019.05.015.

[126] Bian P, Shi J, Liu Y, Xie Y. Influence of laser power and scanning strategy on residual stress distribution in additively manufactured 316L steel. Opt Laser Technol. 2020;132:106477. https://doi.org/10.1016/j.optlastec.2020.106477.

[127] Jiang X, Ye T, Zhu Y. Effect of process parameters on residual stress in selective laser melting of AlSi10Mg. Mater Sci Technol. 2020;36(3):342-352. https://doi.org/10.1080/02670836.2019.1705560.

[128] Čapek J, Polatidis E, Casati N, Pederson R, Lyphout C, Strobl M. Influence of laser powder bed fusion scanning pattern on residual stress and microstructure of alloy 718. Mater Des. 2022;221:110983. https://doi.org/10.1016/j.matdes.2022.110983.

[129] Vaudreuil S, Bencaid SE, Vanaei HR, El Magri A. Effects of Power and Laser Speed on the Mechanical Properties of AlSi7Mg0.6 Manufactured by Laser Powder Bed Fusion. Materials. 2022;15(23):8640. https://doi.org/10.3390/ma15238640.

[130] López C, Elías-Zúñiga A, Jiménez I, et al. Experimental Determination of Residual Stresses Generated by Single Point Incremental Forming of AlSi10Mg Sheets Produced Using SLM Additive Manufacturing Process. Materials. 2018;11(12):2542. https://doi.org/10.3390/ma11122542.

[131] Seshadev Sahoo. Prediction of residual stress and deformation of build part with variation of hatch spacing in direct metal laser sintering of AlSi10Mg built part: Thermo-mechanical modeling. J. Laser Appl. 2021;33(3):032011. doi:10.2351/7.0000393.

[132] Jiaojiao Wu, Linzhi Wang, Xuguang An. Numerical analysis of residual stress evolution of AlSi10Mg manufactured by selective laser melting. Optik. 2017;137:65-78. doi:10.1016/j.ijleo.2017.02.060.

[133] Karolus Małgorzata, Maszybrocka Joanna, Stwora Andrzej, Skrabalak Grzegorz. Residual stresses of AlSi10Mg fabricated by selective laser melting (SLM). Arch Metall Mater. 2019;64(3):1011-1016. doi:10.24425/amm.2019.129488.

[134] C. Li, J.F. Liu, X.Y. Fang, Y.B. Guo. Efficient predictive model of part distortion and residual stress in selective laser melting. Additive Manufacturing. 2017;17:157-168. doi:10.1016/j.addma.2017.08.014.

[135] Alireza Dareh Baghi, Shahrooz Nafisi, Reza Hashemi, Heike Ebendorff-Heidepriem, Reza Ghomashchi. Effective post-processing of SLM fabricated Ti-6Al-4 V alloy: Machining vs thermal treatment. J Manuf Process. 2021;68(Part A):1031-1046. doi:10.1016/j.jmapro.2021.06.035.

[136] Pehlivan E, Džugan J, Fojt J, Sedláček R, Rzepa S, Daniel M. Post-processing treatment impact on mechanical properties of SLM deposited Ti-6Al-4 V porous structure for biomedical application. Materials (Basel). 2020;13(22):5167. doi:10.3390/ma13225167. PMID: 33207787; PMCID: PMC7696100.

[137] Witkin DB, Patel DN, Helvajian H, et al. Surface treatment of powder-bed fusion additive manufactured metals for improved fatigue life. J Mater Eng Perform. 2019;28:681-692. doi:10.1007/s11665-018-3732-9.

[138] Y. Sun, R. Bailey, A. Moroz. Surface finish and properties enhancement of selective laser melted 316L stainless steel by surface mechanical attrition treatment. Surf Coat Technol. 2019;378:124993. doi:10.1016/j.surfcoat.2019.124993.

[139] Simoni F, Huxol A, Villmer FJ. Improving surface quality in selective laser melting-based tool making. J Intell Manuf. 2021;32:1927-1938. doi:10.1007/s10845-021-01744-9.

[140] García-Blanco MB, Díaz-Fuentes M, Espinosa E, Mancisidor AM, Vara G. Comparative study of different surface treatments applied to Ti6Al4V parts produced by Selective Laser Melting. Trans IMF. 2021;99(5):274-280. doi:10.1080/00202967.2021.1898171.

[141] Andrea Avanzini, Davide Battini, Marcello Gelfi, Luca Girelli, Candida Petrogalli, Annalisa Pola, Marialaura Tocci. Investigation on fatigue strength of sand-blasted DMLS-AlSi10Mg alloy. Procedia Struct Integrity. 2019;18:119-128. doi:10.1016/j.prostr.2019.08.146.

[142] Eleonora Atzeni, Andrea Balestrucci, Angioletta R. Catalano, Luca Iuliano, Paolo C. Priarone, Alessandro Salmi, Luca Settineri. Performance assessment of a vibro-finishing technology for additively manufactured components. Procedia CIRP. 2020;88:427-432. doi:10.1016/j.procir.2020.05.074.

[143] Erfan Maleki, Sara Bagherifard, Farshad Sabouri, Michele Bandini, Mario Guagliano. Hybrid thermal, mechanical, and chemical surface post-treatments for improved fatigue behavior of laser powder bed fusion AlSi10Mg notched samples. Surf Coat Technol. 2022;430:127962. doi:10.1016/j.surfcoat.2021.127962.

[144] Maamoun AH, Elbestawi MA, Veldhuis SC. Influence of shot peening on AlSi10Mg parts fabricated by additive manufacturing. J Manuf Mater Process. 2018;2(3):40. doi:10.3390/jmmp2030040.

[145] Naor Elad Uzan, Shlomo Ramati, Roni Shneck, Nachum Frage, Ori Yeheskel. On the effect of shot-peening on fatigue resistance of AlSi10Mg specimens fabricated by additive manufacturing using selective laser melting (AM-SLM). Addit Manuf. 2018;21:458-464. doi:10.1016/j.addma.2018.03.030.

[146] Erfan Maleki, Sara Bagherifard, Asghar Heydari Astaraee, Simone Sgarbazzini, Michele Bandini, Mario Guagliano. Application of gradient severe shot peening as a novel mechanical surface treatment on fatigue behavior of additively manufactured AlSi10Mg. Mater Sci Eng A. 2023;881:145397. doi:10.1016/j.msea.2023.145397.

[147] Hongzhuang Zhang, Changyou Li, Guo Yao, Yimin Zhang. Hot isostatic pressing of laser powder-bed-fused 304L stainless steel under different temperatures. Int J Mech Sci. 2022;226:107413. doi:10.1016/j.ijmecsci.2022.107413.

[148] Grech IS, Sullivan JH, Lancaster RJ, Plummer J, Lavery NP. The optimization of hot isostatic pressing treatments for enhanced mechanical and corrosion performance of stainless steel 316L produced by laser powder bed fusion. Addit Manuf. 2022;58:103072. doi:10.1016/j.addma.2022.103072.

[149] Arumugham Akilan A, Enneti RK, Balla VK, Atre SV. Effects of Hot Isostatic Pressing on the Properties of Laser-Powder Bed Fusion Fabricated Water Atomized 25Cr7Ni Stainless Steel. Lubricants. 2022; 10(12):340. https://doi.org/10.3390/lubricants10120340

[150] Santos Macías, J.G., Zhao, L., Tingaud, D. et al. Hot isostatic pressing of laser powder bed fusion AlSi10Mg: parameter identification and mechanical properties. J Mater Sci 57, 9726–9740 (2022). https://doi.org/10.1007/s10853-022-07027-9

[151] Schneller W, Leitner M, Springer S, Grün F, Taschauer M. Effect of HIP Treatment on Microstructure and Fatigue Strength of Selectively Laser Melted AlSi10Mg. J Manuf Mater Process. 2019;3(1):16. https://doi.org/10.3390/jmmp3010016

[152] Hafenstein S, Hitzler L, Sert E, Öchsner A, Merkel M, Werner E. Hot Isostatic Pressing of Aluminum–Silicon Alloys Fabricated by Laser Powder-Bed Fusion. Technologies. 2020;8(3):48. https://doi.org/10.3390/technologies8030048

[153] Ertuğrul O, Öter ZÇ, Yılmaz MS, Şahin E, Coşkun M, Tarakçı G, Koç E. Effect of HIP process and subsequent heat treatment on microstructure and mechanical properties of direct metal laser sintered AlSi10Mg alloy. Rapid Prototyping J. 2020;26(8):1421-1434. https://doi.org/10.1108/RPJ-07-2019-0180

[154] Giovagnoli M, Tocci M, Fortini A, Merlin M, Ferroni M, Migliori A, Pola A. Effect of different heat-treatment routes on the impact properties of an additively manufactured AlSi10Mg alloy. Mater Sci Eng A. 2021;802:140671. https://doi.org/10.1016/j.msea.2020.140671

[155] Tocci M, Pola A, Gelfi M, et al. Effect of a New High-Pressure Heat Treatment on Additively Manufactured AlSi10Mg Alloy. Metall Mater Trans A. 2020;51:4799-4811. https://doi.org/10.1007/s11661-020-05905-y

[156] Clement CD, Masson J, Kabir AS. Effects of Heat Treatment on Microstructure and Mechanical Properties of AlSi10Mg Fabricated by Selective Laser Melting Process. J Manuf Mater Process. 2022;6(3):52. https://doi.org/10.3390/jmmp6030052

[157] Gao C, Liu Z, Xiao Z, Zhang W, Wong K, Akbarzadeh AH. Effect of heat treatment on SLM-fabricated TiN/AlSi10Mg composites: Microstructural evolution and mechanical properties. J Alloys Compd. 2021;853:156722. https://doi.org/10.1016/j.jallcom.2020.156722

[158] Han Q, Jiao Y. Effect of heat treatment and laser surface remelting on AlSi10Mg alloy fabricated by selective laser melting. Int J Adv Manuf Technol. 2019;102:3315–3324. https://doi.org/10.1007/s00170-018-03272-y

[159] Rosenthal I, Stern A. Heat treatment investigation of the Alsi10Mg alloy produced by selective laser melting (SLM): Microstructure and hardness. Ann "Dunarea de Jos" Univ of Galati, Fascicle XII, Welding Equip Technol. 2016;27:7-11.

[160] Fonda, R., Reynolds, A., Feng, C. R., Rowenhorst, D., & Maier, H. J. (2013). Material flow in friction stir welds. Metallurgical and Materials Transactions A, 44(1), 337-344. https://doi.org/10.1007/s11661-012-1460-6

[161] Boldsaikhan, E., Milhon, M., Fukada, S., Fujimoto, M., & Kamimuki, K. (2023). Metrology of sheet metal distortion and effects of spot-welding sequences on sheet metal distortion. Journal of Manufacturing and Materials Processing, 7(3), 109. https://doi.org/10.3390/jmmp7030109

[162] Badkoobeh, F., Mostaan, H., Rafiei, M., Bakhsheshi-Rad, H. R., & Berto, F. (2021). Friction stir welding/processing of Mg-based alloys: A critical review on advancements and challenges. Materials, 14(21), 6726. https://doi.org/10.3390/ma14216726

[160] Heidarzadeh A, Khorshidi M, Mohammadzadeh R, Khajeh R, Mofarrehi M, Javidani M, Chen X-G. Multipass Friction Stir Processing of Laser-Powder Bed Fusion AlSi10Mg: Microstructure and Mechanical Properties. Materials. 2023; 16(4):1559. https://doi.org/10.3390/ma16041559

[161] Lv, Zhao., Lv, Zhao., Juan, Guillermo, Santos, Macias., Lipeng, Ding., Lipeng, Ding., Hosni, Idrissi., Hosni, Idrissi., Aude, Simar. (2019). Damage mechanisms in selective laser melted AlSi10Mg under as built and different post-treatment conditions. Materials Science and Engineering A-structural Materials Properties Microstructure and Processing, 764:138210-. doi: 10.1016/J.MSEA.2019.138210

[162] Santos Macías, Juan Guillermo & Elangeswaran, Chola & lv, Zhao & Hooreweder, Brecht & Adrien, Jérôme & Maire, Eric & Buffière, Jean-Yves & Ludwig, Wolfgang & Jacques, Pascal & Simar, Aude. (2019). Ductilisation and fatigue life enhancement of selective laser melted AlSi10Mg by friction stir processing. Scripta Materialia. 170. 124-128. 10.1016/j.scriptamat.2019.05.044.

[163] Scherillo, F., Astarita, A., Prisco, U., et al. (2018). Friction Stir Welding of AlSi10Mg Plates Produced by Selective Laser Melting. Metallography, Microstructure, and Analysis, 7, 457–463. https://doi.org/10.1007/s13632-018-0465-y

[164] Huang, C., Yan, X., Zhao, L., Liu, M., Ma, W., Wang, W., Soete, J., Simar, A. (2019). Ductilization of selective laser melted Ti6Al4V alloy by friction stir processing. Materials Science and Engineering: A, 755, 85-96. https://doi.org/10.1016/j.msea.2019.03.133

[165] Maamoun, A. H., Veldhuis, S. C., & Elbestawi, M. (2019). Friction stir processing of AlSi10Mg parts produced by selective laser melting. Journal of Materials Processing Technology, 263, 308-320. https://doi.org/10.1016/j.jmatprotec.2018.08.030

[166] Lv, Z., Santos Macías, J. G., Dolimont, A., Simar, A., Rivière, E., & Lorphèvre. (2020). Comparison of residual stresses obtained by the crack compliance method for parts produced by different metal additive manufacturing techniques and after friction stir processing. Additive Manufacturing, 36, 101499. https://doi.org/10.1016/j.addma.2020.101499

[167] Perard, T., Sova, A., Robe, H., & others. (2021). Friction stir processing of austenitic stainless steel cold spray coating deposited on 304L stainless steel substrate: feasibility study. International Journal of Advanced Manufacturing Technology, 115, 2379-2393. https://doi.org/10.1007/s00170-021-07295-w

[168] Sjölander E, Seifeddine S. The heat treatment of Al–Si–Cu–Mg casting alloys. J Mater Process Technol. 2010;210(10):1249-1259. https://doi.org/10.1016/j.jmatprotec.2010.03.020

[169] Chen Y, Wang L, Feng Z, Zhang W. Effects of heat treatment on microstructure and mechanical properties of SLMed Sc-modified AlSi10Mg alloy. Prog Nat Sci Mater Int. 2021;31(5):714-721. https://doi.org/10.1016/j.pnsc.2021.08.003

[170] Paoletti C, Cerri E, Ghio E, Santecchia E, Cabibbo M, Spigarelli S. Effect of Low-Temperature Annealing on Creep Properties of AlSi10Mg Alloy Produced by Additive Manufacturing: Experiments and Modeling. Metals. 2021;11(2):179. https://doi.org/10.3390/met11020179

[171] Shahani AJ, Xiao X, Skinner K, Peters M, Voorhees PW. Ostwald ripening of faceted Si particles in an Al-Si-Cu melt. Mater Sci Eng A. 2016;673:307-320. https://doi.org/10.1016/j.msea.2016.06.077

[172] Fiocchi J, Tuissi A, Bassani P, Biffi CA. Low temperature annealing dedicated to AlSi10Mg selective laser melting products. J Alloys Compd. 2017;695:3402-3409. https://doi.org/10.1016/j.jallcom.2016.12.019

[173] Zhang C, et al. 2019 IOP Conf. Ser.: Mater. Sci. Eng. 538 012023

[174] Schuch M, Hahn T, Bleckmann M. The mechanical behavior and microstructure of additively manufactured AlSi10Mg for different material states and loading conditions. Mater Sci Eng A. 2021;813:141134. https://doi.org/10.1016/j.msea.2021.141134

[175] Soundararajan B, Sofia D, Barletta D, Poletto M. Review on modeling techniques for powder bed fusion processes based on physical principles. Addit Manuf. 2021;47:102336. https://doi.org/10.1016/j.addma.2021.102336

[176] Alomar Z, Concli F. A Review of the Selective Laser Melting Lattice Structures and Their Numerical Models. Adv Eng Mater. 2020;22:2000611. https://doi.org/10.1002/adem.202000611

[177] Van Belle L, Vansteenkiste G, Boyer JC. Comparisons of Numerical Modelling of the Selective Laser Melting. Key Eng Mater. 2012;504–506:1067–1072. https://doi.org/10.4028/www.scientific.net/kem.504-506.1067

[170] Tsivilskiy I, Shishkovsky I. Thermal-structural hybrid Lagrangian solver and numerical simulation-based correction of shape deformation of stainless-steel parts produced by laser powder bed fusion. Sci Rep. 2023;13:17535. https://doi.org/10.1038/s41598-023-43968-0

[171] Li E, Zhou Z, Wang L, Shen H, Zou R, Yu A. Particle scale modelling of melt pool dynamics and pore formation in selective laser melting additive manufacturing. Powder Technology. 2022;397:117012. https://doi.org/10.1016/j.powtec.2021.11.056.

[172] Cao L. Mesoscopic-Scale Numerical Investigation Including the Influence of Process Parameters on LPBF Multi-Layer Multi-Path Formation. CMES-Computer Modeling in Engineering & Sciences. 2021;126(1):5–23.

[173] Shrestha S, Chou YK. A Numerical Study on the Keyhole Formation During Laser Powder Bed Fusion Process. J Manuf Sci Eng. 2019;141(10):101002. https://doi.org/10.1115/1.4044100.

[174] Chen H, Sun Y, Yuan W, Pang S, Yan W, Shi Y. A Review on Discrete Element Method Simulation in Laser Powder Bed Fusion Additive Manufacturing. Chin J Mech Eng: Additive Manufacturing Frontiers. 2022;1(1):100017. https://doi.org/10.1016/j.cjmeam.2022.100017.

[175] Habiba U, Hebert RJ. Powder Spreading Mechanism in Laser Powder Bed Fusion Additive Manufacturing: Experiments and Computational Approach Using Discrete Element Method. Materials. 2023;16(7):2824. https://doi.org/10.3390/ma16072824.

[176] Homami RM, Ojo O. Residual stress analysis through numerical simulation in powder bed additive manufacturing using the representative volume approach. Int J Adv Manuf Technol. 2023. https://doi.org/10.1007/s00170-023-12634-0.

[177] Zhang ZD, Shahabad SI, Ibhadode O, Dibia CF, Bonakdar A, Toyserkani E. 3-Dimensional heat transfer modeling for laser powder bed fusion additive manufacturing using parallel computing and adaptive mesh. Opt Laser Technol. 2023;158(A):108839. https://doi.org/10.1016/j.optlastec.2022.108839.

[178] Zhang Z, Wang Y, Ge P, Wu T. A Review on Modelling and Simulation of Laser Additive Manufacturing: Heat Transfer, Microstructure Evolutions and Mechanical Properties. Coatings. 2022;12(9):1277. https://doi.org/10.3390/coatings12091277.

[179] Ricci S, Testa G, Iannitti G, Ruggiero A. Laser powder bed fusion of AlSi10Mg alloy: Numerical investigation on the temperature field evolution. Forces in Mechanics. 2022;8:100109. https://doi.org/10.1016/j.finmec.2022.100109.

[180] Zinovieva O, Romanova V, Dymnich E, Zinoviev A, Balokhonov R. A Review of Computational Approaches to the Microstructure-Informed Mechanical Modelling of Metals Produced by Powder Bed Fusion Additive Manufacturing. Materials. 2023;16(19):6459. https://doi.org/10.3390/ma16196459.

[181] Zhang Y, Chen Q, Guillemot G, Gandin CA, Bellet M. Numerical modelling of fluid and solid thermomechanics in additive manufacturing by powder-bed fusion: Continuum and level set formulation applied to track- and part-scale simulations. Comptes Rendus Mécanique. 2018;346(11):1055-1071. https://doi.org/10.1016/j.crme.2018.08.008.

[182] Jakumeit J, Zheng G, Laqua R, Clark SJ, Zielinski J, Schleifenbaum JH, Lee PD. Modelling the complex evaporated gas flow and its impact on particle spattering during laser powder bed fusion. Additive Manufacturing. 2021;47:102332. https://doi.org/10.1016/j.addma.2021.102332.

[183] Rodgers TM, Moser D, Abdeljawad F, Underwood Jackson OD, Carroll JD, Jared BH, Bolintineanu DS, Mitchell JA, Madison JD. Simulation of powder bed metal additive manufacturing microstructures with coupled finite difference-Monte Carlo method. Additive Manufacturing. 2021;41:101953. https://doi.org/10.1016/j.addma.2021.101953.

[184] Li Z et al. 2023. IOP Conf. Ser.: Mater. Sci. Eng. 1281:012017.

[185] Barrionuevo GO, Ramos-Grez JA, Walczak M, Sánchez-Sánchez X, Guerra C, Debut A, Haro E. Microstructure simulation and experimental evaluation of the anisotropy of 316 L stainless steel manufactured by laser powder bed fusion. Rapid Prototyping Journal. 2023;29(3):425-436. https://doi.org/10.1108/RPJ-04-2022-0127.

[186] Mede T, Kocjan A, Paulin I, Godec M. Numerical Mesoscale Modelling of Microstructure Evolution during Selective Laser Melting. Metals. 2020;10(6):800. https://doi.org/10.3390/met10060800.

[187] Zinovieva O, Zinoviev A, Ploshikhin V. Three-dimensional modeling of the microstructure evolution during metal additive manufacturing. Comput Mater Sci. 2018;141:207-220. https://doi.org/10.1016/j.commatsci.2017.09.018.

[188] Tangestani R, Sabiston T, Chakraborty A, Yuan L, Krutz N, Martin É. An Efficient Track-Scale Model for Laser Powder Bed Fusion Additive Manufacturing: Part 2—Mechanical Model. Front Mater. 2021;8:759669. https://doi.org/10.3389/fmats.2021.759669.

[189] Vaglio E, De Monte T, Lanzutti A, Totis G, Sortino M, Fedrizzi L. Single tracks data obtained by selective laser melting of Ti6Al4V with a small laser spot diameter. Data in Brief. 2020;33:106443. https://doi.org/10.1016/j.dib.2020.106443.

[190] Sharma R, Kumar A. Track-Scale Simulations of Selective Laser Melting to Investigate Development and Mitigation of Thermal Stresses. Lasers Manuf Mater Process. 2019;6:464–492. https://doi.org/10.1007/s40516-019-00103-0.

[191] Galati M, Di Mauro O, Iuliano L. Finite Element Simulation of Multilayer Electron Beam Melting for the Improvement of Build Quality. Crystals. 2020;10(6):532. doi:10.3390/cryst10060532.

[192] Bandyopadhyay A, Traxel KD. Invited Review Article: Metal-additive manufacturing - Modeling strategies for application-optimized designs. Addit Manuf. 2018;22:758-774. doi:10.1016/j.addma.2018.06.024. PMID: 30746332; PMCID: PMC6368101.

[193] Zhang Y, Guillemot G, Bernacki M, Bellet M. Macroscopic thermal finite element modeling of additive metal manufacturing by selective laser melting process. Comput Methods Appl Mech Eng. 2018;331:514-535. doi:10.1016/j.cma.2017.12.003.

[194] Meier C, Fuchs S, Much N, Nitzler J, Penny R, Praegla P, et al. Physics-Based Modeling and Predictive Simulation of Powder Bed Fusion Additive Manufacturing Across Length Scales. 2021.

[195] Li C, Fu CH, Guo YB, Fang FZ. Fast Prediction and Validation of Part Distortion in Selective Laser Melting. Procedia Manuf. 2015;1:355-365. doi:10.1016/j.promfg.2015.09.042.

[196] Patuelli C, Cestino E, Frulla G, Valente F, Servetti G, Esposito F, Barbero L. FEM Simulation of AlSi10Mg Artifact for Additive Manufacturing Process Calibration with Industrial-Computed Tomography Validation. Materials (Basel). 2023;16(13):4754. doi:10.3390/ma16134754.

[197] Dong W, Liang X, Chen Q, Hinnebusch S, Zhou Z, To AC, et al. A new procedure for implementing the modified inherent strain method with improved accuracy in predicting both residual stress and deformation for laser powder bed fusion. Addit Manuf. 2021;47:102345. doi:10.1016/j.addma.2021.102345.

[198] Ma N, Nakacho K, Ohta T, Ogawa N, Maekawa A, Huang H, et al. Inherent Strain Method for Residual Stress Measurement and Welding Distortion Prediction. Proc ASME Int Conf Ocean Offshore Arctic Eng. 2016;9:V009T13A001. doi:10.1115/OMAE2016-54184.

[199] Bugatti M, Semeraro Q. Limitations of the inherent strain method in simulating powder bed fusion processes. Addit Manuf. 2018;23:329-346. doi:10.1016/j.addma.2018.05.041.

[200] Dogea R, Yan XT, Millar R. Examining the inherent strains of aluminium alloy 7050-T7451 powder for additive manufacturing processes. MRS Commun. 2022;12:813-818. doi:10.1557/s43579-022-00244-y.

[201] Didier P, Le Coz G, Robin G, et al. Consideration of additive manufacturing supports for post-processing by end milling: a hybrid analytical–numerical model and experimental validation. Prog Addit Manuf. 2022;7:15-27. doi:10.1007/s40964-021-00211-4.

[202] Khorasani AM, Gibson I, Ghaderi A, et al. Investigation on the effect of heat treatment and process parameters on the tensile behaviour of SLM Ti-6Al-4V parts. Int J Adv Manuf Technol. 2019;101:3183-3197. doi:10.1007/s00170-018-3162-8.

[203] Cardon A, Mareau C, Ayed Y, van der Veen S, Giraud E, et al. Heat treatment simulation of Ti-6Al-4V parts produced by selective laser melting. Addit Manuf. 2020;39:101766. doi:10.1016/j.addma.2020.101766.

[204] Warnken N, Larsson H, Reed RC. Coupled modelling of solidification and solution heat treatment of advanced single crystal nickel bas superalloy. Mater Sci Technol. 2009;25:179-185.

[205] Salsi, E., Chiumenti, M., & Cervera, M. (2018). Modeling of Microstructure Evolution of Ti6Al4V for Additive Manufacturing. Metals - Open Access Metallurgy Journal, 8. https://doi.org/10.3390/met8080633

[206] Hannachi, N., Khalfallah, A., Leitao, C., & Rodrigues, D. (2021). Comparison Between ALE and CEL Finite Element Formulations to Simulate Friction Stir Spot Welding.

[207] Chen, G. Q., Shi, Q. Y., Fujiya, Y., et al. (2014). Simulation of Metal Flow During Friction Stir Welding Based on the Model of Interactive Force Between Tool and Material. Journal of Materials Engineering and Performance, 23, 1321-1328. https://doi.org/10.1007/s11665-014-0886-y

[208] Bussetta, P., Marceau, D., & Ponthot, J.-P. (2012). The adapted augmented Lagrangian method: A new method for the resolution of the mechanical frictional contact problem. Computational Mechanics, 49(2), 259-275. https://doi.org/10.1007/s00466-011-0644-z.

[209] Simo, J. C., & Laursen, T. A. (1992). An augmented Lagrangian treatment of contact problems involving friction. Computers & Structures, 42(1), 97-116. https://doi.org/10.1016/0045-7949(92)90540-G.

[210] Liu, F.; Xu, P.; Zhang, H.; Guan, C.; Feng, D.; Wang, X. Use of Time-of-Flight Ultrasound to Measure Wave Speed in Poplar Seedlings. Forests 2019, 10, 682. https://doi.org/10.3390/f10080682.

[211] Eryi Hu, Wenjin Wang, "The Elastic Constants Measurement of Metal Alloy by Using Ultrasonic Nondestructive Method at Different Temperature", Mathematical Problems in Engineering, vol. 2016, Article ID 6762076, 2016. https://doi.org/10.1155/2016/6762076.

[212] Sol T., Hayun S., Noima D., Tiferet E., Yeheskel O., Tevet O. Nondestructive ultrasonic evaluation of additively manufactured AlSi10Mg samples. Addit. Manuf. 2018;22:700–707. doi: 10.1016/j.addma.2018.06.016.

[213] Fisher, Karl A., Candy, Jim V., Guss, Gabe, and Mathews, M. J. Evaluating Acoustic Emission Signals as an in situ process monitoring technique for Selective Laser Melting (SLM). United States: N. p., 2016. Web. doi:10.2172/1342013.

[214] Naor Elad Uzan, Barak Ratzker, Peri Landau, Sergey Kalabukhov, Nachum Frage, Compressive creep of AlSi10Mg parts produced by selective laser melting additive manufacturing technology, Additive Manufacturing, Volume 29, 2019, 100788, ISSN 2214-8604, https://doi.org/10.1016/j.addma.2019.100788.

[215] Xiaofeng Li, Denghao Yi, Xiaoyu Wu, Jinfang Zhang, Xiaohui Yang, Zixuan Zhao, Yinghao Feng, Jianhong Wang, Peikang Bai, Bin Liu, Yong Liu, Effect of construction angles on microstructure and mechanical properties of AlSi10Mg alloy fabricated by selective laser melting, Journal of Alloys and Compounds, Volume 881, 2021, 160459, ISSN 0925-8388, https://doi.org/10.1016/j.jallcom.2021.160459.

[216] Wu, Z., Wu, S., Gao, X. et al. The role of internal defects on anisotropic tensile failure of L-PBF AlSi10Mg alloys. Sci Rep 13, 14681 (2023). https://doi.org/10.1038/s41598-023-39948-z

[217] Otto M, Pilz S, Gebert A, Kühn U, Hufenbach J. Effect of Build Orientation on the Microstructure, Mechanical and Corrosion Properties of a Biodegradable High Manganese Steel Processed by Laser Powder Bed Fusion. Metals. 2021; 11(6):944. https://doi.org/10.3390/met11060944

[218] Promoppatum, P., Srinivasan, R., Quek, S.S., et al. Quantification and prediction of lack of-fusion porosity in the high porosity regime during laser powder bed fusion of Ti-6Al-4V. Journal of Materials Processing Technology. 300. (2022).

[219] Thijs, Lore, et al. "Fine-structured aluminium products with controllable texture by selective laser melting of pre-alloyed AlSi10Mg powder." Acta Materialia 61.5 (2013): 1809-1819.

[220] Yusuf, Shahir Mohd, Mathias Hoegden, and Nong Gao. "Effect of sample orientation on the microstructure and microhardness of additively manufactured AlSi10Mg processed by high-pressure torsion." The International Journal of Advanced Manufacturing Technology 106.9 (2020): 4321-4337.

[221] Van Cauwenbergh, P., Beckers, A., Lore, T., Hooreweder, B., & Vanmeensel, K. (2018). Heat Treatment Optimization via Thermo-Physical Characterization of AlSi7Mg and AlSi10Mg Manufactured by Laser Powder Bed Fusion (LPBF).

[222] Cabrini, M., Lorenzi, S., Testa, C., Manfredi, D., Lombardi, M., Aversa, A., Andreatta, F., Fedrizzi, L., Dekhtyar, Y., Sorokins, H., & Biamino, S. (2021). Effect of Heat Treatment on Microstructure and Selective Corrosion of LPBF-AlSi10Mg by Means of SKPFM and Exo-Electron Emission. Materials, 14(19), 5602.

[223] C. Jing, H. Wei / Microstructure, porosity and mechanical properties of selective laser melted AlSi10Mg // Journal of Aeronautics. DOI: 10.1016/j.cja.2019.08.017

[224] Abu-Lebdeh, T., Damptey, R., Lamberti, V, Hamoush, S. (2019). Powder Packing Den-sity and Its Impact on SLM-Based Additive Manufacturing.

[225] Yuan W., Chen H., T. Cheng T., et al. Effects of laser scanning speeds on different states of the molten pool during selective laser melting: simulation and experiment. Mater Des, 189 (2020), Article 108542, 10.1016/j.matdes.2020.108542.

[226] Zhuang, J.R., Lee, Y.T., Hsieh, Y.H., Yang, A.S. Determination of melt pool dimen-sions using DOE-FEM and RSM with process window during SLM of Ti6Al4V powder. Optics & Laser Technology. 103. (2018). 59-76.

[227] Kheirabadi A.C, Groulx, D. "The Effect of the Mushy-Zone Constant on Simulated Phase Change Heat Transfer," in Proceedings of CHT-15 (Rutgers University, Pisca-taway, USA, 2015).

[228] Laakso P, Riipinen T, Laukkanen A, Andersson T, Jokinen A, Revuelta A, Ruusuvuori K. (2016). Optimization and Simulation of SLM Process for High Density H13 Tool Steel Parts. Physics Procedia

[229] Kerslake, T.W. (1991), Experiments With Phase Change Thermal Energy Storage Can-isters For Space Station Freedom," 26th Interso¢iety Energy Conversion Engineering Conference. Boston, Mass., p. 248-261 (see also NASA TM-104427).

[230] Liu, B., Li, B., Li, Z., Bai, P., Wang, Y., & Kuai, Z. (2019). Numerical investigation on heat transfer of multi-laser processing during selective laser melting of AlSi10Mg. Results in Physics., 12, 2019, 454-459.

[231] Aboulkhair, N.T , Maskery, I. , Tuck, C. , Ashcroft, I. , Everitt, N.M. The microstruc-ture and mechanical properties of selectively laser melted AlSi10Mg: the effect of a conventional T6-like heat treatment Mater Sci Eng A, 667 (2016), 139-146.

[232] Fiedler, T., Dörries, K. & Rösler, J. Selective laser melting of Al and AlSi10Mg: pa-rameter study and creep experiments. Prog Addit Manuf (2021).

[233] Astakhov, V. (2012). Design of Experiment Methods in Manufacturing: Basics and Practical Applications.

[234] Zhirnov, I., Kotoban, D.V. & Gusarov, A.V. Evaporation-induced gas-phase flows at selective laser melting. Appl. Phys. A 124, 157 (2018).

[235] Caiazzo, F. Additive manufacturing by means of laser-aided directed metal deposition of titanium wire. Int J Adv Manuf Technol 96, 2699–2707 (2018).

[236] Zyguła, K., Nosek, B., Pasiowiec, H., Szysiak, N. (2018). Mechanical properties and microstructure of AlSi10Mg alloy obtained by casting and SLM technique. WSN 104. 462-472.

[237] Chen J, Hou W, Wang X, Chu S, Yang Z. (2019). Microstructure, porosity and mechanical properties of selective laser melted AlSi10Mg. Chinese Journal of Aeronautics. 33.

[238] Ch. Chen, J. Yin, H. Zhu, Z. Xiao, L. Zhang, X. Zeng, Effect of overlap rate and pattern on residual stress in selective laser melting, International Journal of Machine Tools and Manufacture, 145, (2019), 103433, https://doi.org/10.1016/j.ijmachtools.2019.103433.

[239] B. Cheng, S. Shrestha, K. Chou, Stress and deformation evaluations of scanning strategy effect in selective laser melting, Additive Manufacturing, 12, Part B, (2016), 240-251, https://doi.org/10.1016/j.addma.2016.05.007.

[240] Pant, P., Salvemini, F., Proper, S., Luzin, V., Simonsson, K., Sjöström, S., Hosseini, S., Peng, R. L., & Moverare, J. (2022). A study of the influence of novel scan strategies on residual stress and microstructure of L-shaped LPBF IN718 samples. Materials & Design, 214, 110386. https://doi.org/10.1016/j.matdes.2022.110386

[241] Cox, B., Ghayoor, M., Pasebani, S., & Gess, J. (2023). Tracking of Marangoni driven motion during laser powder bed fusion. Powder Technology, 425, 118610. https://doi.org/10.1016/j.powtec.2023.118610

[242] Kozhuthala Veetil, J., Khorasani, M., Ghasemi, A., Rolfe, B., Vrooijink, I., Van Beurden, K., Moes, S., & Gibson, I. (2021). Build position-based dimensional deviations of laser powder-bed fusion of stainless steel 316L. Precision Engineering, 67, 58-68. https://doi.org/10.1016/j.precisioneng.2020.09.024

[243] Kan, W.H., Chiu, L.N.S., Lim, C.V.S. et al. A critical review on the effects of process-induced porosity on the mechanical properties of alloys fabricated by laser powder bed fusion. J Mater Sci 57, 9818–9865 (2022). https://doi.org/10.1007/s10853-022-06990-7

[244] Paraschiv, A., Matache, G., Constantin, N., & Vladut, M. (2022). Investigation of Scanning Strategies and Laser Remelting Effects on Top Surface Deformation of Additively Manufactured IN 625. Materials (Basel, Switzerland), 15(9), 3198. https://doi.org/10.3390/ma15093198

[245] M.J. Ansari, D.S. Nguyen, H.S. Park, Investigation of SLM Process in Terms of Temperature Distribution and Melting Pool Size: Modeling and Experimental Approaches, Materials 12(8):1272 (2019).

[246] B. Blackford, G. Zak, I.Y Kim, I.Y. The effect of scan path on thermal gradient during selective laser melting. Int J Adv Manuf Technol 110, 1261–1274 (2020). https://doi.org/10.1007/s00170-020-05899-2

[247] M. Leary, Surface roughness optimisation for selective laser melting (SLM), Laser Additive Manufacturing (2017) 99-118.

[248] R. Huang, N. Dai, X. Cheng, Build orientation optimization for lightweight lattice parts production in selective laser melting using a multicriteria genetic algorithm, Journal of Materials Research 35 (2020) 1-9.

[249] International Organization for Standardization. (1997). Geometrical product specifications (GPS) - Surface texture: Profile method - Terms, definitions and surface texture parameters (ISO 4287:1997). ISO.

[250] A. Maamoun, J. Xue, M. Elbestawi, S.C. Veldhuis, Effect of Selective Laser Melting Process Parameters on the Quality of Al Alloy Parts: Powder Characterization, Density, Surface Roughness, and Dimensional Accuracy, Materials 11. 2343 (2018).

[251] J. Babu, M. Mehrpouya, T. Pijper, G. Willemsen, T. Vaneker. (2022). An Experimental Study of Down-Facing Surfaces in Selective Laser Melting. Advanced Engineering Materials. 24. 10.1002/adem.202101562.

[252] Mahajan AM, Krishna KV, Quamar MJ, Rehman AU, Bandi B, Babu NK. Structure–Property Correlation between Friction-Welded Work Hardenable Al-4.9Mg Alloy Joints. Crystals. 2023; 13(7):1119. https://doi.org/10.3390/cryst13071119

[253] Agha Amini Fashami, H., Bani Mostafa Arab, N., Hoseinpour Gollo, M. et al. Numerical and experimental investigation of defects formation during friction stir processing on AZ91. SN Appl. Sci. 3, 108 (2021). https://doi.org/10.1007/s42452-020-04032-y

[254] Mostafa M. El-Sayed, A.Y. Shash, M. Abd-Rabou, Mahmoud G. ElSherbiny, Welding and processing of metallic materials by using friction stir technique: A review, Journal of Advanced Joining Processes, Volume 3, 2021, 100059, ISSN 2666-3309, https://doi.org/10.1016/j.jajp.2021.100059.

[255] Ahmed H. Maamoun, Stephen C. Veldhuis, Mohamed Elbestawi, Friction stir processing of AlSi10Mg parts produced by selective laser melting, Journal of Materials Processing Technology, Volume 263, 2019, Pages 308-320, ISSN 0924-0136, https://doi.org/10.1016/j.jmatprotec.2018.08.030.

[256] Li Cui, Defan Wu, Yaoqing Chang, Xingye Guo, Xu Wu, Wei Shao, Dingyong He, Microstructural evolution and mechanical property of friction stir welded joints in AlSi10Mg alloys fabricated by laser powder bed fusion, CIRP Journal of Manufacturing Science and Technology, Volume 47, 2023, Pages 228-243, ISSN 1755-5817, https://doi.org/10.1016/j.cirpj.2023.11.002.

[257] S. Ismail, Q. Ahsan, A.S.M.A. Haseeb, 2.7 Recent Advances in Mechanical Surface Treatment, Comprehensive Materials Finishing, Elsevier, 2017, Pages 171-179, ISBN 9780128032497, https://doi.org/10.1016/B978-0-12-803581-8.09197-9.

[258] Maamoun AH, Elbestawi MA, Veldhuis SC. Influence of Shot Peening on AlSi10Mg Parts Fabricated by Additive Manufacturing. Journal of Manufacturing and Materials Processing. 2018; 2(3):40. https://doi.org/10.3390/jmmp2030040

[259] Khosa, S.U., Weinberger, T. & Enzinger, N. Thermo-Mechanical Investigations during Friction Stir Spot Welding (FSSW) of AA6082-T6. Weld World 54, R134–R146 (2010). https://doi.org/10.1007/BF03263499

[260] R. Zettler, 3 - Material deformation and joint formation in friction stir welding, In Woodhead Publishing Series in Welding and Other Joining Technologies, Friction Stir Welding, Woodhead Publishing, 2010, Pages 42-72, ISBN 9781845694500, https://doi.org/10.1533/9781845697716.1.42.

[261] Rana, P.K., Narayanan, R.G. & Kailas, S.V. Assessing the dwell time effect during friction stir spot welding of aluminum polyethylene multilayer sheets by experiments and numerical simulations. Int J Adv Manuf Technol 114, 1953–1973 (2021). https://doi.org/10.1007/s00170-021-06910-0

[262] A.K. Lakshminarayanan, V.E. Annamalai, K. Elangovan, Identification of optimum friction stir spot welding process parameters controlling the properties of low carbon automotive steel joints, Journal of Materials Research and Technology, Volume 4, Issue 3, 2015, Pages 262-272, ISSN 2238-7854, https://doi.org/10.1016/j.jmrt.2015.01.001.

[263] M. de Leon & H.-S. Shin (2016) Material flow behaviours during friction stir spot welding of lightweight alloys using pin and pinless tools, Science and Technology of Welding and Joining, 21:2, 140-146, DOI: 10.1179/1362171815Y.0000000075